UNIVERSITY OF MODENA AND REGGIO EMILIA

DOCTORAL SCHOOL IN
Molecular and Regenerative Medicine

XXXV CYCLE

Role of exosomes derived from amniotic fluid stem cells in counteracting age-related disorders

Candidate:
Dr. Martina Gatti

Supervisor: Prof. Carla Palumbo

Co-supervisor: Prof. Tullia Maraldi

Coordinator: Prof. Michele De Luca

Abstract

Life expectancy has greatly increased in recent decades, and this is associated with increased incidence of age-related chronic diseases. Among several factors, oxidative stress plays a central role in the onset and progression of these pathologies. During aging, loss in antioxidant defenses can cause a pathological imbalance between scavenger systems and reactive oxygen species (ROS), which finally leads to cell damage. Indeed, among the age-related conditions, oxidative stress increases in neurodegenerative disease, immune system diseases, musculoskeletal disorders, frailty, and sarcopenia.

In recent years, mesenchymal stromal/stem cells (MSCs), such as amniotic fluid stem cells (AFSCs), have been proposed as a potential therapy for different pathologies, thanks to their regenerative and tissue repairing capabilities. To explain their mechanisms of action different hypotheses have been proposed, including the paracrine implication of bioactive molecules carried by extracellular vesicles (EVs), such as exosomes.

This thesis work demonstrated the beneficial effects of EVs secreted by AFSCs (AFSC-EVs) on *in vitro* models of different degenerative disorders which affect osteoblasts, skeletal muscles, neurons, microglia, and their functional communication.

Dexamethasone (Dexa) is a synthetic glucocorticoid widely used in therapy. Despite its beneficial effects, their abuse can lead to negative consequences, including muscle loss and bone fragility. In light of this, Dexa was used to set up *in vitro* models of osteoporosis and muscle atrophy. First, AFSC-EVs reduced the oxidative stress observed in human osteoblast exposed to Dexa, as well as all the osteoporosis signs occurring in bone aging. Moreover, EVs ameliorated not only the differentiation capability affected in Dexa-treated bone cells, but also the pre-osteoblasts maturation potential.

Despite the high plasticity of skeletal muscle tissue, during aging its regenerative potential is hampered. During muscle atrophy, neuromuscular junctions (NMJs) become vulnerable, and the impairment in this crucial region of communication between muscle cells and motor neurons (MNs) results in muscle weakness, fueling a vicious circle. In this dramatic context, how skeletal muscle sends retrograde signals to MNs through NMJs, as well as the role and source of oxidative stress, represents an intriguing field of research. To study NMJ perturbations during muscle atrophy, a MN/myotube co-culture system by microfluidic devices was set up, and the crosstalk alterations occurring during Dexa-induced muscle atrophy were investigated. AFSC-EVs presence counteracted morphological and functional defects, as well as the oxidative stress occurring in atrophic myotubes and thus affecting neurites through NMJs.

Neurodegeneration characterizes several age-related disorders such as Alzheimer’s disease (AD) which presents abnormal protein aggregation, β-amyloid (Aβ) deposition, besides an increase in oxidative stress. In an *in vitro* model of AD, we observed a positive effect of AFSC-EV treatment on AD primary neuron morphology, viability, and levels of AD markers (i.e., Aβ and p-Tau). These effects could be due, at least in part, to the apoptotic and autophagic pathway modulation derived from the reduction in redox imbalance exerted by EVs. Since in AD microglia plays a pivotal role in regulating the brain Aβ levels, AFSC-EV immunomodulatory properties were explored in co-cultures of AD neurons and microglia. Interestingly, EV administration mitigated the inflammatory injury caused by microglia in neurons, and significantly recovered the neurotoxicity.

In conclusion, this work demonstrated that AFSC-EVs may be a potential therapeutic cell-free agent for the treatment of age-related degenerative pathologies.

Index

1. Preface

1.1 Stem cells and mesenchymal stromal/stem cells: potential for regenerative medicine

Regenerative medicine is an increasingly emerging field of research focused on repair, replacement or regeneration of cells, tissues, and whole organs [1]. Several studies have already reported encouraging results on the application of stem cell-based therapy, and for this reason, the research of potential novel stem cell sources is increasing.

Stem cells (SCs) are undifferentiated cells present in the embryonic, fetal, and adult life stages which can differentiate to build tissues and organs [2]. Even if the properties of these cells could differ according to the different cell types, all are characterized by self-renewal ability (extensive proliferation), clonality (usually deriving from a single cell), and potency (capability to differentiate into different cell types).

There are different ways for classifying stem cells. For example, according to their differentiation potential they can be divided in (1) totipotent or omnipotent, (2) pluripotent, (3) multipotent, (4) oligopotent, and (5) unipotent [3]. Another accepted way to categorize these cells, and more suitable for our purpose, is through their origin. Indeed, stem cells can be grouped as embryonic stem cells (ESCs), induced pluripotent stem cells (iPSCs), fetal stem cells (FSCs), perinatal stem cells (PSCs), and adult stem cells (ASCs) [4].

ESCs are pluripotent SCs, derived from the inner cell mass of the blastocyst before embryo implantation [5–7]. Their main advantages are the greater ability of self-renewal as well as their high differentiation potential into all the 3 primary germ layers. On the other hand, they can easily form *in vivo* teratomas. An additional critical point is related to their human embryo derivation that raises ethical concern [8]. The undifferentiated state and self-renewal capability are maintained thanks to the expression of specific transcription factors, namely Nanog and octamer-binding transcription factor 4 (Oct4) [9–11]. Interestingly, the recent progress in epigenetic reprogramming of adult somatic cells allow to obtain ESC-like cells named induced pluripotent stem cells (iPSCs), with comparable advantages and concerns, but avoiding the ethical problems, and it opened the way to a personalized cell therapy [12]. iPSCs were similar to human ESCs in terms of morphology, proliferation, differentiation, surface markers, and expression of pluripotent cell-specific genes as Oct3/4, SRY-related high mobility group box protein-2 (Sox2), the oncoprotein c-Myc, and Hruppel-like factor 4 (Klf4) [13]. However, the retroviral vectors and the reprogramming oncogenes (like c-Myc) used can cause cancers, and for this reason researchers are exploring new methods to generate iPSCs without genomic manipulations.

Fetal stem cells (FSCs) can be isolated from fetal tissue at the beginning of the second gestation trimester, such as amniotic fluid; even if these cells display lower stemness properties compared to ESCs [14], they are classified as broadly multipotent [15]. The main advantage of fetal, but also perinatal stem cells (PSCs), is that they can be easily isolated from left over samples from prenatal screening performed during the second trimester (i.e., amniotic fluid from amniocentesis analysis) or as clinical discarded material after birth (i.e., umbilical cord, or terminal amniotic fluid). Interestingly, FSCs show common characteristics with both embryonic and adult stem cells, maintaining high self-renewal potential, without tumorigenic and ethical issues [16].

Lastly, adult stem cells (ASCs), derived from different adult tissues, are multipotent stem cells. They are of advantage since, in addition to the allogenic source, also the autologous one is possible, and transplantation of own ASCs does not cause rejection problems [17]. Tissue-resident stem cells are considered ASCs that reside in a “stem cell niche”, a microenvironment that controls their self-renewal and differentiation capability [18,19]. Niche *stimuli* are fundamental for supporting resident stem cell maturation for the physiological cell turnover or for the cell replacement after injury [20–22]. Similarly, mesenchymal stem cells (MSCs) are noteworthy for their elevated differentiation plasticity (pluripotency) without forming teratomas [23], and relative ease of isolation and expansion [24]. MSCs can be obtained not only from adult tissues (such as adipose tissue, peripheral blood, bone marrow, and dental pulp), but also from fetal (such as umbilical cord, placenta, and amniotic fluid) or other tissues. Notably, MSC biological characteristics, including proteome, transcriptome, and surfactome profiles, can differ according to the different cell-sources [25–29]. To better understand the MSC therapeutic potential and to obtain reliable stem cell products for medicine application, the research is directed through the study of different approaches to improve homogeneity of MSC populations, as the antibody-selection for specific cell surface markers. Fetal or perinatal-MSCs can be considered a preferable alternative to adult MSCs, thanks to their early gestational derivation that leads to a reduction in carried environmental induced mutations. Ninety-five percent of MSC population expresses CD105, CD73, CD105 [30], while the ninety-eight percent does not express CD34 (hematopoietic progenitors and endothelial cells), CD45 (pan-leucocytes), CD14 or CD11b (monocyte/macrophages), and CD19 or CD79a (lymphocyte B). Additionally, the ninety-nine percent of MSCs is negative for HLA-DR (human leucocyte antigen-DR isotype), a MHC (major histocompatibility complex) class II cell surface receptor, if not stimulated by interferon-gamma (IFN-g). What is more, the expression of chemokine receptors allows them to migrate towards inflammatory areas and then exert their beneficial effects [31]. Indeed, MSCs can respond to injured tissue by releasing various mediators that can alter the damaged environment protecting the cells and promoting tissue regeneration. The secretome of these cells includes a wide range of factors, including growth factors, cytokines, and extracellular vesicles (EVs) (i.e., exosomes), and this characteristic allows them to operate *via* more than one mechanism, i.e., modulating the inflammation, reducing the apoptosis and oxidative stress, and increasing the angiogenesis [32].

Concluding, MSC characteristics make these cells promising candidates for a wide range of biological and medical application [33], including the treatment of degenerative disorders.

1.2 Amniotic Fluid Stem Cells and their secretome

The significant advance in regenerative medicine has increased the interest in novel sources of stem cells with potential application in medicine [1]. Recently, amniotic fluid (AF) has been proposed as a potential source of stem cells since its interesting content in stem cells, ease of obtaining, reduced ethical features, and various possible applications. AF is mainly composed of water and electrolytes, chemical substances (such as lipids, proteins, and hormones), suspended materials, and cells. Thus, depending to the different gestation phases and fetal development, this composition and volume change: during the first half of gestation, the volume depend on the osmotic gradient created by sodium chloride, and AF principally contains fetal skin cells, while, during the last half, we can also find fetal respiratory secretions, urine, and excrements. The AF-contained cells consist in a heterogeneous population, principally derived from the embryo, namely the amniotic membrane, but also from respiratory, urinary, and intestinal tracts. The first hypothesis that AF could contain undifferentiated cells came from a study of Streubel et al., where they demonstrated that AF-derived cells, cultured with supernatants derived from a rhabdomyosarcoma cell line, expressed skeletal muscle proteins [34]. Moreover, subsequent research showed the capability of these cells to differentiate into osteocytes, adipocytes, and fibroblasts, as well as the presence of cell markers similar to those of MSCs [35]. Furthermore, the detection of Oct-4 expression, characteristic of ESCs and iPSCs, confirmed the presence of a subpopulation of cells (around 0.5-1%) with stemness potential [36]. This encouraging finding led to the necessity to separate these undifferentiated cells from total AF cells. To do that De Coppi et al., proposed CD117 (a type III tyrosine kinase receptor for stem cell factor) as discriminating marker, and performed both magnetic or fluorescent-cell sorting (MACS and FACS techniques) [37]. The CD117-positive cells, also identified as AF stem cells (AFSCs), are around the 1% of total AF cells and they can differentiate into all the three germ layers, as demonstrated by *in vitro* experiments [15]. Indeed, AFSCs were successfully differentiated into hepatocytes expressing albumin (endodermal potential), neural stem cells expressing Nestin and dopaminergic neurons (ectodermal potential), and myotubes, adipocytes, endothelial cells, and chondrocytes (mesodermal potential) [38]. Furthermore, in addition to Oct-4, AFSCs also express stage-specific embryonic antigen 4 (SSEA-4) pluripotency marker, while they lack in hematopoietic lineage (CD45) and hematopoietic stem cell (CD133, CD34) markers, confirming the absence of umbilical cord and fetal blood cell contamination [35].

In recent years, AFSCs have generated great interest for the development of novel therapies, thanks to their ease of isolation and maintenance *in vitro*, differentiation capability, and lack of tumorigenic risk and ethical concerns. In addition, these cells could be used not only for heterologous transplantation, but also as autologous stem cell source for pre- or postnatal regenerative treatments. Several evidence suggested that these cells can act beneficial effects on injured tissues *via* two possible ways: (1) differentiating into mature cells [15] and (2) releasing trophic paracrine factors which can stimulate endogenous pathways and promote tissue repair [39,40].

In view of these concerns, AFSC-secretome, which includes soluble molecules as well as released vesicles, has gained great curiosity for the possible development of a cell-free therapy [41,42].

1.3 Aging, oxidative stress, and age-related cellular features

Aging is a progressive physiological process characterized by degeneration in cellular and molecular structures, that leads to tissues and organs loss of function or efficiency [43,44]. During aging, physical and mental abilities decline gradually [45]. The mechanism of aging is not yet completely understood, however age-related conditions show chronic/persistent inflammation, increased reactive oxygen and nitrogen species (ROS/NOS - RONS) leading to oxidative stress (OS), and mitochondrial dysfunctions [46]. Indeed, OS increase has been observed in different age-related conditions, such as cardiovascular, neurodegenerative, and chronic kidney diseases, as well as sarcopenia and bone fragility [47–49]. Moreover, the "OS aging theory" links the progressive age-associated dysfunctions to RONS accumulation, which leads to a subsequent loss of homeostasis and damage of several macromolecules (lipids, DNA, and proteins) and tissues [50,51]. RONS are a group of unstable free radicals, which comprise hydroxyl ($OH^{\bullet}$), superoxide anion ($O_2^{\bullet -}$), nitric oxide ($NO^{\bullet}$) radicals, and non-free radicals, namely peroxynitrite ($ONOO^{-}$) and hydrogen peroxide (H_2O_2) [52]. RONS are normally produced during different amphibolic metabolic pathway processes and the two principal systems implicated in ROS generation include the mitochondrial oxidative phosphorylation (OXPHOS) and the nicotinamide adenine dinucleotide phosphate- ($NADPH^{-}$) oxidase (Nox) system. Importantly, mitochondria are the primary endogenous source because of their role in ATP production via the OXPHOS (during mitochondrial electron transport chain – ETC). Other physiological RONS sources are immune cells, that produce ROS through the Nox2 isoform for combating exogenous invaders, but also peroxisomes and microsomes, which mainly produce H_2O_2 [53]. Therefore, at low concentration RONS are fundamental messengers for the regulation of physiological cellular processes, such as cellular survival and defense, activation of transcriptional factors, and protein phosphorylation [54]. In healthy conditions, different enzymatic and non-enzymatic antioxidant defense systems protect cells and mitochondria from RONS damage. Among the enzymatic ones the most significant are glutathione peroxidases (GPXs), thioredoxins (TRXs), superoxide dismutases (SODs), peroxiredoxines (PRDXs), catalase (CAT), while among the non-enzymatic we can find for example glutathione (GSH), cytochrome C oxidase (complex IV), coenzyme Q, ascorbic acid, and vitamin E to cite a few [55–57]. Nevertheless, during aging the imbalance between ROS production and antioxidant defenses may lead to a pro-oxidant status which causes abnormal mitochondrial signaling and loss of homeostasis, increasing the ROS production and decreasing scavenging defenses in a vicious cycle[44].

Interesting hypotheses on the connection among oxidative stress, cellular senescence/aging, and inflammation have been proposed. Indeed, increased ROS levels can stimulate the p16/mitogen-activated protein kinases p38 (p38MAPK) and p53/p21 pathways leading to cell senescence, and thus to the progression of chronic degenerative diseases and aging [58,59]. Senescent cells acquire an irreversible senescence-associated secretory phenotype (SASP) that can stimulate a chronic inflammation state by secreting different soluble factors (i.e., cytokines, interleukins, chemokines, and growth factors), creating a low-grade chronic inflammation characteristic of aging called "inflammaging". Moreover, SASP are responsible of the downregulation of forkhead box (FOXO)-derived antioxidant proteins [59] (such as CAT, MnSOD, and TRX), mainly *via* sirtuin activity inhibition, that leads to the ROS increase. Sirtuins are a NAD^+-dependent deacetylase protein family implicated in several cellular processes, including DNA repair, apoptosis, mitochondrial biogenesis, and oxidative stress responses [60]. The main Sirtuins targets are the FOXO family transcription factors, fundamental for the cell adaptation to a various stressor stimuli, namely oxidative stress and growth factor deprivation. Interestingly, SIRT1 deacetylation of FOXO factors stimulates antioxidant expression, but also the SIRT1 strengthening *via* an auto-feedback loop. Additionally, SIRT1 has a role in controlling the inflammatory response inhibiting the tumor necrosis factor alpha (TNFα) and nuclear factor kappa-B (NFκB) [61]. Moreover, NFκB signaling is a potent inducer of NADPH oxidase components, such as gp91phox and p22phox, and it can also transactivate the iNOS expression, increasing the RNS production [62]. So, the loss of inhibition of these factors, due to Sirtuin down-regulation by SASP, promotes a proinflammatory state and, thus a further increase in the redox unbalance [63]. Furthermore, the crosstalk between SIRT1 and ROS promotes in a context-dependent manner the loss of efficiency in autophagy, a common aging hallmark together with inflammation and oxidative stress. Growing evidence reveals that the prevalence of an inflammatory phenotype in aged tissues could be also promoted by the age-related impairment in autophagy [64]. Indeed, Sirt1 is a potent autophagy inducer that can directly regulate the autophagosome formation, but it can also indirectly regulate autophagy *via* FOXO signaling. In fact, FOXOs can up-regulate the expression of different autophagy-related genes in muscle cells, neurons, cardiomyocytes and bone cells (***Figure 1***).

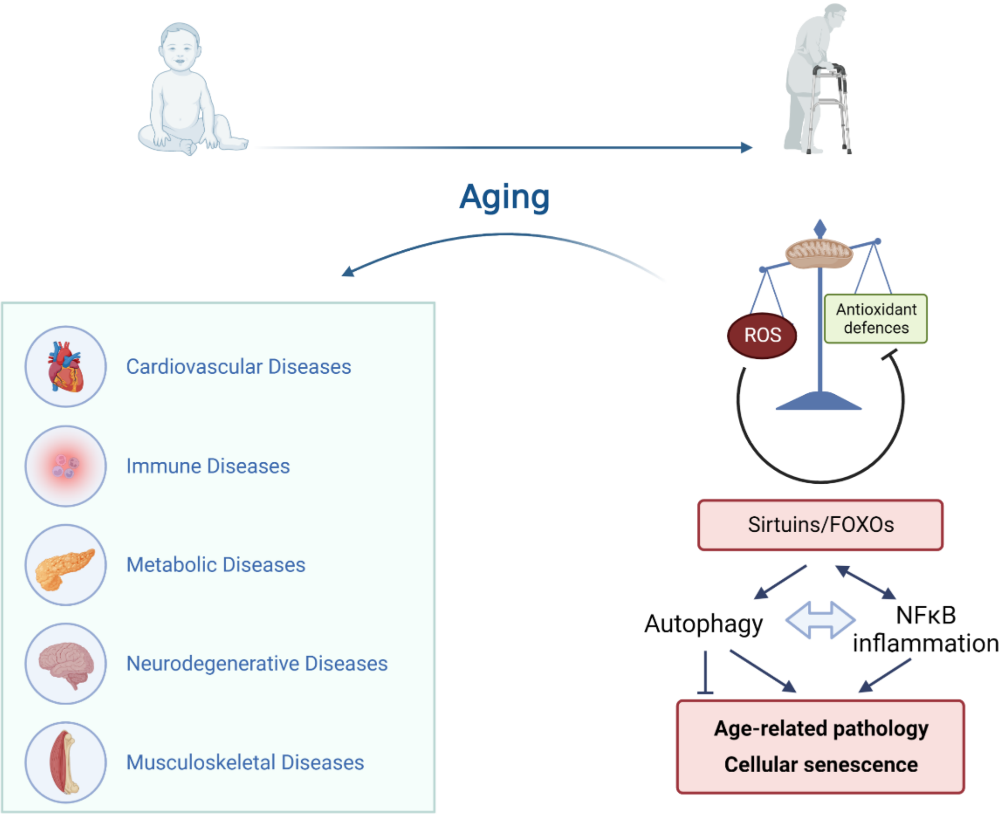

Figure 1: Schematic overview of oxidant unbalance and Sirtuin/FOXO implications in age-related diseases. Image Created with BioRender.com.

.

Concluding, mitochondrial dysfunctions, accumulation of damaged cellular components, genomic instability, loss of proteostasis, cellular senescence, and stem cell exhaustion are the main consequences of redox unbalance that occurs during aging [65]. The research of innovative compounds that can counteract human aging and related biological consequences is ongoing, and among the treatments proposed there is also the stem cell application, thanks to their immunomodulatory, antioxidant, and regenerative potential.

1.4 Application of mesenchymal stem cell therapy in aging

The increase in life expectancy leads to the aging of the global population, increasing the prevalence of aging frailty [66]. Due to its complex pathophysiology, effective treatments for the prevention of this syndrome are still not approved [67]. Since, MSCs can exert regenerative and anti-inflammatory effects, their application represents a promising therapeutic strategy for several degenerative diseases. Indeed, current evidence has demonstrated that MSCs could improve the frailty status by supporting the correct function of different organs, like heart, muscle, brain, and endocrine system [67]. Actually, *in vivo* and *in vitro* studies demonstrated the efficacy of MSCs in promoting neurogenesis and improving the neurological state in models of age-related neurodegeneration [68,69]. Interestingly, it has been documented that intravenous injected MSCs can cross the blood brain barrier (BBB), a fundamental requisite for neural efficiency [70–72]. Furthermore, pre-clinical studies demonstrated the cardioprotective effects of MSCs and their ability to promote cardiac functions through different mechanism, including endothelial cells and cardiomyocyte differentiation ability and promotion, angiogenesis stimulation *via* paracrine *stimuli*, and fibrosis and heart damage reduction [73–75]. Imbalance between anabolic and catabolic hormones and the decline in their total amounts are recognized as promoters of frailty pathogenesis and disease progression [76]. Notably, it has been demonstrated that MSC transplantation could recover several hormone levels back to normal, such as testosterone and insuline-like growth factor 1 (IGF-1) [77,78].

To date, MSC transplantation has undergone the phase I and II trials in humans, which have given positive results about their safety and efficacy for aging frailty [67]. For instance, Aging FRailTy *via* IntravenoUS Delivery (CRATUS) went through phase I and II steps, that reported beneficial effects of BM-derived MSC transplantation in patients with aging frailty [79]. The treatment group had increased 6-minute walk performance at 3 and 6 months after transplantation and decreased inflammatory cytokine TNF-α levels (6 months). Among the dose-divided group, the 10^8 cell-dose-group showed the best performance improvement in 6-minute walk distance, cognitive status and physical function, and no adverse reactions have been registered within 1-month post injection. Despite the positive results, these two trials required additional studies to obtain a more convincing conclusion.

In the recent years, different failure in MSC clinical applications were however encountered, probably due to the methodological variability of culture, poor survival rate after *in vivo* transplantation, and changeable ability to migrate, adhere, and engraft to the injured site [80–82]. The application of different MSC derivates, such as EVs, may be more effective and preferable than the direct MSC use. The way to go before considering MSCs as an ideal clinical treatment for age-related disease is still long, but the positive results obtained to date gives encouraging perspective.

2. Aim of the project

Aging is a progressive physiological process characterized by physical and cognitive gradual decline, due to the degeneration of cellular and molecular structures, and consequent tissue and organ loss of efficiency [43,44]. All the age-related diseases share a low-grade of chronic inflammation as well as increased oxidative stress state due to ROS overproduction and mitochondrial dysfunctions [46]. The complex pathophysiology of aging makes bankruptcy the development of effective treatments [67]. In recent years, it has widely demonstrated the regenerative, anti-inflammatory, and antioxidant potential of different types of stem cells, and MSCs as well [67,83]. The main limits of stem cell clinical application are represented by the poor survival rate after *in vivo* transplantation, and variable ability to migrate, adhere, and engraft to the target damaged site [80–82]. For these reasons, the research has been recently directed through the study of cell-free SC derivatives, namely extracellular vesicles and exosomes. Among the different MSC sources, the amniotic fluid has aroused great interest given its easy obtainability from pre-natal screening waste samples, low ethical issues, and its content in stem cells. Indeed, AFSCs are defined as broadly multipotent, since their capability to differentiate into the three embryonic cell lineages, and expression of Oct-4 and SSEA-4 pluripotency markers [38].

Based on these considerations, the principal aim of this study was to investigate the therapeutic potential of extracellular vesicle-derived from AFSCs in counteracting the detrimental consequences of aging in the most aging-affected areas of the human body: skeletal bone tissue, muscle and NMJs, and brain.

For this purpose we set up *in vitro* models of osteoporosis, muscle atrophy and Alzheimer’s disease. For a greater ease of reading of this thesis works, it was decided to divide it into 4 main chapters.

In the first one, it was discussed about EV studies as well as the scientific debate on their definition and isolation. Indeed, the title of my PhD project contemplates the use of “exosomes” term, which however has been cautiously replaced over the years, as in this thesis work, with the more generic term of extracellular vesicles. Moreover, our recent change in the isolation method applied, from a commercially available kit to the ultracentrifugation one, made necessary the evaluation of possible differences between the obtained EVs.

In Chapter II, the AFSC-EV therapeutic potential was investigated in an *in vitro* model of osteoporosis obtained by the treatment of human pre-osteoblast cell line (HOB) with a synthetic glucocorticoid, the Dexamethasone (Dexa).

Then, Chapter III summarized the work carried out, at least in part, during my mobility PhD period in 2021. Indeed, thanks to the collaboration with the Professor Maurilio Sampaolesi, PI at the Stem Cell Institute of Leuven (Belgium), we set up an *in vitro* model of muscle atrophy between human mesangioblast-derived myotubes and iPSC-derived motor neurons, using microfluidic devices. This allowed us to investigate the NMJ and neuron perturbation transmitted by atrophic myotube, and then the restorative potential of AFSC-EVs.

Lastly, in Chapter IV the AFSC-EV effect was evaluated on the most widespread age-related brain disease: Alzheimer's disease. Primary neurons from transgenic 5xFAD newborn mice were used to investigate the direct effect of these vesicles in counteracting the neurodegenerative features. After that, the indirect effect of EVs on neurodegeneration *via* the reduction of neuroinflammation was also evaluated. To do that, SH-SY5Y neuroblastoma cells treated with amyloid-β, as a more applicable AD model, were indirectly exposed to activated BV2 microglial cells (namely to their conditioned medium exposure), or but also directly using transwell co-culture systems.

Particular attention was directed through the AFSC-EVs modulation of oxidative stress and autophagy balance, principally acting on SIRT/FOXO signaling pathway, as well as their pro-differentiative, and regenerative potential on injured tissues.

Collectively, all the results obtained during these three years could help to improve the knowledge on the potential mechanisms of action of AFSC-EVs as a cell free therapy in the treatment of different age-related diseases.

Chapter I – Extracellular Vesicles derived from human AFSCs: comparison between two isolation methods

3.1 Introduction

3.1.1 Extracellular Vesicles: microvesicles, exosomes and others – Origin, composition, and purpose

Intercellular communication is a fundamental process for multicellular organisms, and it could be acted by direct cell-to-cell contact or by factor secretion. Extracellular vesicles (EVs) represent an important vehicle for carrying into the extracellular space different messengers and biomarkers [84,85].

Extracellular vesicles include microvesicles (MVs), exosomes (Exo), and apoptotic bodies, that are lipid bound vesicles which differentiate for their biogenesis, releasing pathway, content, size, and function [86–88]. The cargo of these vesicles is strictly dependent on the originating cells, but in general it could include lipids, nucleic acid (such as DNA, small RNA, and microRNA), and proteins. It is important to underlie that in literature the generic term of EVs is mainly used to indicate small EVs, namely Exo and MVs, excluding apoptotic bodies.

A brief description of characteristics, origin, and function of these vesicles, focusing on Exo and MVs, those of main interest for this thesis work, is reported below.

Exosomes are single layer lipid membrane vesicles, secreted by all cell types and contained in several biological fluids, such as plasma, serum, urine, saliva, cerebral spinal fluid (CSF), and amniotic fluid [84]. Exo have endosomal origin and its size is typically comprised between 30-150 nm, even if there are still many controversies since some plasma membrane-derived vesicles with similar size are also called exosomes [85–90]. Exo vesicles are formed from inward budding of early endosomes membrane, and initially take the name of multivesicular bodies (MVBs) (***Figure 2***). MVBs are involved in protein metabolisms (i.e., sorting, recycling, storage, transport, and release) [86], and after their formation they could be sent to lysosomes to be degraded together with their content, or released into the extracellular spaces, such as Exo, by fusing with the plasmatic cellular membrane [91–93]. The driving factors of MVB specific fate are not yet clear [85]. Exo formation and transport are regulated by Endosomal sorting complex required for transport (ESCRT) proteins, which, together with their accessory proteins (Alix, tumor susceptibility gene 101-TSG101, heat shock cognate protein-HSC70, and heat shock protein 90 beta-HSP90β) are considered exosomal protein markers [94–98]. Moreover, the transmembrane tetraspanin family proteins, CD63, CD9, and CD81, are also commonly found on Exo membrane, as well as on MVs surface, and for this reason they appeared enriched in vesicles samples compared to the total cell lysate [99,100]. On the contrary, Exo and MVs should be negative for intracellular proteins associated with different compartment than plasma membrane or endosomes, such as endoplasmic reticulum (HSP90β1, calnexin), Golgi (Golgi marker 130-GM130), mitochondrial (cytochrome c), nucleus (histones), and argonaute/RISC complex proteins [101]. Moreover, compared to the vesicles derived from cellular plasma membrane, Exo are enriched in cholesterol, shyngomyelin, hexosylceramides, and saturated or monounsaturated fatty acid [85]. Importantly, the Exo cargo also include mRNA and miRNA, that could be transfer to the recevitory cell and here translated into proteins. Different studies linked the Exo-contained RNAs to the originating cell, index of a selective loading of RNA into these vesicles [102–104].

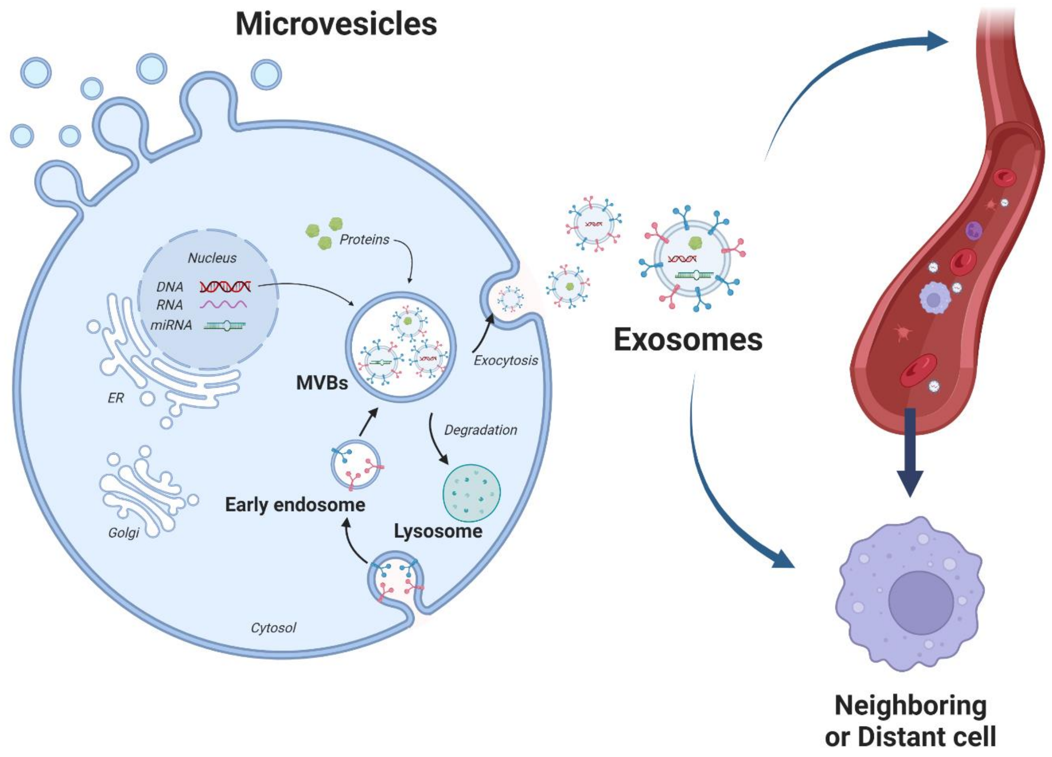

Figure 2: Schematic overview of MV and exosome origins. Image Created with BioRender.com.

Despite the absence of specific markers to perfectly distinguish Exo from MVs, their derivation source is completely different: indeed, MVs originate by direct outward budding, or pinching, of the cell plasma membrane. Moreover, their size is higher, from 100 nm to 1 µm [85–88,90]. Even if the exact mechanism is not well understood, cytoskeleton components, like actin and microtubules, as well as dynamic proteins (kinesins and myosins) and fusion proteins (SNAREs and tethering factors) seem to be fundamental for MVs formation [84]. As a result of their origin, MVs are enriched in cytosolic and plasma membrane associated proteins (including tetraspanins) [105,106], but also cytoskeletal proteins, heat shock proteins, integrins and post translational modified proteins (glycosylated and phosphorylated proteins) [107–109]. The presence of cytosolic and plasma membrane proteins is a characteristic point related to their origin, and the absence of organelle-associated proteins could be an easy way to distinguish them from total lysate and apoptotic bodies [100,110]. However, these proteins cannot be used to discern MVs from Exo [111].

As anticipated, MVs and Exo are involved in the cell-to-cell communication, cell maintenance, and tumor progression. The EV uniqueness is their ability to package, protect, and specifically target active molecules to neighboring or distant cells [88]. This ability made them of particular interest as a carrier of biomarkers for different pathologies, including Parkinson's disease [112,113], glioblastoma [114], kidney injury [115], just to name a few. Furthermore, the numerous advantages of Exo, including a long circulating half-life, great tolerability by the human body, capability to cross cellular membranes as well as the blood brain barrier, and the possibility of engineering for specific targeting, make them a promising candidate for the development of drug delivery systems [116,117]. Lastly, several recent studies highlighted the beneficial effect of MSC derived-exosomes against tissue damage and degenerative disease progression [118]. Indeed, recent studies on MSC-derived secretome, and in particular EVs, highlighted their capability to mimic all the therapeutic effects produced by the originating cells, including tissue repair, immune system and oxidative stress regulation. MSC-EV specific cargo contains mRNAs, miRNAs, and proteins that can be transferred to the recipient cells, and this ability makes these vesicles more advantageous than MSCs. Furthermore, MSC-EV storage, transfer, and production are easier, and their administration is also safer than MSC therapy [119].

Even if the potential medical and clinical applications of these vesicles are numerous, more standardized methods to isolate and characterize EVs are needed in order to obtain more reproducible therapies.

3.1.2 Isolation methods and analysis

The wide range of potential clinical applications of EVs, in particular Exo, are however accompanied by the absence of standardization in the isolation methods. The original method of Exo isolation is the ultracentrifugation, still considered as the gold standard today, nevertheless cheaper, faster, and more applicable methods have been developed. Despite these alternative methods (listed in ***Table 1***) have been developed to separate Exo from total EVs by size, immunoaffinity, or precipitation capability characteristics, they often fail and result in complex EVs mixtures together with other extracellular space components [87,88]. This drawback is mainly due to the complex composition of biological fluids or culture medium (which are often enriched in fetal bovine serum, FBS), to the similar physical, chemical and biological characteristic of Exo and EVs, as well as to the heterogeneity inside Exo subpopulations [120,121].

Table 1: Summary of the principal EV isolation techniques [84].

ISOLATION TECHNIQUES	SEPARATION PRINCIPLES	TYPES	REF.
ULTRACENTRIFUGATION TECHNIQUES	Density Shape Size	Differential ultracentrifugation	98
		Density gradient centrifugation	122
		Rate-zonal centrifugation	123
		Isopycnic centrifugation	123
SIZE BASED TECHNIQUES	Size	Ultrafiltration	124
		Exosome isolation kit (based on membranes)	125
		Sequential filtration	126
		Size exclusion chromatography (SEC)	127
		Flow field-flow fractionation (FFFF)	128
		Hydrostatic filtration dialysis (HFD)	129

IMMUNOAFFINITY CAPTURE-BASED TECHNIQUES	Antigen surface expression	Enzyme-linked immunosorbent assay (ELISA)	124,130
		Magneto-immunoprecipitation	124
EXOSOME PRECIPITATION	Precipitation using water excluding polymer	Polyethylene glycol (PEG) precipitation	124,131
		Lectin induced agglutination	132
MICROFLUIDIC BASED ISOLATION TECHNIQUES	Physical and biochemical properties	Acoustic nanofilter	133
		Immuno-based microfluidic isolation	134

Below, only the two methods used in this work will be discussed: differential ultracentrifugation and Polyethylene Glycol (PEG) precipitation methods.

The first method used by researchers for Exo isolation, from biological fluid but also cellular medium, was the differential ultracentrifugation [135–137]. First, cellular debris and larger particles are pelleted out from the matrix with a 500× *g* centrifugation. Then, thanks to a 0.22 µm filtration and a 10000× *g* step, larger EVs and apoptotic bodies are removed. Finally, two 100000× *g* ultracentrifugations permit to pellet out and wash exosomes. The ultracentrifugation time is directly linked to the isolation yield but also to the exosome damage (high damage for time > 4 hours), and as a consequence to soluble protein contamination [138]. However, less than 4 hours 100000× *g* step results in an exosome enrichment and not in a complete isolation [88]. Principal disadvantages of this technique are the need for technical expertise, high time consuming, and larger starting sample volume requirement (several mL), that make the simultaneous process of several biological samples difficult. Based on this, commercially available kits are being developed as “easy isolation procedures” and, among these, we can find the PEG precipitation techniques. The PEG polymer excludes water molecules favoring exosomes, and other particles, pelletization. The related advantages are numerous, such as shorter time and little technical expertise, simplicity, absence of expensive equipment necessity, and large variety of applicable starting volumes (from 100 µL to several mL) [124]. Despite the numerous advantages, the main limit of these products is their frequent inability to separate differently sized EVs [85]. To reduce contaminations, sample pretreatment such as filtration and/or ultracentrifugation, are recommended [124].

Due to the difficulties to obtain exosome pure final products, post-isolation content analyses are fundamental. Protein quantification is an easy and quick method to characterize isolated EVs, even if the concentration is typically overestimated due to contamination, and it does not consider the quality of protein cargo [88]. Thus, the most common analyses evaluate the physical and chemical/biochemical/compositional characteristics. Physical analyses give information on particle size and/or concentration, and they include nanoparticle tracking analysis (NTA), dynamic light scattering (DLS), and electron microscopy [84]. NTA, for example, allows the determination of concentration and size distribution of isolated EVs, analyzing the Brownian motion of vesicles in suspension [139]. The chemical/biochemical/compositional analysis gives information on isolated vesicles content, and it could be performed through staining, immunoblotting, or proteomic analysis. Interestingly, different proteomic profiles are obtained from EV samples isolated from the same cell line but by using different isolation methods [87]. This intriguing finding highlights the necessity of standardized and reproducible (new) isolation methods.

3.1.3 MISEV: guidelines and practical controversies

As already discussed, the major on-going challenge in the EV field is to improve and standardize EV isolation, analysis, and characterization. To do that, the International Society for Extracellular Vesicles (ISEV) has grouped the main experts in the EV area in order to provide a series of minimal standard criteria for EV isolation/purification, characterization, and functional investigation. This editorial work took the name of "minimal experimental requirements for definition of extracellular vesicles (EVs)" or "minimal information for studies EVs (MISEV)", and it was published in the *Journal of Extracellular vesicles* in 2014 [101].

The first critical point discussed was about the term "exosomes", that is commonly used to indicate any type of EVs. However, several publications specify the endosomal derivation of Exo, unlike that of EVs originating *via* cell membrane budding. Unfortunately, a list of specific markers has not yet been drawn up to distinguish among different EV subtypes and, for this reason, MISEV2014 recommended a prudent use of the term "exosome". Since the actual meaning of "exosome" is not universally accepted, the general term "extracellular vesicles" will be used in this work.

In October 2016 a 14-question MISEV survey was released to the ISEV membership, and the outcomes highlighted the necessity of regular updates, together with the strong commitment of the ISEV community to advance the field by standardization efforts [140]. In fact, in 2018 the previously drawn up guidelines have been updated with MISEV2018 [141].

The numerous points discussed in MISEV2018, and briefly summarized below in ***Table 2***, are intended to provide the basis to discriminate between EVs and non-EVs, and, above all, to build the bridge direct through the reproducibility [140].

Table 2: Summary of MISEV2018 guidelines [141].

NOMENCLATURE	Since consensus has not yet emerged on specific markers of EV subtypes, “Extracellular vesicle” is the preferred generic term for the subject of our investigations, and subtypes should be defined by physical and biochemical characteristics and/or conditions/ sources. When other terms are used, careful definition is required.
SOURCE	Possible sources are: - Cell culture conditioned medium - Biological fluids - Tissue
EV SEPARATION AND CONCENTRATION	- There is no single optimal separation method, so choose based on the downstream applications and scientific question. Separation of non-vesicular entities from EVs is not fully achieved by common EV isolation protocols, including centrifugation protocols or commercial kits that claim EV or “‘exosome’” purification. - Report all details of the method(s) for reproducibility.
EV CHARACTERIZATION	**Quantification of EVs:** Both the source of EVs and the EV preparation must be described quantitatively. For the EV preparation, there is no single perfect quantification method. The most used are total protein amount and total particle number. Total lipid quantification could be also considered.
	Characterization of EVs by their protein composition: At least one protein of each category 1 to 3 must be evaluated in any EV preparations. Analysis of proteins of category 4 is required when claiming specific analysis of small EVs, and of category 5 to document functional activities. Cat. 1: transmembrane or GPI-anchored proteins associated to plasma membrane and/or endosomes Cat. 2: cytosolic proteins recovered in EVs

	Cat. 3: Major components of non-EV co-isolated structures Cat. 4: transmembrane, lipid-bound and soluble proteins associated to other intracellular compartments than PM/endosomes Cat. 5: secreted proteins recovered with EVs
	EV protein content analytic approaches: - Western blot - ELISA - Flow cytometry (FACS) - Mass spectrometry
	Single vesicle analysis: Characterization of single vesicles: use two different but complementary techniques, for example: 1. electron or atomic force microscopy (and show both close-up and wide-field) 2. single particle analyzers (not electron microscope-based)
FUNCTIONAL STUDIES	- Determine the specific versus common functions of different types of EVs - Demonstrate that the activity is observed in the absence of direct cell-cell contact - Demonstrate that the activity is predominantly associated with EVs rather than with soluble mediators - Demonstrate the specific association of the activity with EVs rather than with co-isolated components - Determine whether a function is specific to exosomes, as compared with other small EVs - How to attribute particular effects mediated by EVs to specific EV components - Consider whether an EV-dependent function is specific to a given EV source
GENERAL CONSIDERATIONS	**Reporting requirements**
	Exceptions to compliance with MISEV guidelines: Finally, there are exceptions to every rule. MISEV2018 is meant to guide and improve the field, not stifle it. If MISEV recommendations and requirements cannot be met, authors will then need to explain their unique situation and describe their attempts to meet the guidelines and the reason for failure. These guidelines will also continue to evolve.

3.2 Materials and Methods

3.2.1 Amniotic fluid collection

Amniotic fluids were collected from 3 healthy pregnant women (age: 27-43) between the 16th and 17th week of gestation during amniocentesis procedure performed at the Unit of Obstetrics and Gynaecology at the Policlinico Hospital of Modena, Italy. Amniocentesis were performed under continuous ultrasound guidance, in a sterile field, with 23-Gauceneedles. The related risks of the procedure and the aim of the study were explained to all patients before the procedure and the ob-gyn specialist collected a signed consent form before starting the exam (protocol 360/2017, dated 15 December 2017 and approved by Area Vasta Emilia Nord). Amniotic fluids were centrifuged, supernatants were discarded, and the cellular pellets were re-suspended. Amniotic fluid cells (AFCs) were seeded in culture to be expanded and used for diagnostic procedures. AFCs were maintained in Amniochrome™ - II complete medium (Lonza Bioscience, Rome, Italy). Supernumerary (unused) T25 flasks of amniotic fluid cells, cultured in the Laboratory of Genetics – TEST Lab in Modena (Italy) for 2 weeks, were used for subsequent manipulation.

3.2.2 Amniotic fluid stem cell isolation and culture

To obtain c-kit (CD117) positive cells, also known as human amniotic fluid stem cells (hAFSCs), which represent a subpopulation of AFCs with high stemness properties [37], cells were expanded in αMEM culture medium supplemented with 15% fetal bovine serum (FBS) (Gibco, Waltham, MA, USA), 2 mM L-glutamine, 100 U/mL penicillin, and 100 µg/mL streptomycin (all from EuroClone Spa, Milano, Italy) to reach at least 5 million of cells before isolation. C-kit positive cells were isolated using the immunogenic method MACS technology (Miltenyi Biotec, Germany). According to protocol, cells were trypsinized, resuspended in 10 ml of Buffer I (composed by PBS containing 20% FBS and 2 mM EDTA), and filtered through 100 µm cell strainer. After, cell suspension was centrifuged (300 x *g*, 5 min at RT), and cellular pellet was resuspended in Buffer II (composed by PBS containing 2 mM EDTA, 0,5%$_{m/v}$ BSA) with microbeads antibody dil. 1:50 and incubated at 4°C for 15 min under agitation. The ratio Buffer II/cells is approximately 500 µL/5 million cells. After incubation, cells were washed with Buffer II and resuspended in 500 µL of Buffer II. Then, a magnetic column from kit was conditioned by Buffer II and located on the magnetic hold.

After that, cell suspension was loaded into the column and eluted c-kit negative cells were collected. To collect all these cells, three consecutive washings with 500 µL of Buffer II were performed. Then, the column was removed from magnetic support and put into a 15 mL falcon tube. C-kit positive cells were collected washing 3 times with αMEM medium (Corning, MA, USA). hAFSC obtained are around 1-5% of total AFCs. hAFSCs were subcultured at 1:3 dil. once reached 70% confluence. Cells were grown in complete αMEM culture medium as previously described.

3.2.3 Conditioned medium collection

hAFSCs were grown in 175 cm^2 flasks until subconfluence (around 4×10^6 cells). Then, cells were washed once with PBS and maintained for 4 days in 20 mL culture medium without FBS, to exclude extracellular vesicles contamination from FBS solution. Conditioned medium (CM) was collected and centrifuged at 300 x *g* for 10 min at RT to eliminate cellular debris. Supernatant was concentrated up to 2 mL by using Centrifugal Filter Units with 3K cutoff (Merk Millipore, MA, USA) [41].

3.2.4 Extracellular vesicles isolation by Invitrogen^{TM} Total Exosome Isolation kit from CM

Total Exosome Isolation solution from cell culture media (Invitrogen, Life Technologies, CA, USA) is a commercially available kit proposed for the separation of exosomes from cellular conditioned mediums (CMs). It is a water excluding precipitation method. According to the manufacturer's protocol, concentrated CM was incubated with Total Exosome Isolation solution from cell culture media (ratio 1:1) (Invitrogen, Life Technologies, CA, USA) overnight at 4°C under agitation. The day after, the mixture was then centrifuged at 10 000 x *g* for 1 h at 4°C. The pellet, enriched in extracellular vesicles (EVs) and including exosomes (exo), was collected.

3.2.5 Extracellular vesicle isolation by ultracentrifugation

Concentrated CM was again centrifuged at 10 000 x *g* for 30 min at 4°C to exclude small cellular debris and, then, the supernatant was transferred into polypropylene ultracentrifuge tubes (13.5 mL, Beckman Coulter) and ultracentrifuged at 100 000 x *g* for 90 minutes at 4°C in a Beckman Coulter Optima L-90 K centrifuge (SW-41 rotor); the supernatants were discarded and the pellets were resuspended in 13 mL D-PBS (Corning, VA, USA) and ultracentrifuged again at 100 000 x *g*, 90 minutes at 4°C) [142]. The pellet was collected and stored at -20°C until use.

3.2.6 Nanoparticle tracking analysis (NTA)

EV pellets were resuspended in 100 µL D-PBS. After appropriate dilution, size distribution and concentration were evaluated by the ZetaView particle tracker from ParticleMetrix (Inning am Ammersee, Germany).

3.2.7 Transmission electron microscopy (TEM) analysis

EV pellets were resuspended in a fixative solution composed by 0.1 M phosphate buffer (pH 7.4) with 4% paraformaldehyde and 4% glutaraldehyde for 15 minutes at room temperature and kept at 4°C until the analysis. For the analysis, a drop of each sample was placed on a carbon-coated copper grid and let dry. Then the supports were immersed in 2% phoshotungstic acid solution (pH 7.0) for 30 seconds. The preparations were examined under TEM (JEM-1200EX, JEOL Ltd., Japan) at an acceleration voltage of 80 kV.

3.2.8 Extracellular vesicle extract preparation and protein quantification

Extracellular vesicle pellets were treated with lysis buffer (820 mM Tris-Cl pH 7.0, 1% Nonidet P-40, 150 mM NaCl, 10% glycerol, 10 mM EDTA, 20 mM NaF, 5 mM sodium pyrophosphate, and 1 mM Na_3VO_4) added with a protease inhibitor cocktail and para-nitrophenylphosphate (all from Sigma Aldrich, Milan, Italy) at a ratio of 3:2 ($v_{\mathrm{EVs}}/v_{\mathrm{LB}}$) at 4°C for 20 minutes. Lysates were sonicated, cleared by centrifugation (12 000 rpm for 15 minutes, 4°C) and protein quantification was performed using Bradford method. Into a 96 multi well plate, to 160 µL of MilliQ water were added 1 µL of each sample lysate and 40 µL of Bradford reagent (Bio-Rad, CA, USA). Absorbance was immediately read at 595 nm using a multi well reader (Appliskan, Thermo Fisher Scientific, Vantaa, Finland). After protein quantification, lysates were boiled in SDS sample buffer (Tris-Cl 1 M pH 6.8, SDS

10%, glycerol 30%, bromephenol blue 0.012%, dithiothreitol 0.6 M) for 5 minutes and stored at 4°C until use.

3.2.9 SDS PAGE and Western Blot (WB)

EV processed lysates were loaded in SDS gels 1.55 mm thick with 12% polyacrylamide running part and 4% polyacrylamide stacking part. For all the analyses at least 20 µg of proteins were loaded and 6 µL of Precision Plus Protein™ Standards Dual Color (Bio-Rad, CA, USA) was used as molecular weight indicator. Protein separation was carried out at 160 V for around 90 minutes at 4°C in the presence of electrolytic Tris Glycine SDS (TGS) Buffer (Bio-Rad, CA, USA). After separation, proteins were transferred from the gel to a polyvinylidenedifluoride (PVDF) membrane previously treated with methanol. Protein transfer was performed using a semi-dry method (12 V for 90 minutes) in Transfer Buffer containing 25 mM Tris, 190 mM glycine, and 20% methanol. To verify the correct protein transfer, the PVDF membrane was stained 1 minute with Ponceau Red, and after that it was washed with Tris Buffered Saline solution (TBS) (Tris 25 mM, KCl 3 mM, NaCl 140 mM pH 7.8) added with 0.1% tween (TBS-T) until disappearance of the coloration. Blocking solution, composed by TBS-T solution with 3% BSA (TBS-T+BSA), was incubated for 1 hour to block nonspecific binding sites, while primary antibodies diluted in TBS-T+BSA were incubated overnight at 4°C. The day after, the membranes were washed 3 times with TBS-T, and incubated with secondary antibodies in TBS-T+BSA (1:3000) for 1 hour at RT. Then, they were washed again before luminescence signal detection by a ChemiDoc™ Imager system (Bio-Rad, CA, USA) using Immobilon® Forte (Millipore, MA, USA. Relatively protein bands quantification was performed using ImageJ software. Primary antibodies used are against the following molecules: Rab5 (Lonza, SC, USA), CD9 (Life Technologies, CA, USA), CD81 (Thermo Fisher Scientific, MA, USA), SOD1 (Santa Cruz Biotechnology, CA, USA). Secondary antibodies were all from Thermo Fisher Scientific (MA, USA).

3.2.10 ELISA Assays

EVs were lysed by treating PBS-EV suspension with lysis buffer (previously described in *Section 3.2.8*) at a ratio of 1:3 (*v/v*) and performing 3 freeze-and-thaw cycles. 1 µg of total protein extract was quantified by TGFβ1, HGF, and IDO ELISA kits (all from Cusabio Technology, TX, USA) according to the manufacturer's protocol.

3.2.11 Statistical analysis

Experiments were performed in triplicate. For quantitative comparison, values were reported as mean ± SD based on triplicate analysis for each sample. One-way ANOVA with Bonferroni post hoc test was applied to evaluate the observed difference significance among the study groups. A p value < 0.05 was considered statistically significant. GraphPad Prism® release 6.0 software was used to obtain statistical analysis and plot layout.

3.3 Results

3.3.1 Size distribution and yield comparison between hAFSC-EVs isolated by Invitrogen^{TM} Total Exosome isolation kit and ultracentrifugation methods

First, we compared the morphological characteristics of EVs obtained by the commercial kit and ultracentrifugation. Transmission electron microscopy (TEM) showed that the average dimension of particles is around 100 nm (***Figure I.1A***) for both samples.

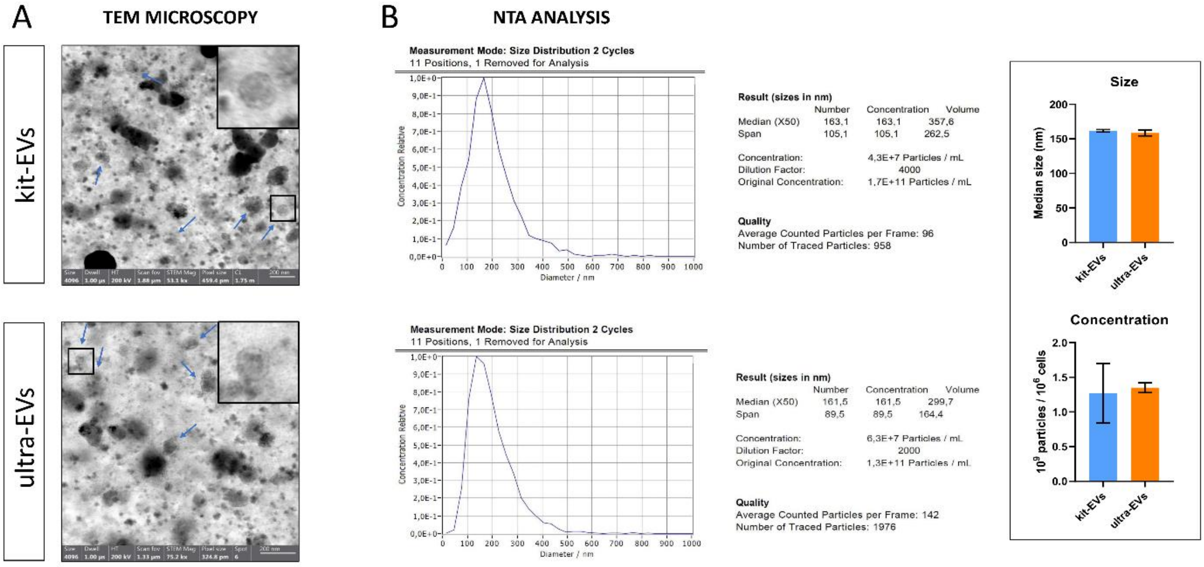

```
Measurement Mode: Size Distribution 2 Cycles
11 Positions, 1 Removed for Analysis

Result (sizes in nm)
                   Number    Concentration    Volume
Median (X50)        163,1        163,1         357,6
Span                105,1        105,1         262,5

Concentration:              4,3E+7 Particles / mL
Dilution Factor:                   4000
Original Concentration:     1,7E+11 Particles / mL

Quality
Average Counted Particles per Frame: 96
Number of Traced Particles: 958
```

```
Measurement Mode: Size Distribution 2 Cycles
11 Positions, 1 Removed for Analysis

Result (sizes in nm)
                   Number    Concentration    Volume
Median (X50)        161,5        161,5         299,7
Span                 89,5         89,5         164,4

Concentration:              6,3E+7 Particles / mL
Dilution Factor:                   2000
Original Concentration:     1,3E+11 Particles / mL

Quality
Average Counted Particles per Frame: 142
Number of Traced Particles: 1976
```

Figure I.1. Transmission electron microscopy and nanotracking analysis comparison between hAFSC-EV obtained from isolation kit and ultracentrifugation

(A) Representative TEM images of EVs obtained from isolation kit (top) and ultracentrifugation (bottom). Arrows indicate EVs. Scale bars: 200 nm.

(B) Representative nanoparticle tracking analysis (NTA) performed by Zeta view on EVs obtained from isolation kit (top) and ultracentrifugation (bottom) – left. On the right, graphs comparing median size – top – and concentration – bottom – of isolation kit and ultracentrifugation derived EV. Data shown are the mean ± SD (n=3). *p* values>0.05 (not significant).

Moreover, similar results were obtained by Nano tracking analysis (NTA): 163.1 ± 1.84 nm for kit-EV while 161.5 ± 4.24 nm for ultra-EV (indicated as average of median values) (***Figure I.1B***). Moreover, the number of EVs obtained using isolation kit and ultracentrifugation methods was similar, around 1×10^9 particles from 10^6 hAFSCs. Graphs in ***Figure I.1B*** showed no significant alterations in vesicles' size and concentration obtained by the two methods.

3.3.2 Protein content comparison between hAFSC-EVs isolated by Invitrogen^{TM} Total Exosome isolation kit and ultracentrifugation methods

Then, the protein content of EVs obtained by the two different isolation methods was investigated. Western blot analysis demonstrated a comparable quantity of typical EV surface markers, namely CD81, CD9, and Rab5, and the antioxidant protein SOD1 into both samples (***Figure I.2A***). Similarly, ELISA assay showed a similar content of anti-inflammatory and pro-regenerative molecules TGFβ1, HGF, and IDO (***Figure I.2B***).

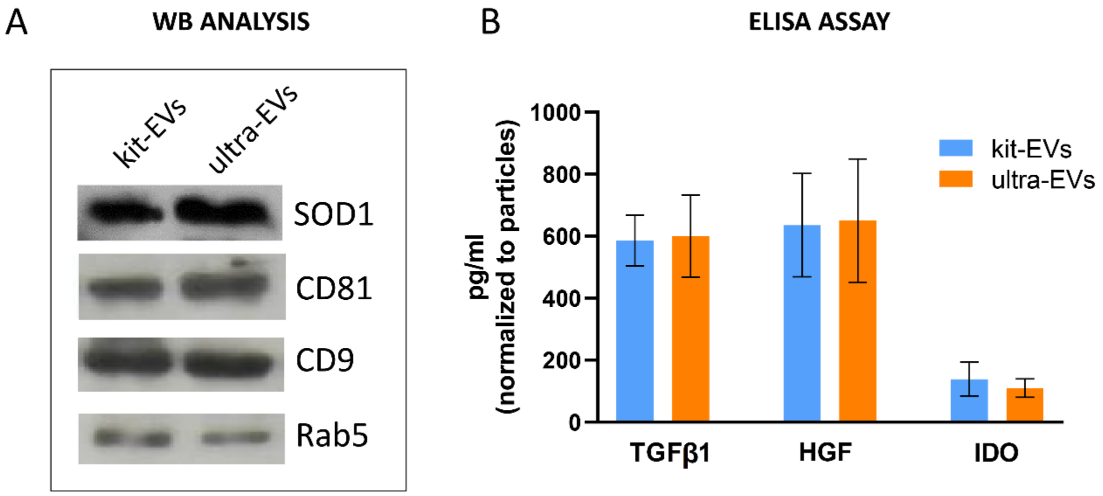

.

Figure I.2. Western blot and ELISA analyses on AFSC-EVs obtained from isolation kit and ultracentrifugation

(A) Representative images of WB analysis of kit-EV and ultra-EV total lysates revealing SOD1, CD81, CD9, and Rab5 protein levels.

(B) Graph representing ELISA analysis of TGFβ1, HGF, and IDO on the lysates of isolated EVs by the two different techniques. Data shown are the mean ± SD (n=3). *p* values>0.05 (not significant).

3.3.3 AFSC-EV sample collection

During my PhD, in our laboratory we collected 18 samples of AFCs, 14 of them were processed as previously described in order to obtain the EVs used in this project. The ***Table 3*** below summarizes the characteristics and the isolation method of AFSC-EVs used for each Chapter.

Table 3. Summary of AFSC-EV characteristics.

Chapter	***AF samples***	***AFSC-EV isolation method***	
		Exosomes Isolation kit	*Ultracentrifugation*
I- ***Extracellular Vesicles derived from Amniotic Fluid Stem Cells: comparison between two isolation methods***	3	✓	✓
II- ***Human AFSC-EVs counteract steroid-induced osteoporosis in vitro***	3	✓	
III- ***Human neuromuscular junction on a chip: impact of AFSC-EVs on muscle atrophy and nerve health***	3		✓
IV- ***Neurons and microglia in Alzheimer's disease: human AFSC-EVs protective effect against Aβ***	5	✓	✓

3.4 Discussion

In recent years, the interest in the study of extracellular vesicles has grown enormously given to their physio/pathological role in cell-to-cell communication and, their feasible use as disease biomarkers, but above all as a therapeutic strategy. Indeed, since their long circulation half-life, great tolerability by the human body, ability of not only penetrating cellular membrane but also potentially targeting specific cell types, EVs are considered promising candidates for the development of drug delivery systems [116,117]. In addition, it has been recently demonstrated that their content often reflects the characteristics of their parental cells, and it makes EVs interesting for cell-free therapy in stem cell and regenerative medicine [143–146]. Even if there is a wide range of potential applications of EVs, their use is widely debated from the scientific community since the lack in a unique definition and standardized methods for their isolation and characterization. For these reasons, we have encountered different obstacles in our research on hAFSC-derived EVs. Our first isolation approach, also used in some studies of this work, was by employing a commercially available kit based on the water exclusion principle (Invitrogen^{TM} Total Exosomes Isolation - from cell conditioned medium). Despite the numerous advantages of this method, its inability to separate differently sized EVs and membrane-free macromolecular aggregates makes it hotly contested. Some reviewers' criticisms led us to improve our isolation technique and opt for the ultracentrifugation method, considered the "gold standard" [84]. This methodological change has led to the necessity to evaluate the ultracentrifugation-derived EVs (ultra-EVs) and to compare them with those obtained from Invitrogen kit (kit-EVs). Thus, kit-EVs and ultra-EVs were examined in parallel basing on the official MISEV2018 criteria, in order to confirm the physical and biological similarity between the two types of EVs [141]. First, TEM analysis demonstrated the presence of round-shaped vesicles with a similar diameter in both samples, approximately 100 nm, comparable with that of exosomes and suggesting an enrichment in this type of vesicles. Notably, it also excluded the presence of vesicle aggregates as well as damaged vesicles, a possible inconvenience in the use of ultracentrifuge, given the high working speed and timing [138]. Consistently, NTA confirmed that most vesicles are around 160 nm in diameter and, at the same time, showed a similar size distribution for both suspensions, despite the different isolation approaches. This analysis also provided indications regarding the sample concentration, fundamental to determine the treatment volume. Interestingly, the similar number of starting cells/obtained particles ratio between kit- and ultra-samples suggested a comparable isolation yield from the two different techniques. Importantly, the treatment concentration is strictly connected to the experimental model (*in vitro* or *in vivo*), method of disease induction and cell type used, and for this reason no unique value could be established.

After confirming the similitude from the morphological point of view, we moved towards the EV content analysis. As recommended by the MISEV guidelines, the presence of typical EV markers, namely CD81, CD9, and Rab5, was detected in both samples in similar amounts. A recent study showed that different proteomic profiles could be obtained from EV samples isolated from the same cell line but using different isolation methods [87]. Considering that, the bioactive cargo of kit-EVs and ultra-EVs was compared. Interestingly, both our samples display similar amounts in antioxidant (SOD1) and anti-inflammatory proteins (TGFβ, HGF, and IDO), that we consider, at least partially, responsible for their *in vitro* positive effect in different degenerative diseases.

Finally, it is important to underline that slight variability among samples could occur since the complexity of EV-cell source, in particular the individual donor variability.

Collectively our results indicated that despite the different isolation methods, obtained EVs exhibit similar morphological and biological profiles, so they can be used in the same way for the *in vitro* study of human AFSC-derived EVs potential in counteracting age-related dysfunctions.

Chapter II – Human AFSC-EVs counteract steroid-induced osteoporosis *in vitro*

4.1 Introduction

4.1.1 Osteoporosis: bone and skeletal aging – From classification to cellular pathways

Osteoporosis is characterized by qualitative and quantitative defects of bone segments, and consequent strength loss that could lead to a reduction in fracture resistance [147]. From the clinical point of view, this complex skeletal condition could be classified in primary and secondary osteoporosis. The first is a systemic disease strictly related to aging, and it can occur in both men and women with age. Secondary osteoporosis includes a set of different alterations caused by different conditions or treatments; indeed, a common example is glucocorticoid-induced osteoporosis [148]. Moreover, age-related skeletal alterations increase the necessity of pharmacological treatments, including glucocorticoids (GC), aggravating the bone instability.

The bone loss occurring during age-related skeletal disorders is thought to be, at least in part, due to an imbalance in bone turnover [149]. Resident bone marrow-derived mesenchymal stem cells (BMSCs) have a key role in maintaining the correct balance in bone turnover, and, for this reason, several studies linked their alteration to osteoporosis occurrence [150]. Recently, Liang and colleagues [151] demonstrated that aging negatively affects BMSC proliferation and their osteoblastic differentiation potential, which can finally lead to osteoporosis. In light of these considerations, different studies recently demonstrated the positive effect of MSC secretome in recovering bone precursor cell ability to overcome senescence and apoptosis and reduce bone loss (as will be detailed in the following paragraph).

Another well-established cause of bone homeostasis imbalance is the increase in osteocyte death occurring during aging. Osteocytes are the most numerous long-lived bone cells trapped within the bone matrix and they are centrally involved in the regulation of bone erosion and deposition [152,153]. Apoptotic osteocytes are surrounded by osteoclasts that support dying bone cells and in parallel call other osteoclasts [154]. Among the main causes of osteocyte apoptosis during aging, we can find lack of hormones, disruption of blood flow as well as the oxidative stress increase [155]. Indeed, the ROS rise can trigger cell death principally by the activation of the mitochondria-dependent apoptotic pathway, which finally leads to the release of cytochrome c, and activated caspase3 and 9 [156]. The main mediators of this pathway are represented by the Bcl-2 family, which includes both pro-apoptotic (i.e., Bax, Bad, and Bak) and anti-apoptotic (i.e., Bcl-2, Bcl-X, and Bcl-w) members [156]. Moreover, recent evidence showed that oxidative stress and ROS can activate pre-osteoclast maturation and osteoblast apoptosis [152].

Recently, a strong court of studies claims that autophagy, as a cell survival pathway, plays a central role in maintaining bone homeostasis [157]. Cellular degradation and recycling of cytoplasmic proteins and organelles is mainly mediated by autophagic pathways. This process is fundamental for protein aggregate degradation and thus, in preventing cell toxicity. The decrease in autophagy efficiency and the impairment in protein homeostasis (proteostasis) have been associated with several age-related diseases, including osteoporosis [158]. Indeed, in aged rats' osteocytes it has been observed an age-dependent decrease of autophagy, associated with a reduction in related genes LC3β-II, BECLIN, and ULK-1 expression and a parallel rise of p62 expression and apoptosis (Pierrefite-Carle et al., 2015). To mimic skeletal aging, *in vitro* inhibition of autophagy in osteoblasts and osteocytes of young mice showed an increase in bone mass loss [160]. Nevertheless, different studies correlated the oxidative stress rise to autophagic pathway activation in osteocytes and osteoblasts, hypothesizing a possible defense mechanism against ROS-induced cell death (Pierrefite-Carle et al., 2015; X. Yang et al., 2019).

Among the different autophagy regulators, FOXOs and Sirtuins are the most interesting since their additional role in counteracting oxidative stress. Their physiological action is fundamental for skeletal development and bone homeostasis, while their alteration may contribute to bone diseases. Indeed, the inhibition of FOXO3, occurring during corticosteroid-induced osteoporosis, results in autophagy reduction and increases ROS levels [60] (***Figure 3***).

As already seen, the main target of sirtuins is the FOXO family. In bone tissue, FOXO deacetylation by SIRT1 prevents its association with β-catenin and improves Wnt signaling, increasing osteoblast proliferation. Moreover, the osteoblastogenesis stimulation by Sirtuins could be also mediated by direct action on β-catenin and RUNX2 [162,163]. On the contrary, FOXO loss of function promotes osteoclastogenesis and bone erosion leading to reduced trabecular and cortical bone mass. In osteoblast, FOXO attenuates ROS production and simulates cell survival, leading to bone formation, thanks to FOXO-induced antioxidant proteins and paracrine mechanisms, including osteoprotegerin (OPG) stimulation [164–168].

Concluding, similarly to different other age-related diseases, also in bone aging SIRT/FOXO axis plays a pivotal role in maintaining cellular homeostasis, thus it could be a potential therapeutic target for the treatment of bone loss.

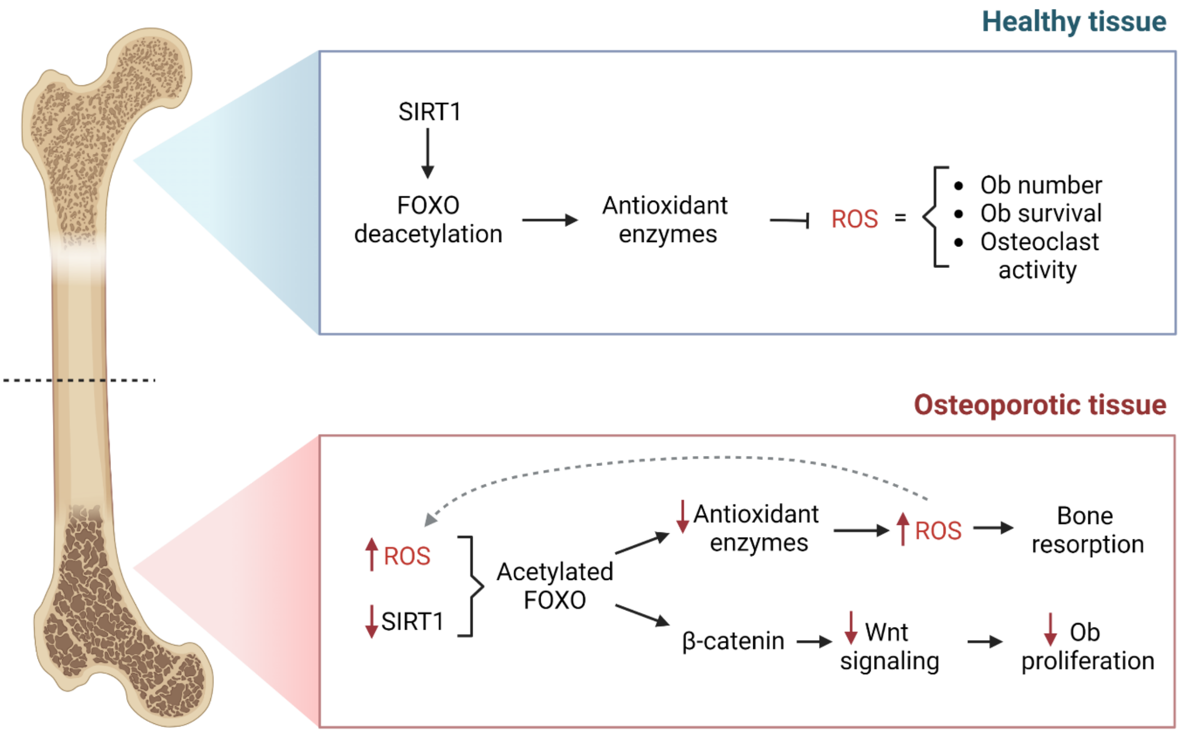

Figure 3: Schematic overview of SIRT1 and FOXO roles in aged osteoblast and osteoclast. Image Created with BioRender.com.

4.1.2 GIOP-induced osteoporosis: an experimental model to study bone aging

Glucocorticoids, such as Dexamethasone (Dexa), depending on concentration [169], can induce negative effects on skeletal bone tissue by increasing intracellular ROS that could lead to bone cell death, impairment in cell differentiation, and uncontrolled autophagy [170,171]. These side effects make them excellent candidates to set up *in vitro* and *in vivo* models to investigate the molecular mechanisms underpinned to skeletal aging and several bone-diseases, and to develop potential therapies.

Indeed, a study of Deng et al. [170] demonstrated the apoptotic effect of Dexa on osteoblasts *via* the ROS-PI3K/AKT/GSK3β signaling pathway. In primary osteoblasts from calvarial bones of newborn rats and murine pre-osteoblast cell line (MC3T3-E1), Dexa increased the ROS levels. This event produced inhibition of proliferation and caspase mediated apoptotic pathway promotion of both cell types, pre-osteoblasts and osteoblasts, while impaired the osteoblast differentiation decreasing ALP activity. The effect of ROS rise is probably due to the up regulation of GSK3β expression, a critical downstream substrate and effector of PI3K/AKT, resulting in proliferation and differentiation decrease [170,172,173]. Moreover, the Dexa-inhibitory effect on osteogenesis was also supported by the osteoblast diminution of the osteogenesis-related proteins, including the early marker ALP and the late differentiation marker OCN, fundamental for bone matrix formation [172,174,175]. Bone-ALP is a membrane protein of osteoblast, released into the serum once activated. It contributes to skeleton calcification enhancing the local concentration of inorganic phosphate or working as a calcium-binding protein Ca^{2+}-ATPase [176]. On the other hand, OCN is the most abundant non-collagenous protein in bone, which regulates bone quality, fundamental for bone strength and for regulating the growth of the long bone. Clinically, serum OCN is a marker for bone formation.

Additionally, Dexa caused negative effects on bone metabolism balance working on two key cytokines expressed in osteoblast: RANKL and OPG. As anticipated, RANKL binding to its receptor RANK on osteoclast surface stimulates bone resorption, while the OPG binding to RANKL inhibits its erosive activity. Dexa was found able to up-regulate RANKL and downregulate OPG expression, in both *in vitro* and *in vivo* models. Furthermore, among the regulators of osteoblast differentiation and bone formation, there are the bone morphogenic proteins (BMPs), members of transforming growth factor beta (TGFβ) superfamily. Interestingly, Dexa-treated rats and primary osteoblasts showed a significant down-regulation of BMP-2 and its receptor (BMPR), together with the BMP-target gene RUNX2, a transcriptional regulator of osteoblast differentiation [177]. Finally, a study carried out by Zhang S. et al. (S. Zhang et al., 2018b) on human fetal osteoblast cell line (hFOB) correlated the dose of Dexa with the induction of autophagy *via* intracellular ROS. Indeed, low and short doses of Dexa induced an increase in ROS and parallel up-regulation of autophagy-associated proteins (beclin-1 and LC3β). To respond to oxidative stress, autophagy was successfully activated to protect osteoblasts from cell death; however, if the oxidative stimuli persist, the antioxidant capacity of autophagy will be overwhelmed, and the protective response fails, potentially leading to osteoblast apoptosis [171].

4.1.3 Application of MSCs and their secretome in bone aging

Impaired capability of osteogenic differentiation, dysregulated bone resorption/deposition balance, senescence of resident stem cells, altered microenvironment, and disordered immunoregulation play a central role in osteoporosis pathogenesis [178]. MSC-based therapies promise to increase osteoblast differentiation and inhibit osteoclast activation, rebalance the bone resorption/deposition axis, and enhance bone regeneration [179]. Different approaches have been tested including the direct transplantation of mesenchymal cells or genetically modified ones, as well as the application of the derived paracrine [178,180,181].

Preclinical investigations showed that MSC transplantation in osteoporotic *in vivo* models enhances osteoblast differentiation while inhibiting osteoclast activation and rebalancing the bone formation/resorption axis. Different studies, highlighted that the direct transplantation of human placenta-derived mesenchymal stem cells (PDSCs) and umbilical cord blood mesenchymal stem cells (UCMSECs) in ovariectomized rats or mice (OP model) increased the accumulation of collagen, the rod-like shaped trabecular bone, and the formation rate, improved the trabecular micro-architecture, while reduced the damage to the structure of bone trabeculae [182,183].

Meanwhile, gene modification, targeted modification, and co-transplantation of MSCs are the latest techniques developed and promise to enhance MSC therapeutic effect and efficacy. To obtain improved osteogenic and angiogenic MSC capabilities, gene modifications have been performed, in example overexpressing osteogenic-related genes, silencing genes for bone resorption to inhibit osteoclast activation, overexpressing angiogenic genes, modifying homing-related genes to enhance MSC homing and migration, or reducing MSC senescence [178]. Moreover, to improve the bone-targeted efficacy of MSCs and their retention, targeted surface proteins could be added on MSC membranes. This approach can also be combined with gene modification.

The application of MSC-EV in *in vitro* and *in vivo* models of bone diseases showed similar effect to direct transplantation, but with the advantage of being a cell-free therapy. Indeed, it has been seen that MSC-EVs are able to promote angiogenesis and osteoblast proliferation, as well as to inhibit osteoclast activity, inflammation and oxidative stress, probably thanks to their endogenous cargo [151,152,184]. Indeed, MSC-EVs can regulate key pathways for bone formation and resorption, including Wnt/β-catenin, PI3K/Akt, NF-κB, and RANKL. Furthermore, MSC-EVs effectively promoted angiogenesis *via* IncRNAH19-Angpt1-Tie2/NO signaling and inhibited the expression of pro-inflammatory cytokines, including TNFα, IL18, and IL1β, as well as the induction of inflammasome activation, which in turn leads to the inhibition of bone resorption [180].

Among the different MSC sources, BMSCs are the most commonly used in tissue engineering. Serval evidence suggested the BMSC-derived EV (BMSC-EVs) potential in promoting osteogenesis, angiogenesis, and bone mineralization in several bone defect models. Human umbilical cord mesenchymal stem cells (hUCMSCs) have also attracted much interest in bone defects. hUCMSC-EVs can stimulate osteogenic and chondrogenic differentiation, as well as angiogenesis, that indirectly promote bone regeneration. Compared to the previous, they display major pluripotency and pro-angiogenesis potential. Moreover, similarly to hAFSCs, hUCMSCs are obtained from perinatal waste tissue and, due to their derivation, they are free from ethical and moral controversies [31].

Since osteoporosis and bone aging are systemic conditions, a systemic administration, rather than local one, can improve their efficacy in counteracting bone loss. Different studies showed a limited therapeutic efficiency of MSC-EVs administered systemically, while it significantly increases in modified bone-targeted MSC-EVs [180].

Even if still many issues need to be addressed, such as EV standardization, modification, and administration to improve their beneficial potential, MSC-EVs show promising therapeutic effects in the treatment of osteoporosis.

4.2 Materials and Methods

4.2.1 HOB culture and treatments

Human pre-osteoblast cells (HOB) were grown in culture medium composed by αMEM medium (Corning, MA, USA) supplemented with 10% FBS (Gibco, Waltham, MA, USA), 2 mM L-glutamine, 100 U/mL penicillin, and 100 µg/mL streptomycin (all from EuroClone Spa, Milano, Italy), in a humidified atmosphere, 5% CO_2 at 37°C. Osteogenic differentiation was obtained replacing culture medium with differentiation medium (for 5 days) composed by αMEM medium (Corning, MA, USA) supplemented with 1% FBS (Gibco, Waltham, MA, USA), 2 mM L-glutamine, 100 U/mL penicillin, and 100 µg/mL streptomycin (all from EuroClone Spa, Milan, Italy), 100 µM 2P-ascorbic acid, and 5 mM β-glycerophosphate (all from Sigma-Aldrich, Milan, Italy). The day after the induction of differentiation, EVs were added for 4 days (40 µg/ml) while Dexamethasone (Sigma-Aldrich, Milan, Italy) treatment was added at the end of differentiation for 24 h at the concentrations of 0.5, 5, 20, and 50 µM. The study of AFSC-EVs effect on HOB differentiation was performed by maintaining cells in culture medium supplemented by 1,3 x 10^8 particles/cm^2 for 4 days.

4.2.2 MTT assay

HOB cells were seeded in a 96-well plate in 100 µL of culture medium at the density of 500 cells/well, 4 replicates for each condition. The following day, differentiation was started and after 24 hours AFSC-EVs were added (for 4 days). Dexamethasone treatments were performed after 5 days of differentiation induction at the concentration of 0.5, 5, 20, and 50 µM. At the end of the experiment, cells were incubated with 0.5 mg/mL MTT (Sigma-Aldrich, Milan, Italy) for 4 hours at 37°C and 5% CO_2. Then, the medium was removed, and the resulting formazan salts were solubilized by acidified isopropanol (isopropanol, 0.1 M HCl) (Carlo Erba, Milan, Italy) prior quantification. The absorbance was measured at 570 nm using a microplate spectrophotometer (Appliskan, Thermo-Fisher Scientific, Vantaa, Finland).

4.2.3 ROS and glutathione detection

To analyze intracellular reactive oxygen species (ROS), dichlorodihydrofluorescein diacetate (DCFH-DA) (Sigma-Aldrich, Milan, Italy) assay was applied. HOB cells were seeded in a 96-well black plate in 100 µL of culture medium at the density of 500 cells/well, 4 replicates for each condition. After cell treatments (as previously described), culture medium was replaced with PBS/glucose (1 g/L) containing 5 µM DCFH-DA and incubated at 37°C, 5% CO_2 for 30 minutes. Then, cells were washed with PBS, and oxidized dichlorofluorescein (DCF) product fluorescence was read at 485 nm (excitation) and 535 nm (emission) using multiwell reader Appliskan (Thermo-Fisher Scientific, Vantaa, Finland). The values of well not incubated with the probe were subtracted as cellular autofluorescence background.

Similarly, monochlorobimane (MCB) (Sigma-Aldrich, Milan, Italy) assay was performed to evaluate glutathione (GSH) levels. Cell culture medium was replaced with 50 µM MCB in PBS/glucose and cells were incubated for 30 minutes (37°C, 5% CO_2). Wells were washed once with PBS, and their fluorescence was measured at 355 nm (excitation) and 460 nm (emission).

4.2.4 Cellular extracts preparation

Total cellular pellets were processed and quantified as previously described in *Section 3.2.8*. HOB nuclei were purified adding to 5×10^6 cells 400 µL of nuclear isolation buffer (10 mM Tris-HCl, pH 7.8, 1% Nonidet P-40, 0.5 mM phenylmethylsulfonyl fluoride, 10 mM β-mercaptoethanol, and 1 µg/mL aprotin and leupeptin) for 8 minutes on ice. 400 µL of MilliQ water were added to swell cells for 3 minutes. Passage through a 22-gauge needle was performed to shear cells and then, nuclei were recovered by centrifugation at 400 × g at 4°C for 6 minutes and wash in 400 µL of washing buffer (10 mM Tris-HCl, pH 7.4, and 2 mM $MgCl_2$, plus inhibitors described above in this section). Supernatants (containing cytosolic fractions) were further centrifuged at 4000 × g for 30 minutes. Isolated cytoplasmic and nuclear extracts were finally lysed in a lysis buffer, sonicated, cleared by centrifugation and processed as described above for total lysates.

4.2.5 SDS-PAGE and protein digestion

Total, nuclear and cytoplasmatic lysates were separated by 4-16% SDS-PAGE and then, gels were stained in the Coomassie brilliant blue G solution (0.1% Coomassie blue in 10% acetic acid, 45% methanol) (Sigma-Aldrich, MO, USA) and shaken at room temperature for 1 hour. The gels were destained by soaking for 2 hours in a destaining solution (10% acetic acid, 30% methanol). In gel trypsin digestion was performed as described by Shevchenko et al. [185]. Briefly, stained gel bands were cut in small pieces and treated with solution A (1:1 mixture of acetonitrile and 100 mM ammonium bicarbonate) for 30 minutes and then dried under vacuum. Proteins were subjected to reduction of disulfide bonds by 10 mM DTT at 56°C for 1 h. Alkylation of cysteine residues was performed with 55 mM iodoacetamide for 45 minutes at room temperature in the dark (all from Sigma-Aldrich, MO, USA). Ammonium bicarbonate and solution A were used to perform rehydration and dehydration and after that, samples were finally dried under vacuum. Trypsin digestion was performed by incubating the dry gel slice with 40 µL of sequencing grade modified trypsin (12.5 ng/µL in 50 mM NH_4HCO_3) (all from Sigma-Aldrich, MO, USA) overnight at 37°C. Following digestion step, the tryptic digested proteins were extracted from the gels with 100 µL of acetonitrile/0.1% formic acid and samples were dried under vacuum and stored at -20°C until LC-MS/MS analysis was performed.

4.2.6 Mass Spectrometry and data analysis

Samples were dissolved in 40 µL of water:acetonitrile:formic acid (95:3:2), sonicated, centrifuged, and 35 µL of this solution was injected into a UHPLC system coupled to a Q Executive mass spectrometer equipped with a HESI-II ion source. Peptides were loaded into a C18 Hypersil Gold (100 × 2.1 mm ID, 1.9 µm ps) column (all from Thermo Fisher Scientific, MA, USA) and separated by linear gradient of 0.1% formic acid in water (A) and acetonitrile (B) from 2% B to 28% B in 90 minutes. The mass spectrometer was operated with a Data Dependent Acquisition (DDA) method, performing a 250 $<m/z<$2000 Full MS scan at 70000 resolution (at m/z 200) followed by HCD fragmentation at 28 normalized collision energy of the Top 8 most intense precursor ions (charge state $z \geq 2$, 17, 500 resolution (at m/z 200)), with a dynamic exclusion of 8 seconds. Raw data files were converted to mascot generic format (.mgf) using MSConvert and protein identification was performed using Mascot Server (Version 2.7.0) search engine against the Human section of the neXtProt database (54 paper osteo) and against a database of contaminants commonly found in proteomics experiments (cRAP). The search parameters were set as follows: Trypsin was selected as enzyme with one missed cleavage allowed; carbamidomethylation (C) was specified as fixed modification while oxidation (M) and deamidated (NQ) as variable modifications; peptide and MS/MS tolerances were 10 ppm and 0.02 Da, respectively. False discovery rate (FDR) evaluation was performed using DECOY search tool and results were filtered at 1% FDR for peptide-spectrum matches (PSMs) above homology. Only proteins identified with at least 2 independent peptides were considered as a significant hit. The parameter "Intensity" calculated by the software and normalized based on the total amount of emPAI (exponentially modified Protein Abundance Index) (55 paper osteo) was used to estimate the abundance of the proteins across the different samples. The protein ratio between the HOB+EVs and HOB samples was then calculated. Only ratio values ≥ 2.0 or ≤ 0.5 were considered. For the Galectin-3, whose ratio was not ≥ 2.0 or ≤ 0.5, the two highest scoring peptides ion peak areas were used to evaluate protein fold-change between HOB+EVs and HOB samples (56 paper osteo), to have a better quantification.

4.2.7 SDS-PAGE and Western Blot

HOB total, nuclear, and cytoplasmic lysates were processed as previously described (*Section 3.2.9*). Primary antibodies used are against the following molecules: Actin (Sigma-Aldrich, St Louis, MO, USA), total-Akt, OCN, OPN, OSX, SOD1, SIRT1, TrxR1, HOx1, MAP LC3β, PARP, FKHRL1 FOXO3a, Lamin A/C (Santa Cruz Biotechnology, CA, USA), p70, p-p70, caspase7, Bcl-2 (Bio Source, CA, USA), Galectin-3, p21, pAkt ^{Ser473} (Cell Signaling Technology, Lieden, Netherlands), Nrf2 (Abcam, Cambridge, UK). Secondary antibodies, all used at 1:3000 dilution, were all from Thermo Fisher Scientific (MA, USA).

4.2.8 Immunofluorescence and confocal microscopy

For immunofluorescence analyses, 5000 cells/cm^2 were seeded in glass coverslip placed inside a multi-12 well (culture medium volume: 500 µL). After treatments, cells were fixed with 4% paraformaldehyde (PFA) (Sigma-Aldrich, Milan, Italy). For only intracellular markers, fixed cells were permeabilized with 0.1% Triton X-100 for 4 minutes (Sigma-Aldrich, Milan, Italy). After washing twice with PBS, unspecific binding sites were blocked with 3% BSA/PBS (Sigma-Aldrich, Milan, Italy) for 30 min at RT. After blocking, cells were incubated with primary antibodies diluted in 3% BSA/PBS in a wet chamber overnight at 4°C. The day after, 3 washing with 3% BSA/PBS were performed before secondary antibodies incubation (1 hour, at room temperature in the dark). Then, cells were washed again, twice with PBS and once with distilled water, and nuclei were stained with 4',6-diamidino-2-phenylindole (DAPI) for 5 minutes. After 2 PBS washing, coverslips were mounted on slides with anti-fading medium (0.21 M DABCO, 90% glycerol in 0.1 M Tris pH 8.0). Primary antibodies used are against the following molecules: osterix, OCN, 53BP1 (Santa Cruz Biotechnology, CA, USA), p21 (Cell Signaling Technology, Lieden, Netherlands), and pH2A (Millipore, CA, USA). Alexa secondary antibodies (Thermo Fisher Scientific, MA, USA) were used at 1:200 dilution. Image acquisition was performed with a Nikon A1 confocal laser scanning microscope. 3D projections were obtained from confocal serial sections by ImageJ software, while image rendering was performed by Adobe Photoshop software.

For apoptosis detection, after 3 washes with 50 µL of binding buffer (10 mM HEPES, pH 7.5, containing 140 mM NaCl and 2.5 mM $CaCl_2$), samples were incubated for 15 minutes with 50 µL of double staining solution composed by binding buffer containing 0.25 µL of annexin V-FITCH and 0.25 µL of propidium iodide (PI) (BD Pharmingen TM, Erembodegem, Belgium). Finally, samples were washed 5 times with 50 µL of binding buffer, mounted with 15 µL of binding buffer, and visualized under confocal microscopy.

4.2.9 Alizarin Red S staining

4% paraformaldehyde fixed monolayer cells were washed with distilled water and then incubated with 2% Alizarin Red S solution (Sigma-Aldrich, MO, USA) at pH 4.2 for 30 minutes at room temperature. Histological sample images were obtained with a Zeiss Axiophot microscope (Zeiss AG, Jena, Germany), equipped with a Nikon DS-5Mc CCD color camera.

4.2.10 ALP assay

After collection, conditioned mediums (CM) derived from multi-12 wells (500 µL from each well) were centrifuged at 300 x *g* for 10 minutes at RT to remove cellular debris. Cell lysates were washed twice with cold PBS and then, cells were resuspended in 100 μL of Assay Buffer. Samples were homogenized on ice and then insoluble materials were removed by centrifugation at 10 000 x *g* for 15 minutes at 4°C. Quantification by Bradford method was performed, lysates and CM were added in a black 96-well plate (4 replicates for each condition), and Alkaline Phosphatase assay was performed according to the manufacturer's protocol of ALP assay kit (colorimetric) (Abcam, Cambridge, UK).

4.2.11 Statistical analysis

Experiments were performed in triplicate. For quantitative comparison, values were reported as mean ± SD based on triplicate analysis for each sample. One-way ANOVA with Bonferroni post hoc test was applied to evaluate the observed difference in significance among the study groups. A p value < 0.05 was considered statistically significant. GraphPad Prism® release 6.0 software was used to obtain statistical analysis and plot layout.

4.3 Results

4.3.1 AFSC-EV effect on cell death

MTT assay showed that the treatment with increasing Dexamethasone concentrations (from 0,5 µM to 50 µM) causes significant decrease in HOB viability from the concentration of 20 µM, that became more than 50% at the concentration of 50 µM (***Figure II.1A***). Based on that, we decided to perform all the following experiments with the Dexa concentration of 20 µM.

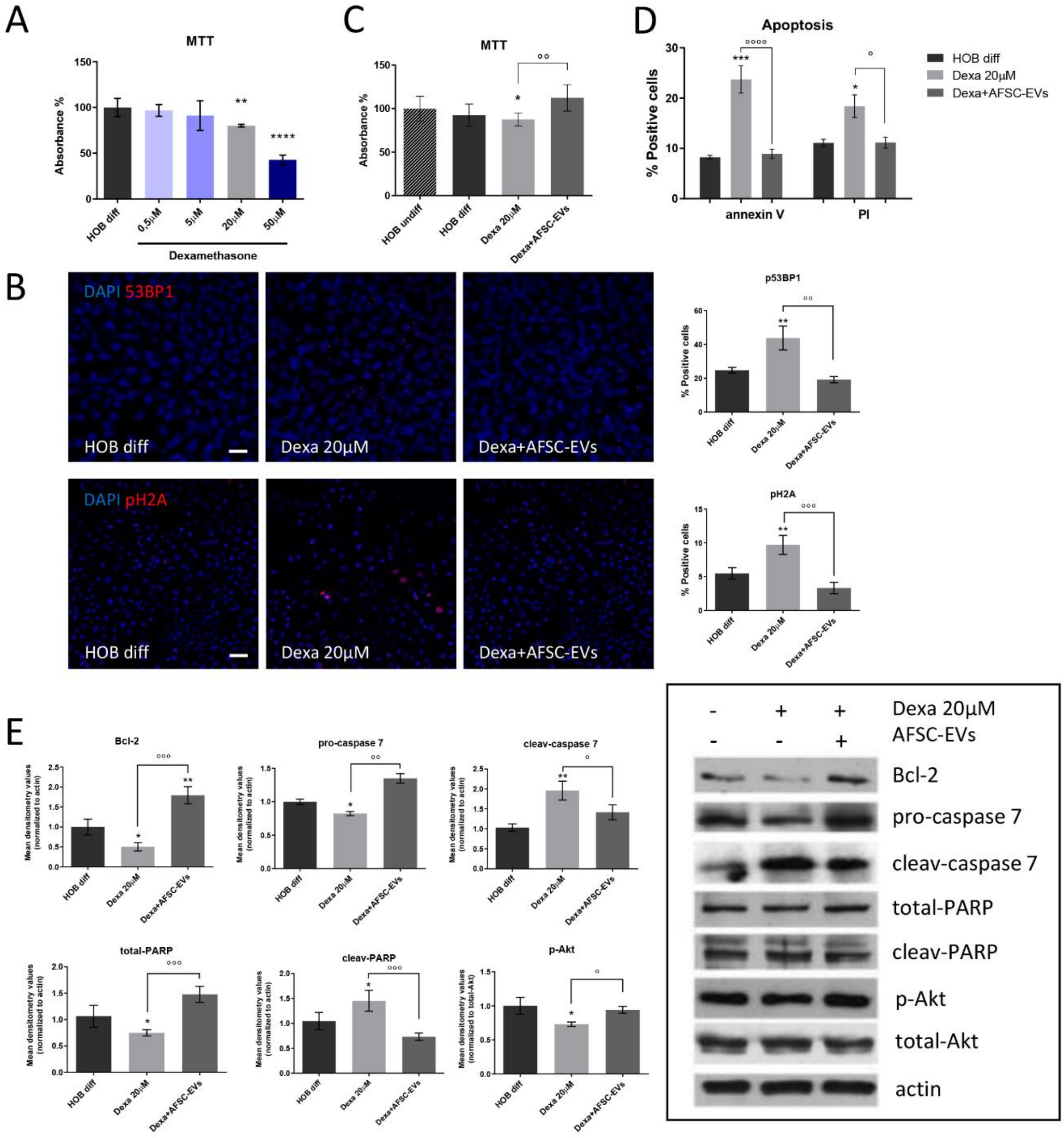

Figure II.1. Amniotic fluid stem cell-derived extracellular vesicle effects on viability and apoptotic pathway alterations caused by Dexamethasone treatment.

(A) Graph showing MTT assay of differentiated human osteoblast (HOB) treated with 0.5, 5, 20, and 50 µM of Dexamethasone. Data shown are the mean ± SD (n=4). $^{**}p$ value < 0.01, $^{****}p$ value < 0.0001.

(B) Representative images of differentiated HOB cells, treated or not with Dexamethasone and AFSC-EVs, stained with p53BP1 (red) – top – and pH2A (red) – bottom. Nuclei stained with DAPI. Scale bars: 25 µm. To the right, a graph showing the percentage of positive cells. Data shown are the mean ± SD of 5 fields visualized for each condition. $^{**,\circ\circ}p$ value < 0.01, $^{\circ\circ\circ}p$ value < 0.001.

(C) Graph showing MTT assay of HOB cells treated with 20 µM Dexamethasone in presence or absence of AFSC-EVs. Data shown are the mean ± SD (n=4). $^{*}p$ value < 0.05, $^{\circ\circ}p$ value < 0.01.

(D) Graph showing the percentage of annexin V and PI positive cells after AFSC-EVs and/or Dexa treatments. Data shown are the mean ± SD (n=3). $^{*,\circ}p$ value < 0.05, $^{***}p$ value < 0.001, $^{\circ\circ\circ\circ}p$ value < 0.0001.

(E) Representative images of WB analysis of HOB total lysates treated or not with Dexa in presence or absence of AFSC-EVs, revealing Bcl-2, pro- and cleav-caspase7, total- and cleav-PARP, phosphorylated $\text{Akt}^{\text{Ser473}}$, and total-Akt protein levels. The graphs represent the mean ± SD of densitometric analysis (n=3) normalized to actin values. $^{*,\circ}p$ value < 0.05, $^{**,\circ\circ}p$ value < 0.01, $^{\circ\circ\circ}p$ value < 0.001.

Since the exposure to Dexa 20 µM showed a viability decrease, we investigated the DNA damage, analyzing the binding protein of p53 (p53BP1), known as a DNA damage response (DDR), and the phosphorylation of the histone variant H2A.X, DDR pathway initiator. Interestingly, the DNA damage leads to the induction of p53 signal, however the final response to p53 activation can range from the induction of different irreversible consequences, such as cell death or senescence, to a reversible cell cycle arrest [186]. In our model, Dexa treatment increased 53BP1 and pH2A labeling, while AFSC-EV pre-exposure reduced this negative rise, as shown by immunofluorescence analysis (***Figure II.1B***).

Moreover, the apoptotic pathway involvement in Dexa-mediated viability decrease was investigated by annexin V and propidium iodide (PI) analysis. Interestingly, AFSC-EV pre-treatment significantly restored the cell viability affected by Dexa (***Figure II.1C***) and reduced the augmented annexin V and PI staining (***Figure II.1D***). Similarly, western blot analysis showed an increase in the anti-apoptotic marker Bcl-2 in EV treated cells, and, at the same time a reduction in the cleavages of PARP and caspase7 increased by Dexa. In parallel, AFSC-EVs stimulated the activation of the key survival signaling molecule Akt, as shown by its higher phosphorylation on Ser 473, normalized to total-Akt.

These results suggest that AFSC-EVs can reduce the decrease in cell viability linked to the activation of apoptotic pathways.

4.3.2 AFSC-EV role in autophagic pathway

Recent evidence highlighted the central role of autophagy in bone homeostasis maintenance, and how alterations in this repairing pathway can be associated with osteoporosis [157].

Interestingly, we observed that AFSC-EVs positively modulated the autophagic pathway probably increasing the levels of the autophagy promoter SIRT1 (***Figure II.2A***). Then, we investigated the phosphorylation of p70 and LC3β level, both autophagy markers even if in opposite manner. According to WB analysis, the active form of LC3β, LC3β-II, was increased by Dexa treatment (***Figure II.2A***), while immunofluorescence staining revealed its nuclear localization (***Figure II.2B***). Interestingly, AFSC-EV pre-exposure counteracted the phosphorylation of p70 (***Figure II.2A***), as well as increased the cytoplasmic localization of LC3β (***Figure II.2B***), translocation induced by the SIRT1-mediated deacetylation [187].

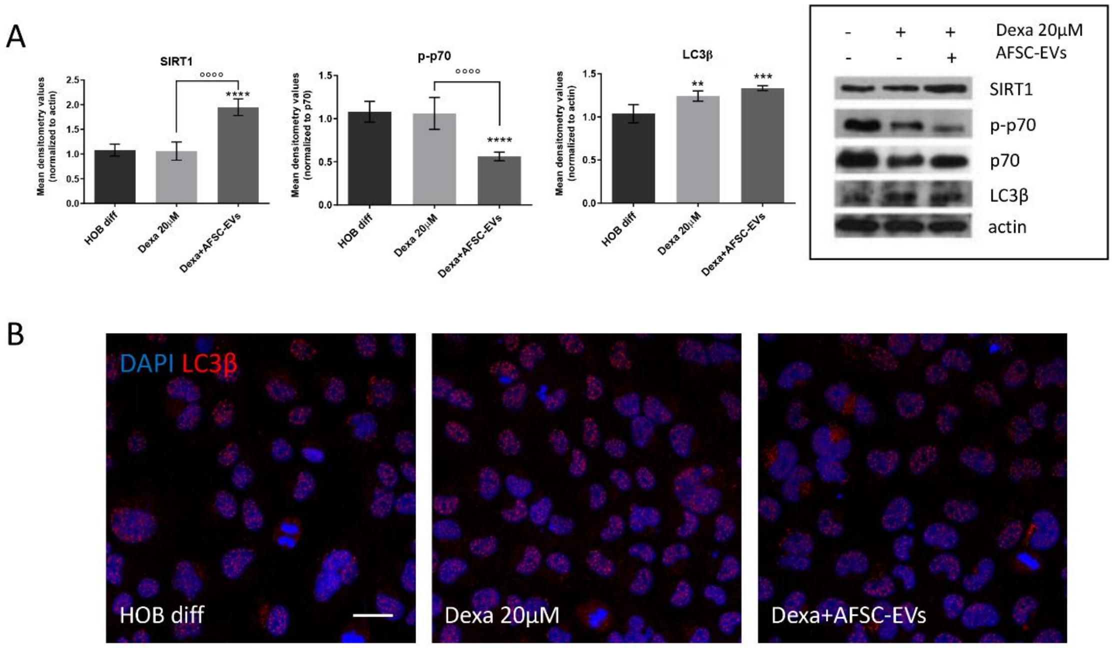

Figure II.2. AFSC-EVs effect on autophagic pathway during Dexamethasone osteoporosis induction of HOB cells.

(A) Representative images of WB analysis of HOB total lysates treated or not with Dexa in presence or absence of AFSC-EVs, revealing SIRT1, phosphorylated and not p70, and LC3β-II protein levels. The graphs represent the mean ± SD of densitometric analysis (n=3) normalized to actin values. ***p* value < 0.01, ****p* value < 0.001, $^{****,\circ\circ\circ\circ}$ value < 0.0001.

(B) Representative images of differentiated HOB cells, treated or not with Dexamethasone and AFSC-EVs, stained with LC3β (red). Nuclei stained with DAPI. Scale bar: 10 μm.

4.3.3 Modulation of Reactive Oxygen Species (ROS) by AFSC-EVs

As expected, Dexa treatment induced a dose-dependent increase of ROS in differentiated HOB, as shown by ***Figure II.3A***. In particular, ROS levels significantly increased from the treatment concentration of 20 µM. Moreover, the ROS rise caused by this concentration was reduced by EVs exposure, with a parallel increase in reduced glutathione (GSH) levels (***Figure II.3B***).

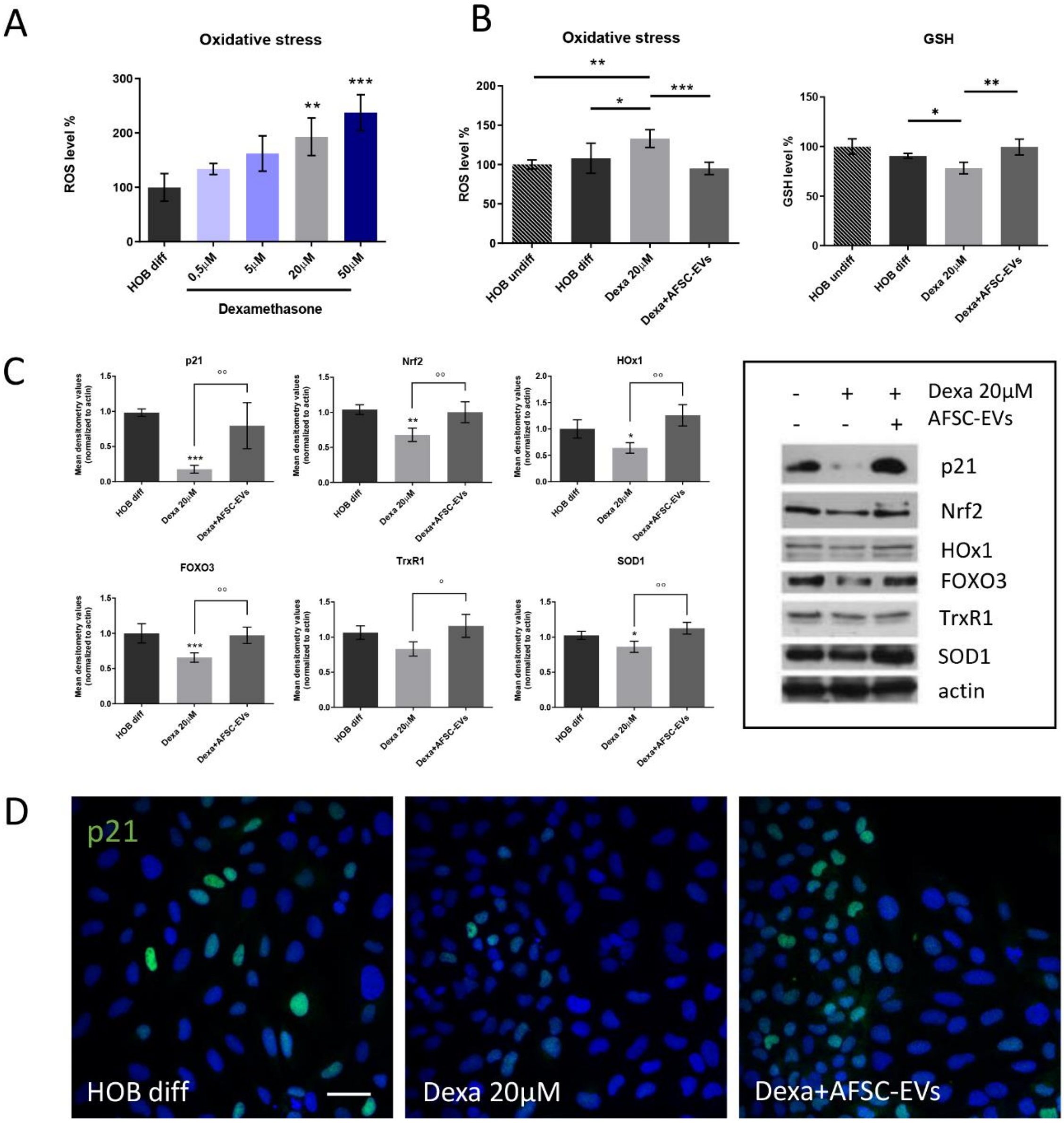

Figure II.3. Effect of AFSC-EVs on oxidative stress unbalance during Dexamethasone-induced osteoporosis.

(A) Graph showing ROS assay of differentiated human osteoblast (HOB) treated with 0.5, 5, 20, and 50 µM of Dexamethasone. Data shown are the mean ± SD (n=4). **p value < 0.01, ***p value < 0.001.
(B) Graph showing ROS – left – and GSH – right – content into undifferentiated HOB cells and differentiated ones treated with 20 µM Dexamethasone in presence or absence of AFSC-EVs. Data shown are the mean ± SD (n=4). *p value < 0.05, **p value < 0.01, ***p value < 0.001.
(C) Representative images of WB analysis of HOB total lysates treated or not with Dexa in presence or absence of AFSC-EVs, revealing p21, Nrf2, HOx1, FOXO3, TrxR1, and SOD1 protein levels. The graphs represent the mean ± SD of densitometric analysis (n=3) normalized to actin values. $^{*,\circ}p$ value < 0.05, $^{**,\circ\circ}p$ value < 0.01, ***p value < 0.001.
(D) Representative images of differentiated HOB cells, treated or not with Dexamethasone and AFSC-EVs, stained with p21 (green). Nuclei stained with DAPI. Scale bar: 10 µm.

Then, we explored the alterations of antioxidant protein expression during osteoporosis induction, in presence or absence of AFSC-EVs. p21 can control oxidative stress unbalance by the positive regulation of Nrf2 transcriptional activity [188]. Indeed, Dexa reduced p21 levels, restored by EV exposure as shown by western blot (***Figure II.3C***) and immunofluorescence (***Figure II.3D***) analyses. Similar trend was observed for the redox sensitive transcriptional factors Nrf2 and FOXO3, which regulate the expression of several antioxidant enzymes, such as SOD1, HOx1, and TrxR1 that appeared significantly increased in AFSC-EVs pre-treated condition compared to the Dexa treated one (***Figure II.3C***).

4.3.4 Effect of AFSC-EVs on osteogenic differentiation affected by Dexamethasone

Even if at the end of the differentiation protocol, Dexa-treated HOB cells showed impaired osteogenic marker expression, namely osterix (OSX), osteocalcin (OCN), and osteopontin (OPN), as shown in ***Figures II.4A*** and ***II.4B***.

Accordingly, the analysis of intracellular and secreted alkaline phosphatase (ALP), together with the evaluation of calcium deposits performed by Alizarin Red staining, confirmed a reduction in bone matrix deposition after Dexa treatment (***Figure II.4C*** and ***II.4D***). Conversely, pre-exposure to AFSC-EVs counteracted these negative effects, significantly restoring the levels of all these markers.

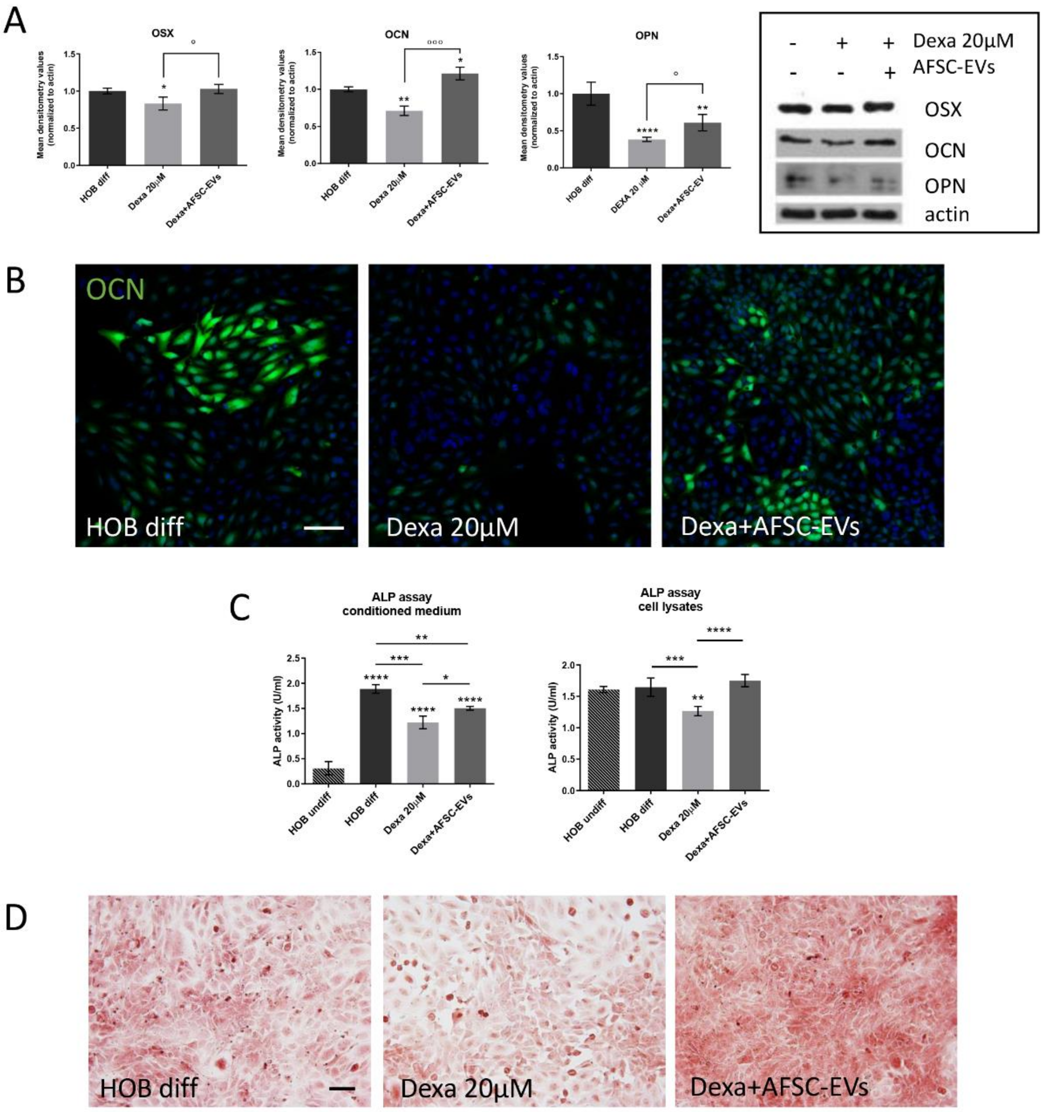

Figure II.4. AFSC-EV effect osteogenic differentiation during Dexamethasone-induced osteoporosis.

(A) Representative images of WB analysis of HOB total lysates treated or not with Dexa in presence or absence of AFSC-EVs, revealing OSX, OCN, and OPN protein levels. The graphs represent the mean ± SD of densitometric analysis (n=3) normalized to actin values. *,°*p* value < 0.05, ***p* value < 0.01, °°°*p* value < 0.001, *****p* value < 0.0001.

(B) Representative confocal images of differentiated HOB cells, treated or not with Dexamethasone and AFSC-EVs, stained with OCN (green). Nuclei stained with DAPI. Scale bar: 30 µm.

(C) Graph showing ALP assay of total cell lysates and conditioned medium from undifferentiated HOB cells and differentiated HOB cells treated or not with Dexamethasone, in presence or absence of AFSC-EVs. The graphs represent the mean ± SD (n=4 of 3 biological samples).

(D) Representative images of Alizarin Red staining of differentiated HOB cells, treated or not with Dexamethasone and AFSC-EVs. Scale bar: 50 µm.

4.3.5 Effect of AFSC-EVs on undifferentiated pre-osteoblast cells

The interesting results regarding the positive consequences of AFSC-EVs treatment on differentiated HOB cells led us to explore in deep its effect on undifferentiated pre-osteoblasts. Interestingly, the exposure to AFSC-EVs alone for 4 days promoted the differentiation process towards the osteoblast feature.

Indeed, the levels of transcription factor osterix and the secreted protein osteocalcin, both osteoblast markers, increased after EVs treatment, as shown by immunofluorescence images (***Figure II.5A***). Furthermore, Alizarin Red staining demonstrated the increase in calcified extracellular matrix deposition, confirming the pro-differentiative effect of AFSC-EVs.

To explore the mechanisms underpinned to the pro-osteogenic induction of AFSC-EVs, nuclear cell extracts of HOB were obtained for proteomic experiments. Mass spectrometry (MS) analysis showed an increase in osteogenic differentiation related protein, and a decrease in inhibiting proteins of bone differentiation, after 4 days of AFSC-EV exposure (Table in ***Figure II.5C***). Among the different nuclear proteins identified by MS, particular attention was focused on proteins involved in osteogenic differentiation, as reported in literature [189,190]. Previously, my research group found in AFSC-EV proteome the presence of Galectin-3 binding protein [41], and this observation led us to investigate the levels of the osteoblastogenesis promoting protein Galectin-3 in HOB cells after AFSC-EV exposure [191]. Interestingly, Galectin-3 protein appeared dramatically increased in EV-treated HOB nuclei, as shown by IF and WB analysis and also suggested by proteomic analysis (***Figures II.5C*** and ***II.5D***).

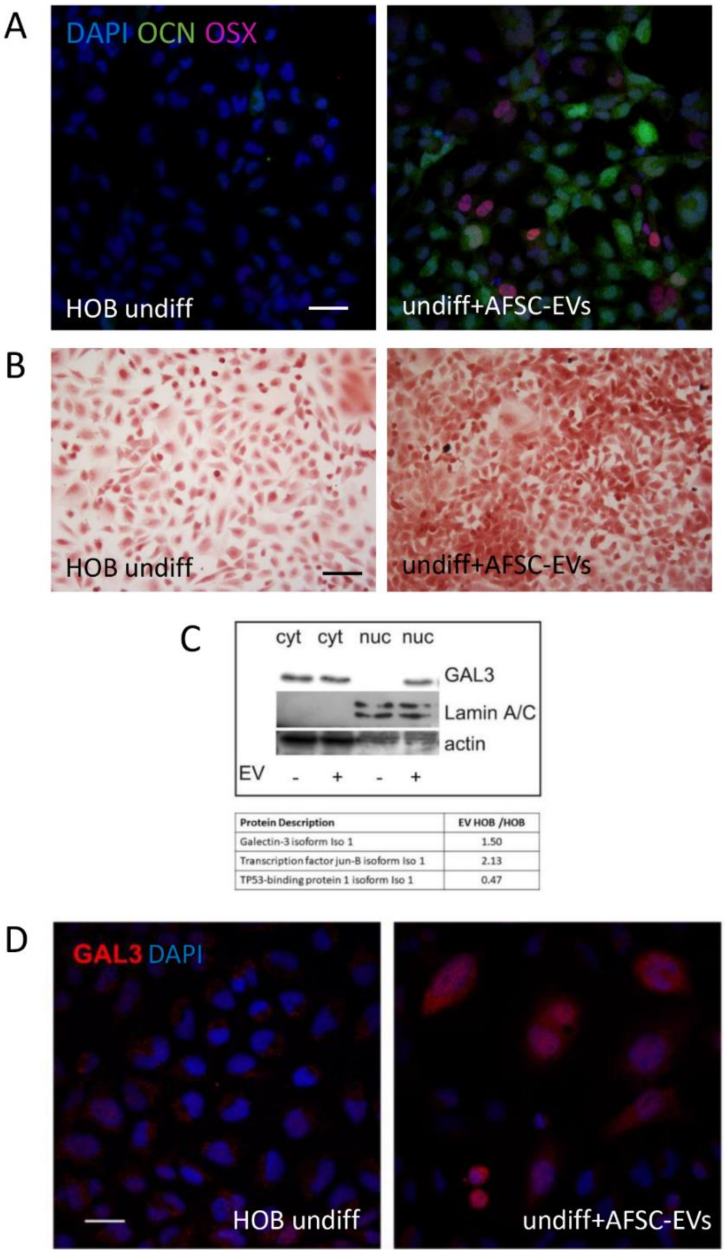

Protein Description	EV HOB /HOB
Galectin-3 isoform Iso 1	1.50
Transcription factor jun-B isoform Iso 1	2.13
TP53-binding protein 1 isoform Iso 1	0.47

Figure II.5. Pro-osteogenic effect of AFSC-EVs on undifferentiated HOB cells.

(A) Representative confocal images of undifferentiated HOB cells, treated or not with AFSC-EVs, stained with OCN (green), and OSX (red). Nuclei stained with DAPI. Scale bar: 30 µm.

(B) Representative images of Alizarin Red staining of undifferentiated HOB cells, treated or not with AFSC-EVs. Scale bar: 50 µm.

(C) Top – representative images of WB analysis of undifferentiated HOB cytoplasmatic (cyt) and nuclear (nuc) lysates treated or not with AFSC-EVs, revealing Galectin-3 (GAL3), Lamin A/C (as nuclear marker), and actin (as a loading control) protein levels. Bottom – table showing MS semi-quantitative results of nuclear proteins identified in undifferentiated HOB treated or not with EV. The ratio between EV-treated HOB and untreated is shown for the proteins identified in both samples and involved in osteogenic differentiation process.

(D) Representative images of undifferentiated HOB cells, treated or not with AFSC-EVs, stained with GAL3 (red). Nuclei stained with DAPI. Scale bar: 10 µm.

4.4 Discussion

As in most age-related pathologies, oxidative stress plays a central role also in the osteoporosis process, affecting bone homeostasis and remodeling *via* apoptosis induction and autophagy balance interference [169]. Glucocorticoids, as the synthetic one Dexamethasone (Dexa), can produce dose-dependent negative effects on bone redox homeostasis by generating an increase in intracellular reactive oxygen species (ROS), and consequent defects in cell differentiation and autophagic processes, that finally leads to cell death [169–171]. In this osteoporosis *in vitro* model, Dexa treatment generated a ROS rise, accompanied by a reduction in antioxidant defenses, and collateral increase in DNA damage and apoptosis. Based on previous studies, even by our lab, that demonstrated the antioxidant cargo of gestational stem cell-derived extracellular vesicles, EVs from AFSCs were applied [42,192]. This study demonstrated a positive AFSC-EV influence on viability, autophagy efficiency, and differentiation that can be linked to the extracellular vesicle role in ROS balance modulation. Since the highly complex EV cargo, a multifactorial effect cannot be excluded and, for this reason, particular attention was paid to possible parallel mechanisms to avoid osteoporosis, such as the activation of osteogenic differentiation.

Recent studies demonstrated that SIRT1 is an important player in skeletal bone maintenance, indeed its deletion in adult mice has been linked to bone mass reduction, demonstrating that SIRT1 is not only important during development and growth [60]. Moreover, it has been reposted that SIRT1 is a potent intracellular inhibitor of inflammatory response, oxidative stress, but also inducer of autophagic process. Considering the AFSC-EV potential in the redox modulation, interestingly, we observed a huge increase in SIRT1 levels in AFSC-EV treated condition. As already discussed, SIRT-mediated deacetylation of FOXO factors, as FOXO1, FOXO3a or FOXO4, induced an overexpression of antioxidant genes, such as catalase, SOD, Trx, and SIRT1 as well, boosting an auto-feedback loop. Consistently, after AFSC-EV exposure, we observed an increase in FOXO3 levels, as well as in antioxidant SOD1, and TrxR1, previously affected by Dexa. Moreover, the level of phosphorylated p70 S6 kinase (p-p70 S6 kinase), protein substrate of mTOR pathway, and the ratio p-p70 S6 kinase/p70 S6 kinase were significantly reduced by AFSC-EVs exposure, suggesting their positive effect on autophagy [193]. In parallel, we observed that, even if increased in Dexa treated condition, LC3β protein showed a translocated puncta labeling, autophagosome like, into the cytoplasm only in EV-exposed cells. Notably, only SIRT1-deacetylated LC3β can return into the cytoplasm, thanks to the binding of nuclear protein DOR, and in this site, it is able to bind autophagy mediators [187]. Together, these results suggest the pro-autophagic activity of AFSC-EVs in Dexa-exposed HOB cells, probably by the redox-dependent regulation of SIRT1. In parallel to the SIRT1/FOXO interaction, the redox sensitive/modulating transcription factor Nrf2 also has a pivotal role into the SIRT1 axis pathway. Indeed, the deacetylation of Nrf2 by SIRT1 promotes its stability and activity [194]. In accordance, AFSC-EV exposure increased Nrf2 levels, together with its target genes, HOx1 and SOD1. Additionally, the indirect Nrf2 activation way is represented by p21, that suppresses cell transition from G1 to S phase and it is in turn activated by FOXO3a [195]. The SIRT1/FOXO3a cell regulatory function linked to oxidative stress can be a fundamental self-defense mechanism to counteract uncontrolled ROS accumulation [196]. Moreover, recent evidence hypothesized a protective function of p21 by preventing apoptosis in some reversible damage circumstances. Furthermore, p53 is a gene regulator for p21 and, since p53 is strictly linked to apoptosis, the downregulation of p21 could affect the apoptosis pathway. On the other hand, p21 expression is necessary during DNA repairing processes, arresting the growth, and giving to the cell the time necessary to correct the damage [197]. Furthermore, the tumor suppressor p53 and its homologues, p63 and p73, have a central role in the regulation of DNA damage response, cellular homeostasis, development, aging, and metabolism. The loss of both, p63 and p73, prevents the cell death after DNA damage, even the functional content of p53, confirming their implication in cellular apoptosis [198]. Moreover, the role of all, p53, p63, and p73, in the autophagy process should not be overlooked [199].

Since during the early phases of DNA damage response, the p53 binding protein 1 (p53BP1) action and the downstream of H2AX are fundamental [200], we investigated their levels by 53BP1 and pH2A immunofluorescence staining. Notably, AFSC-EV pre-incubation prevented the increase of both these markers caused by Dexa, suggesting a protecting role from DNA damage. In parallel, all the apoptosis markers were beneficially modulated by AFSC-EVs. In addition, Galectin-3 is an anti-apoptotic protein that plays its role preventing p53-induced cells death, and in turn p53 phosphorylation at serine 46 has be linked to the repression of Galectin-3 [201]. Curiously, we previously found a high score for Galectin-3 binding protein presence into AFSC-EVs [169]. Recently, it has also been demonstrated the central role of Galectin-3 in osteoblast differentiation modulating splicing patterns of different genes [171,202,203]. In fact, the proteomic analysis permitted us to explore the nuclear protein pattern promoted by extracellular vesicles, showing an increase in Galectin-3 expression in those nuclei of pre-osteoblast treated with EVs. Interestingly, different genes, normally over-expressed during osteogenic differentiation, were identified only in EV-exposed conditions (data not shown), but, despite this, only proteins that are expressed in both samples will be discussed in this work. For example, AP-1 complex β1 was found more expressed in AFSC-EV treated cells: it can interact with c-Jun forming a transcription factor highly expressed in proliferating osteoprogenitors, that promotes bone formation targeting bone sialoproteins, osteocalcin, and alkaline phosphatase promoters [204]. Conversely, we found in EV-treated samples, compared to untreated ones, a reduction in negative regulators of osteoblast differentiation expression. An example is TP53, whose pathway activation was linked to consequent cell apoptosis, and which could impair development and in particular also the ossification process [205].

In conclusion, all these evaluations suggest the pro-osteogenic potential of AFSC-EVs observed in both, undifferentiated and under differentiation HOB cells, that could contribute, together with their anti-inflammatory and antioxidant effect, to slow the progression of the age-related bone loss.

Chapter III – Human neuromuscular junctions on a chip: impact of AFSC-EVs on muscle atrophy and nerve health

5.1 Introduction

5.1.1 Muscle atrophy: from the pathogenesis to the cellular mechanisms

Skeletal muscle is a plastic tissue maintained by different pathways that regulate cell and protein turnover [206]. During aging, its regenerative potential is hampered, and the consequent loss of muscle mass, strength, and function greatly affects the quality of life in elderly population. Similarly, to the other age-related conditions, also muscle atrophy is mainly characterized by a low-grade of chronic inflammation and oxidative stress, accompanied by the loss in resident stem cells, and consequent regenerative ability.

Into the high complexity of muscle atrophy pathogenesis, unbalanced protein synthesis and degradation have been involved [207]. The two most important cell proteolytic systems that control muscle protein turnover are the ubiquitin-proteasome and the autophagy-lysosome machinery [206]. During muscle loss, the most strongly induced atrophy-related genes, also known as “atrogenes”, are those that encodes for two muscle-specific ubiquitin ligases, atrogin-1 (also called MAFbx) and MuRF1 [208,209]. Among many, the crucial regulators of atrogenes are JNK, AMPK, FOXO3, and NFκB. Despite the high complexity of the signaling pathway and transcriptional program networks involved in regulating muscle proteostasis, here we will mainly discuss the FOXO signal pathway.

Indeed, FOXO3 is a central player in muscle wasting-related catabolic events, regulating both metabolism and oxidative stress defenses. In particular, FOXO3 promotes the ubiquitin-proteasome system, *via* atrogin-1 and MuRF1 up-regulation, and the autophagy-lysosome system as well, *via* beclin-1, LC3β, and other autophagy-related genes [175,210,211]. In physiological conditions, the up-regulation of all these genes by FOXO3 is blocked by Akt. Indeed, the phosphorylation of FOXO3 by Akt prevents its translocation into the nucleus and, thus, its transcriptional activity [210]. So, when Akt is active the proteolysis is suppressed, while when FOXO3 is induced protein degradation is stimulated. This is not trivial, because FOXO activity is controlled by numerous post-translational modifications, such as phosphorylation, acetylation, and mono- or poly-ubiquitylation [212].

Likewise, oxidative stress and ROS unbalance, closely associated with muscle atrophy, are fundamental regulators of proteolysis. Indeed, a recent study of Young and colleagues [213] showed that genetic depletion of SOD1 in mice leads to an increase in oxidative stress, muscle atrophy and weakness, but also accelerates the age-related muscle loss. Interestingly, they also observed a strong simultaneous activation of the two proteolytic systems.

Furthermore, during aging numerous tissues, including skeletal muscle, exhibit mitochondrial dysfunction and ROS over-production [214]. To date, it is still not clear if mitochondrial dysfunction is a cause or a consequence, but it is certain their role in overall muscle aging. Indeed, during muscle loss, mitochondria go through different detrimental modifications characterized by down-regulation of PGC-1α and antioxidant defense, increased ROS production, activated FOXO, NFκB, and inflammation, enhanced ubiquitination, and finally mitophagy and apoptotic cascades [215]. The evidence highlighted the strong implication of mitochondria in age-dependent atrophy.

The growing interest in the study of age-related wasting conditions leads to the necessity to develop new experimental models of muscle atrophy and, among many, we can find Dexamethasone (Dexa). As already seen, Dexa is a synthetic glucocorticoid widely used as treatment to control different pathological alterations linked to inflammation [216]. Despite its beneficial effects, an abuse can lead to skeletal muscle atrophy, mainly *via* two pathways: glucocorticoid receptor (GR)-mediated catabolic processes and the oxidative stress-related pathway [217–219]. Given their mechanism in muscle loss induction, similar to that of aging, GC treatment is largely used in research to set up age-related atrophy models. Indeed, GC administration induces atrogin-1 and MuRF1 expression and muscle loss in both *in vitro* and *in vivo* [209,210]. Interestingly, it has been recently demonstrated that the muscle catabolic activity of GC is, lastly in part, mediated by the transcriptional regulation of FOXO1, and together they cooperate for MuRF1 upregulation. Moreover, Dexa also induces an increase in ROS accumulation, causing antioxidant and pro-oxidant imbalance, that finally leads to proteolysis promotion and proteins synthesis inhibition [218,220–222].

5.1.2 Muscle-nerve cross talk during aging: the role of oxidative stress

During aging, the musculoskeletal impairment is further worsened by the loss of alpha motor neurons (MNs) and negative alterations of neuromuscular junctions (NMJs) [223,224]. NMJs are specialized regions where muscle and nerve can communicate, a fundamental connection to govern vital processes, such as breathing and voluntary movements [225]. Notably, not only MNs can communicate with muscle cells, but also skeletal muscle is a fundamental source of signals that influence neuron survival, axonal growth, and synaptic connection maintenance [225].

In physiological conditions, after neuronal loss, denervated orphan muscle fibers release chemotactic signals which stimulate the growth of new neurites and consequentially, their re-innervation. During aging, these reparatory strategies start failing and the not re-innervated fibers become apoptotic, leading to the decline of muscle functions [226,227]. Additionally, the pathological proteolytic cleavage of agrin, a proteoglycan involved in NMJ formation and maturation, but also in acetylcholine receptors (AChRs) clustering, causes the early onset of muscle loss pathologies [225].

Furthermore, exhaustion of adult satellite cells (SCs), the characteristic muscle stem cell compartment, aggravates this dramatic scenario [228]. This muscle solidity loss leads to perturbations in NMJ morphology that becomes fragmented, and to functional alterations in neuromuscular transmission [229]. This initial NMJ change is accompanied by an increase in inflammatory cytokine production and loss of trophic support with consequent neurodegeneration [230].

Moreover, the age-related increase in oxidative stress and mitochondrial dysfunction are considered central players in the NMJ degeneration and muscle atrophy. The oxygen metabolism compromission, associated with the reduction in mitochondrial energy production and increase of intracellular calcium, intensifies the pre-synaptic decline, and reduces the synaptic vesicles release. The ROS increase, due to mitochondrial dysfunction, in muscles and neural tissues as well, causes the accumulation of damaged cell structures with alteration in their functional activities [225,231]. Interestingly, SIRT3 is an important regulator of cell survival, metabolisms, and stress adaptive response by controlling the mitochondrial functions and metabolism in response to oxidative *stimuli* [232]. As previously described, FOXO3a is one of the most important targets of Sirtuins' family. Through its deacetylation SIRT1 can control mitochondrial homeostasis (mitochondrial biogenesis, fusion/fission/mitophagy) and protect these organelles from oxidative stress, upregulating a set of FOXO3a-dependent mitochondrial antioxidant enzymes, namely SOD1, Prx3, Prx5, and Trx2.

Thus, in this fundamental crosstalk, it has not yet been clarified whether NMJ alterations follow or precede muscle decline and the role that oxidative stress components play under such circumstances (***Figure 4***).

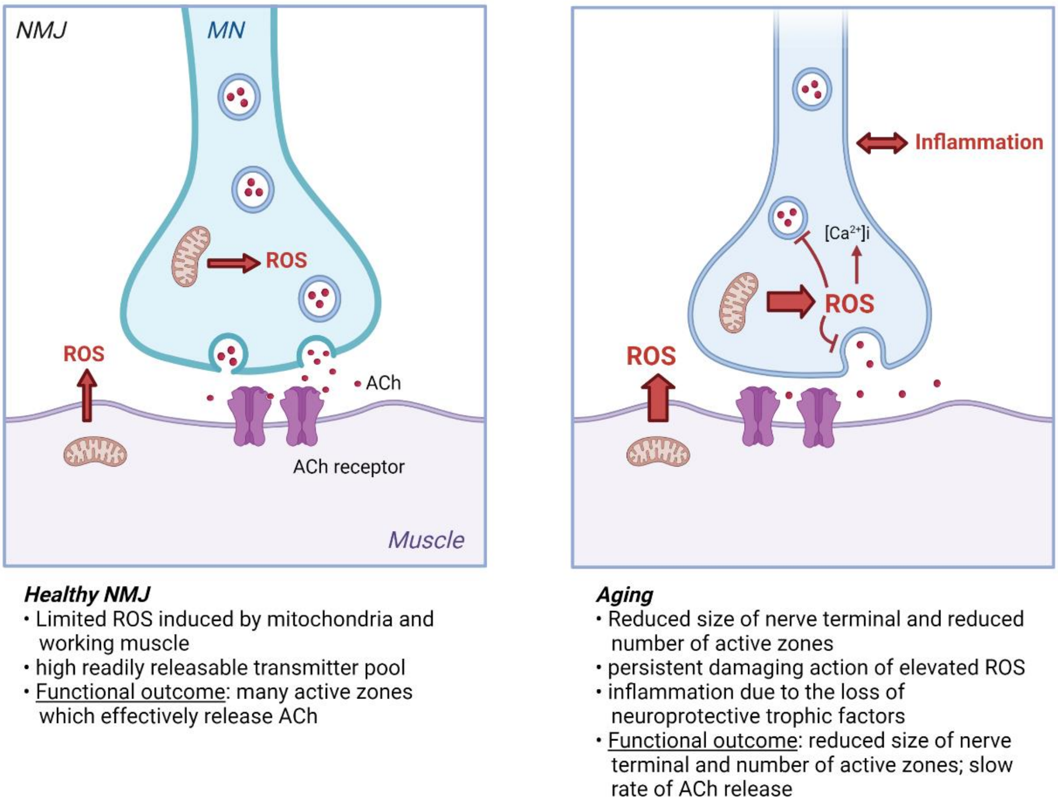

Healthy NMJ
- Limited ROS induced by mitochondria and working muscle
- high readily releasable transmitter pool
- Functional outcome: many active zones which effectively release ACh

Aging
- Reduced size of nerve terminal and reduced number of active zones
- persistent damaging action of elevated ROS
- inflammation due to the loss of neuroprotective trophic factors
- Functional outcome: reduced size of nerve terminal and number of active zones; slow rate of ACh release

Figure 4: Schematic representation of oxidative cross-talk between muscle and MNs in healthy and aged conditions. Image Created with BioRender.com.

5.1.3 Application of MSCs and their secretome in muscle-atrophy related dysfunctions

Several efforts have been directed through the identification of novel treatments to promote skeletal muscle regeneration in acute and chronic conditions. MSC derived from different sources are being investigated for their potential to regenerate and repair muscle tissues. Indeed, MSCs can induce the proliferation and differentiation of resident muscular stem cells, but also reduce inflammation acting on the other cellular components of muscle niche [119]. Recent works demonstrated that MSCs have interesting potential to regenerate or repair skeletal muscle that has been damaged by acute or chronic injuries, including muscular dystrophies and atrophy [233–235].

Interestingly, Kim et al. demonstrated that MSCs isolated from different sources (bone marrow, adipose tissue, and umbilical cord) can stimulate muscle regeneration after *in vivo* transplantation in rats with hindlimb suspension-induced muscle atrophy [233], by activating PI3K/Akt pathway that leads to the reduction of the atrogene expressions. Furthermore, in an amyotrophic lateral sclerosis (ALS) model (SOD1-G93A mice) intravenous injection of BM-MSCs has been demonstrated effective in reducing the inflammatory response and the MN loss with consequent atrophy and loss of muscle movements [236,237].

Recently, the research has moved through the study of MSC-secretome, including the vesicular part. Several works attributed the beneficial effects of EVs to their cargo. Among the numerous components, it has been seen the presence of myogenic (miR-1, miR-133, and miR-206 [238,239], anti-inflammatory (i.e., miR-let7 family) and regenerative (i.e., miR-145) miRNAs [240].

Interestingly, a study of Mellow et al. [241] described the beneficial effect of secretome (the whole CM as well as the EV part) derived from AFSCs on muscle homeostasis, thanks to their anti-inflammatory potential, their ability to enhance proliferation, and their capacity to protect against cellular senescence in an *in vivo* model.

The interest in MSC-EVs for the treatment of degenerative neuromuscular diseases has also intensified because of their ability to cross the BBB in a non-invasive manner [242]. Indeed, using *in vitro* models of ALS, it has been observed that the transfer of SOD1 and SOD3 through EVs counteracted the free superoxide radicals improving the response to oxidative stress [243].

Concluding, several pre-clinical studies demonstrated that the beneficial effect of MSC secretome in skeletal muscle regeneration could be partially due to secreted EVs, which can mirror the positive action of their originating cells. EV therapy is a promising option to avoid concerns about the application of live cells.

5.2 Materials and Methods

5.2.1 Derivation, maintenance, and treatment of human Mesoangioblasts

Human Mesoangioblasts (hMABs) were isolated as previously described [244,245]. hMABs were cultured on collagen from calf skin-coated flask in IMDM growth medium (Sigma, Milan, Italy) supplemented with 1% sodium pyruvate, 1% non-essential amino acids, 1% L-glutamine, 1% insulin transferrin selenium (all from EuroClone Spa, Milano, Italy), 5ng/ml recombinant human basic fibroblast growth factor (bFGF) (PeproTech, Rocky Hill, NJ, USA). Medium was changed every 3 days. Since physical contact between hMABs initiates fusion and reduces the myogenic potential, cells were trypsinized not over 70% of cell confluence [246]. To induce myotube differentiation, confluent hMABs were exposed for 1 week to a differentiation medium composed of 1:1 DMEM/F12 (Life Technologies, Thermo Fisher Scientific, Waltham, MA, USA) supplemented with 2% horse serum (Thermo Fisher Scientific, Waltham, MA, USA) and 1% sodium pyruvate (EuroClone Spa, Milano, Italy). In order to induce muscle atrophy, mature myotubes were treated with 20µM Dexamethasone (Sigma Aldrich, St Louis, MO, USA) in the differentiation medium for 20 minutes (for ROS analysis) or 24 hours (for all other experiments). AFSC-EV treatment (1,3 x 10^8 particles/cm^2) was added 24 hours before Dexamethasone (Dexa) treatment and maintained for the glucocorticoid treatment time.

5.2.2 Differentiation of iPSCs into mature Motor Neurons and treatment

To obtain mature motor neurons (MNs) from human iPSCs, Dittlau et al. protocol was applied [246,247]. Human iPSCs (Gibco, Waltham, MA, USA) were harvested using Collagenase type IV (Gibco, Waltham, MA, USA), transferred into Ultra-low attachment Multi-6 well (Corning Manassas, VA, USA) to promote embryo body formation and maintained in Neuronal medium (50% DMEM/F12 and 50% Neurobasal Medium (both from Life Technologies, Thermo Fisher Scientific, Waltham, MA, USA) with 2 mM L-glutamine, 100 U/mL penicillin, and 100 µg/mL streptomycin (all from EuroClone Spa, Milano, Italy), 1% N2 supplement, 2% B-27^{TM} without vitamin A, 0.1% β-mercaptoethanol (all from Thermo Fisher Scientific, Waltham, MA, USA), 0.5 µM ascorbic acid (Sigma-Aldrich, Milan, Italy) supplemented with 5 µM Y-27632 (Merk Millipore, Burlington, MA, USA), 0.2 µM LDN-193189 (Stemgent, Beltsville, MA, USA), 40 µM SB431542, and 3 µM CHIR99021 (both from Tocris Bioscience, Bristol, UK) for 2 days changing medium every day. On day 2, Neuronal medium was supplemented with 0.1 µM retinoid acid (Sigma-Aldrich, Milan, Italy), 500 nM smoothened agonist (SAG) (Merk Millipore, Burlington, MA, USA), and refreshed on day 4. On day 7, medium was changed again with the same of day 4 supplemented with brain-derived neurotrophic factor (BDNF) 10 ng/mL and glial cell-derived neurotrophic factor (GDNF) 10 ng/mL (Peprotech, Rocky Hill, NJ, USA). On day 9, day 7 medium was supplemented with 20 µM DAPT (Tocris Bioscience, Bristol, UK) and the well plates required were coated using 100 µg/mL poly-L-ornithine (PLO) in DPBS for 3 hours and then 20 µg/mL laminin (both from Sigma, St Louis, MO, USA) in Neurobasal medium (Life Technologies, Thermo Fisher Scientific, Waltham, MA, USA) overnight. On day 10, embryo bodies were dissociated into single cell neural progenitor cells (NPC) using 0.05% trypsin (Gibco, Waltham, MA, USA), and then, cryopreserved or seeded into previously coated well plates or devices. For monocultures, days 10-11 neuronal progenitor medium was the same as day 9. From day 11, medium was not changed completely, but 50% medium replacement were performed. On day 14, medium was composed by Neuronal medium supplemented with 10 ng/mL BDNF, 10 ng/mL GDNF (Peprotech, Rocky Hill, NJ, USA), and 20 µM DAPT (Tocris Bioscience, Bristol, UK). On day 16, medium was partially replaced again with day-14 medium supplemented with ciliary neurotrophic factor (CNTF) (Peprotech, Rocky Hill, NJ, USA) and from day 18 medium was refreshed every 2 days with Neuronal medium supplemented with neurotrophic factors (NTF) (BDNF, GDNF, and CNTF (all 10 ng/mL)). To test the effect of Dexamethasone on mature motor neurons, at day 27 of differentiation, Dexa treatment was applied at the concentration of 20µM for 24 hours in 18-day Neuronal medium.

5.2.3 Preparation of microfluidic devices

Microfluidic devices (Xona^{TM} Microfluidics, Temecula, CA, USA; Cat N° XC150) were sterilized in 90% ethanol and left to air-dry in sterile laminar flow. Devices were placed individually in 10 cm petri dishes for easy handling. Before cell seeding, devices were coated using 100 µg/ml poly-L-ornithine (PLO) in DPBS for 3 hours and then 20 µg/ml laminin (both from Sigma, St Louis, MO, USA) in Neurobasal medium (Life Technologies, Thermo Fisher Scientific, Waltham, MA, USA) overnight. All coated materials were incubated at 37°C, 5% CO_2, and a volume difference of 100 µl between two sides was applied to allow the coating to pass through the microgrooves (maximum capacity for each device well: 200

µl). The day after, devices were carefully washed once with DPBS before neural cells plating.

5.2.4 Co-culturing myotubes and MNs in microfluidic devices and treatments

Myotubes and MNs were co-cultured into Xona^{TM} microfluidic devices according to a previously described protocol [248]. Briefly, day 10 MN-NPC were seeded into one side of devices at 1,25 x 10^5 cells/well (total 2,5 x 10^5 cells/side) and maintained in day-specific differentiation medium according to the differentiation protocol (100 µL day-10 medium). Same volume and composition medium was added also to the other compartment without cells, and into both compartment mediums was changed on days 11, 14 and 16 according to medium composition protocol described in the previous section. After 1 week (on day 17), hMABs were seeded into the opposite compartment (10^5 cells/well, total 2 x 10^5 cells/side) in growth medium (described in *Section 5.2.1*), and no medium change were required for MN compartment. The following day myotube differentiation was started (differentiation medium described in *Section 5.2.1*) while into MN-side medium was replaced with Neuronal medium supplemented with 10 ng/mL NTF (day 18-medium). On day 21, a chemotactic and volumetric gradient was established. Neuronal compartment received 100 µL/well of Neuronal medium without neurotrophic factors, while myotube compartment received 200 µL/well neuronal medium supplemented with 30 ng/mL BDNF, GDNF, CTNF (all from PeproTech, Rocky Hill, NJ, USA), 20 µg/mL laminin (Sigma, St Louis, MO, USA) and 0.01 µg/mL recombinant human agrin protein (R&D Systems, Minneapolis, USA). The gradient and laminin/agrin treatment were maintained until the co-culture end. At day 26, AFSC-EVs were added to both compartments (4,16 x 10^7 particles/well), and after 24 hours only myotube compartment was also treated with 20 µM Dexamethasone for 20 minutes for oxidative stress analysis or 24 hours for all other analysis.

5.2.5 RNA isolation and quantitative real-time PCR

For quantitative Reverse Transcription Polymerase Chain Reaction (RT-qPCR) assay, Purelink® RNA mini kit (Thermo Fisher Scientific, Waltham, MA, USA) was used to isolate total RNA, and RNA samples were purified by TurboTM DNA-free kit (Thermo Fisher Scientific, Waltham, MA, USA) [249].1 µg of RNA was reverse-transcribed using Superscript

III Reverse Transcriptase First-Strand Synthesis SuperMix (Thermo Fisher Scientific, Waltham, MA, USA), according to the manufacturer's protocol. Platinum SYBR Green QPCR SuperMix-UDG (Thermo Fisher Scientific, Waltham, MA, USA) was used to dilute cDNA (1:5). The RT-qPCR was performed by Viia7 384-plate reader (Thermo Fisher Scientific, Waltham, MA, USA). Oligonucleotide primer forward/reverse sequences are listed in ***Table 4***.

Table 4 *- List of primers used for gene expression analysis.*

GENE	PRIMER SEQUENCE (5'-3')	GENE	PRIMER SEQUENCE (5'-3')
h-SIRT2	Fw: CTGCGGAACTTATTCTCCCAGAC Rev: CCACCAAACAGATGACTCTGCG	**h-OCT4**	Fw: CCTGAAGCAGAAGAGGATCACC Rev: AAAGCGGCAGATGGTCGTTTGG
h-SIRT3	Fw: GCTGGACAGAAGAGATGC Rev: GTGGATGTCTCCTATGTTACC	**h-SOX2**	Fw: GCTACAGCATGATGCAGGACCA Rev: TCTGCGAGCTGGTCATGGAGTT
h-FOXO3	Fw: TCAAGGATAAGGGCGACAGC Rev: GGACCCGCATGAATCGACTA	**h-SOX17**	Fw: ACGCTTTCATGGTGTGGGCTAAG Rev: GTCAGCGCCTTCCACGACTTG
h-LC3β	Fw: GAGAAGCAGCTTCCTGTTCTGG Rev: GTGTCCGTTCACCAACAGGAAG	**h-NESTIN**	Fw: TCAAGATGTCCCTCAGCCTGGA Rev: AAGCTGAGGGAAGTCTTGGAGC
h-BECLIN	Fw: CCATGCAGGTGAGCTTCGT Rev: GAATCTGCGAGAGACACCATC	**h-OLIG2**	Fw: ATGCACGACCTCAACATCGCCA Rev: ACCAGTCGCTTCATCTCCTCCA
h-MHC1	Fw: GCTGGCTAAGACCGAGGCAAAA Rev: CCTTTCCTCTGCATCAGCCAAG	**h-HB9**	Fw: GCCTAAGATGCCCGACTTCAAC Rev: CGCGACAGGTACTTGTTGAGCT
h-MHC3	Fw: CTGGAGGATGAATGCTCAGAGC Rev: CCCAGAGAGTTCCTCAGTAAGG	**h-ISL1**	Fw: GCAGAGTGACATAGATCAGCCTG Rev: GCCTCAATAGGACTGGCTACCA
h-PAX	Fw: GGGCCTCCTGCTTGTTTAT Rev: CCATCTGGCTGGACTTCAAT	**h-MAP2**	Fw: AGGCTGTAGCAGTCCTGAAAGG Rev: CTTCCTCCACTGTGACAGTCTG
h-DESMIN	Fw: GAAGCTGCTGGAGGGAGAG Rev: ATGGACCTCAGAACCCCTTT	**h-βTUB3**	Fw: TCAGCGTCTACTACAACGAGGC Rev: GCCTGAAGAGATGTCCAAAGGC
h-SOD1	Fw: GGTGGGCCAAAGGATGAAGAG Rev: CCACAAGCCAAACGACTTCC	**h-CASP3**	Fw: GGAAGCGAATCAATGGACTCTGG Rev: GCATCGACATCTGTACCAGACC
h-GPX	Fw: CAGTCGGTGTATGCCTTCTCG Rev: GAGGGACGCCACATTCTCG	**h-CASP8**	Fw: AGAAGAGGGTCATCCTGGGAGA Rev: TCAGGACTTCCTTCAAGGCTGC
h-PDRX3	Fw: ACAGCCGTTGTCAATGGAGAG Rev: ACGTCGTGAAATTCGTTAGCTT	**h-CASP9**	Fw: GTTTGAGGACCTTCGACCAGCT Rev: CAACGTACCAGGAGCCACTCTT
h-TRXR3	Fw: ATGAGGCTGTTAGACCTCTGC Rev: GGCGACAATGGCATTCACATC	**h-GAPDH**	Fw: TCAAGAAGGTGGTGAAGCAGG Rev: ACCAGGAAATGAGCTTGACAAA
h-NANOG	Fw: CTCCAACATCCTGAACCTCAGC Rev: CGTCACACCATTGCTATTCTTCG		

5.2.6 Immunofluorescence Confocal Microscopy and Image Analysis

For immunofluorescence analysis, cells seeded on coverslip were processed and confocal imaging was performed using a Nikon A1 confocal laser scanning microscope, as previously described (*Section 4.2.8*). Microfluidic devices were processed as previously described by Dittlau et al. [246]. Cells were washed twice with DPBS and then fixed with 4% paraformaldehyde (PFA) in DPBS for 30 minutes at RT. After fixation, fixed cells were washed twice and then permeabilized with 0.1% Triton X-100 for 20 minutes (Sigma-Aldrich, Milan, Italy). Unspecific binding sites were blocked with 3% BSA/DPBS (Sigma-Aldrich, Milan, Italy) for 30 minutes at RT. After blocking, cells were incubated with primary antibodies diluted in 3% BSA/DPBS in a wet chamber overnight at 4°C. To ensure labeling of neurites into microgrooves, a volume gradient was performed (100 µL/well of antibody solution on one side of the microgrooves and 150 µL/well on the other side). The day after, 3 washing with 3% BSA/PBS were performed before secondary antibodies incubation for 1 hour, at RT in the dark (as described above a volumetric gradient was applied). Then, cells were washed twice with DPBS, and nuclei were stained with 4',6-diamidino-2-phenylindole (DAPI) for 20 min at RT (dark). After 2 washing, DPBS was removed and the culture was let dry for a few seconds before adding 1 drop of anti-fading medium (0.21 M DABCO, 90% glycerol in 0.1 M Tris pH 8.0) in each well. Devices were kept horizontal for at least 24 hours to allow the mounting media to set and after that, devices can be stored at 4°C or visualized using a Nikon A1 confocal laser scanning microscope.

Primary antibodies to detect neurofilament heavy chain (NEFH) (Abcam, Cambridge, UK), synaptophysin (SYPH) (Cell Signaling Technology, Lieden, Netherlands), Islet-1 (Isl-1) (Millipore, Burlington, MA, USA), β-tubulinIII (βTubIII) (Cell Signaling Technology, Lieden, Netherlands), myosin heavy chain (MyHC) (In-house, SCIL, dil. 1:20) were used following the datasheet-recommended dilutions. α-Bungarotoxin-tetramethylrhodamine (Sigma-Aldrich, MO, USA) was incubated with secondary antibodies according manufacturer's protocol. Alexa secondary antibodies (Thermo Fisher Scientific, Waltham, MA, USA) were used at 1:200 dilution. To obtain three-dimensional projections, the confocal serial sections were processed with ImageJ software, while image rendering was performed with Adobe Photoshop software. For myotube fusion index, nuclei per myotube, myotube thickness analyses, and NMJ quantification, MyHC positive cells containing multiple nuclei were selected as myotubes. For NMJ quantification into microfluidic devices, 40X magnification images of MyHC positive-myotubes were collected using an inverted confocal microscope. The number of co-localizations between NEFH/SYPH and α-bungarotoxin (αBtx) (Sigma, St Louis, MO, USA), for Acetylcholine Receptor (AChR) identification, was counted manually through each z-stack, and the number of co-localizations was normalized to the number of myotubes present in the z-stack. NMJs morphology, single or multiple contact point, were analyzed looking at neurite interaction with AChR clusters, as previously described by Dittlau et al., 2021 [246]. Briefly, NMJs were identified as single contact point when a neurite touched once a AChR cluster, while multiple contact point when neurite will fan out and engage with the AChR cluster over a larger surface.

5.2.7 Neurite Density-Outgrowth Quantification

Neurite density-outgrowth quantification was performed as previously described by Dittlau et al. 2021 [248]. Briefly, tile scan images of NEFH fluorescence into myotube compartment were taken using an inverted Leica SP8 DM18 confocal microscope and neurites were isolated using Ilastik 1.3.3post1 Pixel Classification software. A custom ImageJ 1.52p software linear School analysis script was used to quantify the total number of pixels that intersect an intersection line (distance between lines: 50 µm). Measure was started at 100 µm distance from the microgrooves due to the high neurite density at the exit of microgrooves.

5.2.8 Calcium Fluorescent Imaging

After AFSC-EV and/or Dexamethasone treatments, to the myotube compartment was added with 5 µM Fluo-4 AM (Thermo Fisher Scientific, Waltham, MA, USA) for 25 min at dark (5% CO_2, 37°C). MNs were stimulated with 50 mM KCl and Fluo-4 fluorescence was recorded in the myotube compartment (1 picture/second for a total of 60 seconds, 10X magnification). The fluidic isolation of compartments in the microfluidic device ensured no passage of KCl solution to myotube side. Recordings were acquired and analyzed using a Nikon A1R confocal microscope and NIS-Elements AR 4.30.02 software.

5.2.9 ROS Detection

To evaluate the intracellular ROS levels, a dichlorodihydrofluorescein diacetate (DCFH-DA) assay was performed as previously described (*Section 4.2.3*). For myotube oxidative stress investigation, hMABs were seeded and differentiated into 96-well plates with 5 replicates for each condition, while for co-culture oxidative stress analysis myotubes and MNs were cultured in microfluidic devices as described above. Culture medium was removed from each well and 5 µM DCFH-DA was incubated in PBS with 1 gr/L of glucose for 20 min at 37°C and 5% CO_2. Dexamethasone treatment was only added to myotubes with the probe at the mean time and maintained for 20 minutes. Into 96-well plates, the probe solution was replaced with PBS/glucose solution and the fluorescence was read at 485 nm (excitation) and 535 nm (emission) using the multiwell reader Appliskan (Thermo Fisher Scientific, Waltham, MA, USA). Cellular autofluorescence was subtracted as a background using the values of the wells not incubated with the probe. For devices, after Dexa treatment, the probe solution was replaced with PBS/glucose solution and the neurite fluorescence was recorded for 8 minutes into the muscle compartment with a Nikon A1 confocal laser scanning microscope equipped with a live cell imaging system. Live images were taken between microgrooves exit and myotubes in order to select the neurites most likely to have contacted myotubes and to avoid myotube fluorescence noise.

5.2.10 Mitochondrial Oxidative Stress Analysis

Confocal images were obtained using a Nikon A1 confocal laser scanning microscope equipped with live cell imaging system. During live imaging, cells were maintained in a PBS-glucose (1g/L) solution at 37°C, 5% CO_2. All acquisition settings, including detector sensitivity and camera exposure time, were maintained constant during recording. To avoid photobleaching and to reduce cell stress, laser power was set to minimum. To identify mitochondria, at day 27 – after 24 h of hAFSC-EVs exposure – both microfluidic device-compartments were washed once with PBS/glucose buffer and then incubated with 100 nm MitoTracker^{TM} Green FM probe (Invitrogen, Waltham, MA, USA) in PBS/glucose solution, and, only myotube compartment, with 20 µM Dexamethasone for 20 minutes at 37°C, 5% CO_2. After the first 10 minutes, 5 µM MitoSox^{TM} Red was added to both compartments to identify mitochondrial superoxide production. After the incubation time, microfluidic devices were gently washed 3 times and maintained in PBS/glucose during live imaging analysis. MitoSox^{TM} and MitoTracker^{TM} fluorescence was recorded in myotube compartment next to the microgrooves exit (20X magnification, with 10 seconds interval for a duration of 8 minutes). MitoSox^{TM} signal was normalized on MitoTracker^{TM} for each time point.

5.2.11 Statistical analysis

All the experiments were performed in 3 biological replicates. For quantitative comparisons, the values were reported as the mean ± SD based on a triplicate analysis for each sample. One-way ANOVA with Bonferroni post hoc test or a Student's *t*-test were applied to test the significance of the observed differences amongst the study groups. Statistically significant was considered a p-value < 0.05. Statistical analysis and plot layout were obtained by using GraphPad Prism® release 8.0 software.

5.3 Results

5.3.1 AFSC-EV effect on an in vitro model of muscle atrophy induced by Dexamethasone

Muscle atrophy was induced *in vitro* by myotube treatment with 20 µM Dexa for 24 hours. The analysis of myotubes, stained with marker of mature myotubes myosin heavy chain (MyHC), showed a decrease in fusion index, number of nuclei per myotube, and above all myotube thickness, the main sign of muscle atrophy, after Dexa treatment. However, AFSC-EVs exposure restored all these differentiation indexes (***Figure III.1A***).

Increasing studies link the age-related atrophy to reactive oxygen species (ROS) rise and oxidative stress unbalance [250,251]. Considering this, we investigated the ROS level alterations at an early time – 20 minutes – of atrophy induction (***Figure III.1B***). Interestingly, we observed a significant increase in oxidative stress, indeed prevented by AFSC-EVs. Furthermore, AFSC-EV capability to reduce the structural alterations occurring during *in vitro* atrophy induction was also confirmed by gene expression analysis (***Figure III.1C***). Indeed, the reduction of MYHC1, MYHC3 and PAX3 expression after Dexa exposure, was prevented by EVs pre-treatment. Conversely, the expression of structural protein Desmin increased in presence of Dexa while not in AFSC-EV treated condition.

Among the redox-sensitive signal pathways, the expression SIRT3 and FOXO3, main regulators of oxidative stress defenses and the autophagy/mitophagy process during muscle atrophy [215], were investigated. The transcriptional factor FOXO3 and the autophagy-related genes (LC3β and beclin-1) were up-regulated with Dexa treatment. Notably, EV exposure restored the levels of autophagy-genes LC3β and beclin-1 similar to the untreated condition. Since the broad implication of FOXO3 in the transcription of several gene, including antioxidant defense ones, we observed that the AFSC-EV treatment stimulated a further gene expression increase of both FOXO3 and SIRT1, accompanied by an up-regulation of SOD1, GPX, PDRX3, and TRXR3 genes, codifying for antioxidant proteins (***Figure III.1C***).

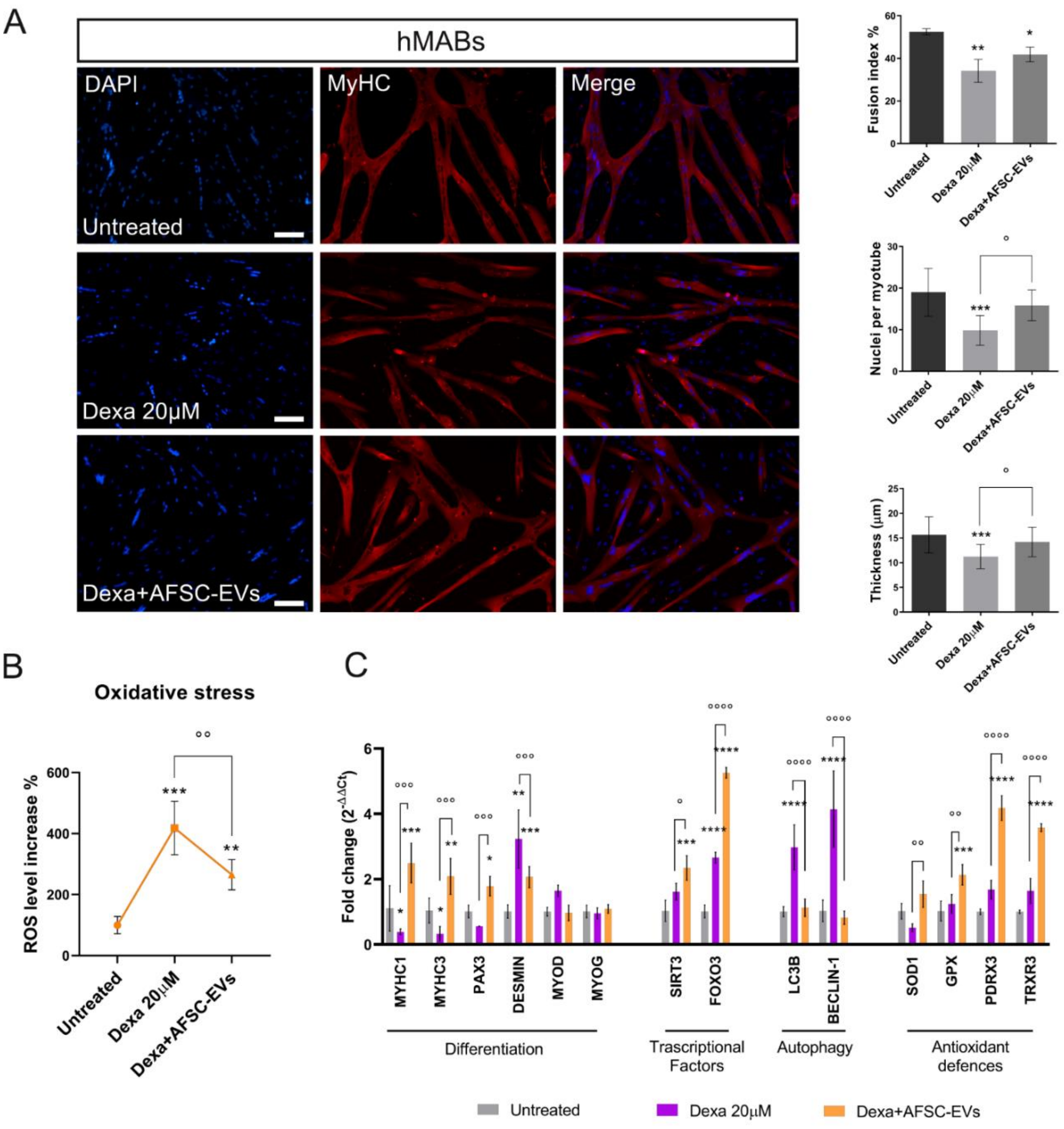

Figure III.1. Effect of human AFSC-EV supplementation on an in vitro model of Dexamethasone-induced atrophy.

(A) Representative images of hMAB-derived myotubes, treated or not with Dexa and AFSC-EVs, stained with myosin heavy chain (MyHC) (red) and DAPI (blue) for nuclei. Scale bars: 50μm. Graphs relative to analysis of fusion index%, nuclei per myotube and myotube thickness (Biological replicates=3). $^{\circ,*}$*p* value < 0.05, ***p* value < 0.01, ****p* value < 0.001.

(B) Graph showing ROS content in myotubes, pre-treated or not with AFSC-EVs for 24 hours, after 20 min of Dexa exposure. Data shown are the mean ± SD (n=5). $^{\circ\circ,**}$*p* value < 0.01, ****p* value < 0.001.

(C) Gene expression comparisons among differentiated hMABs (Untreated), Dexa 20μM, and Dexa+AFSC-EVs. Data shown are the mean ± SD (n=3). $^{\circ,*}$*p* value < 0.05, $^{**,\circ\circ}$*p* value < 0.01, $^{***,\circ\circ\circ}$*p* value < 0.001, $^{****,\circ\circ\circ\circ}$*p* value < 0.0001.

5.3.2 Dexamethasone effect on mature iPSC-MNs

Morphological and functional mature motor neurons (MNs) were obtained from human iPSCs *via* 28-days differentiation protocol previously described by Guo et al. [247]. The up-regulation of typical pan-neuronal (MAP2 and β-TubIII) but also specific motor neuron (HB9 and Islet-1) genes, together with the downregulation of pluripotency markers (i.e., NANOG, SOX2), on day 28 compared to day 10, confirmed the differentiation success (***Figure III.2A***). In addition, mature differentiated MNs expressed synaptophysin (SYPH) and Islet-1 (Isl-1), as shown by IF images (***Figure III.2B***).

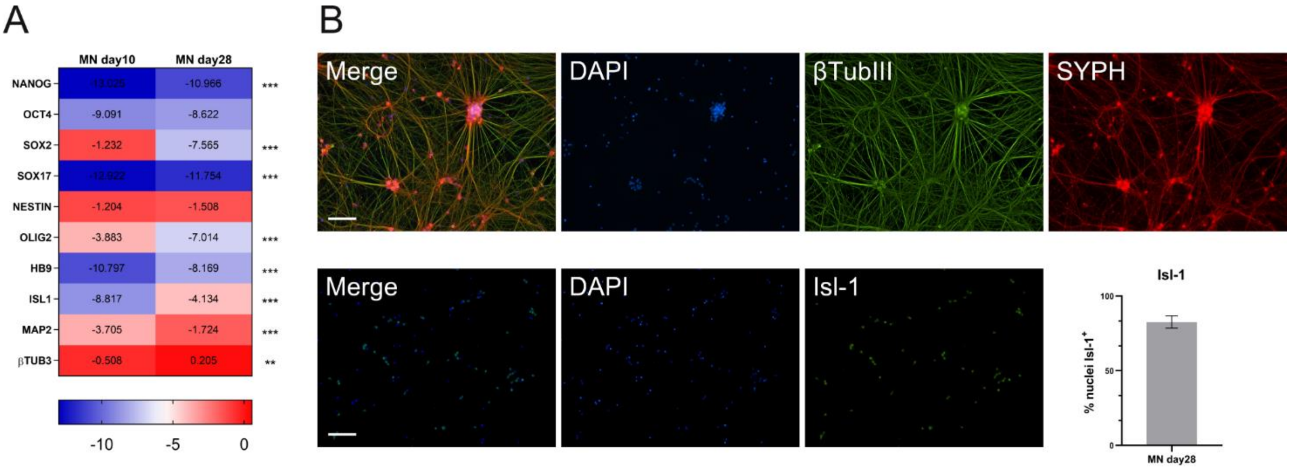

Figure III.2. From human iPSCs to mature motor neurons.

(A) Graph showing gene expression comparison between motor neurons at day 10 and 28 of differentiation for pluripotency, pan-neuronal and motor neuron specific markers. Data shown are the mean ± SD (n=3). $^{**}p$ value < 0.01, $^{***}p$ value < 0.001.

(B) Representative confocal images of MNs at day 28 of differentiation stained with β-tubulinIII (βTubIII) (green), synaptophysin (SYPH) (red) – top –, and Islet-1 (Isl-1) (green) – bottom. Nuclei stained with DAPI. Scale bars: 75µm.

Moreover, to be sure that MN alterations during co-culture experiments were mediated exclusively by atrophic myotubes, by immunofluorescence and RT-qPCR analyses, we demonstrated that 20µM Dexa treatment for 24 hours doesn't affect MN morphology and differentiation potential (***Figure III.3A***), but also the expression of differentiation, redox, and apoptosis related genes (***Figure III.3B***).

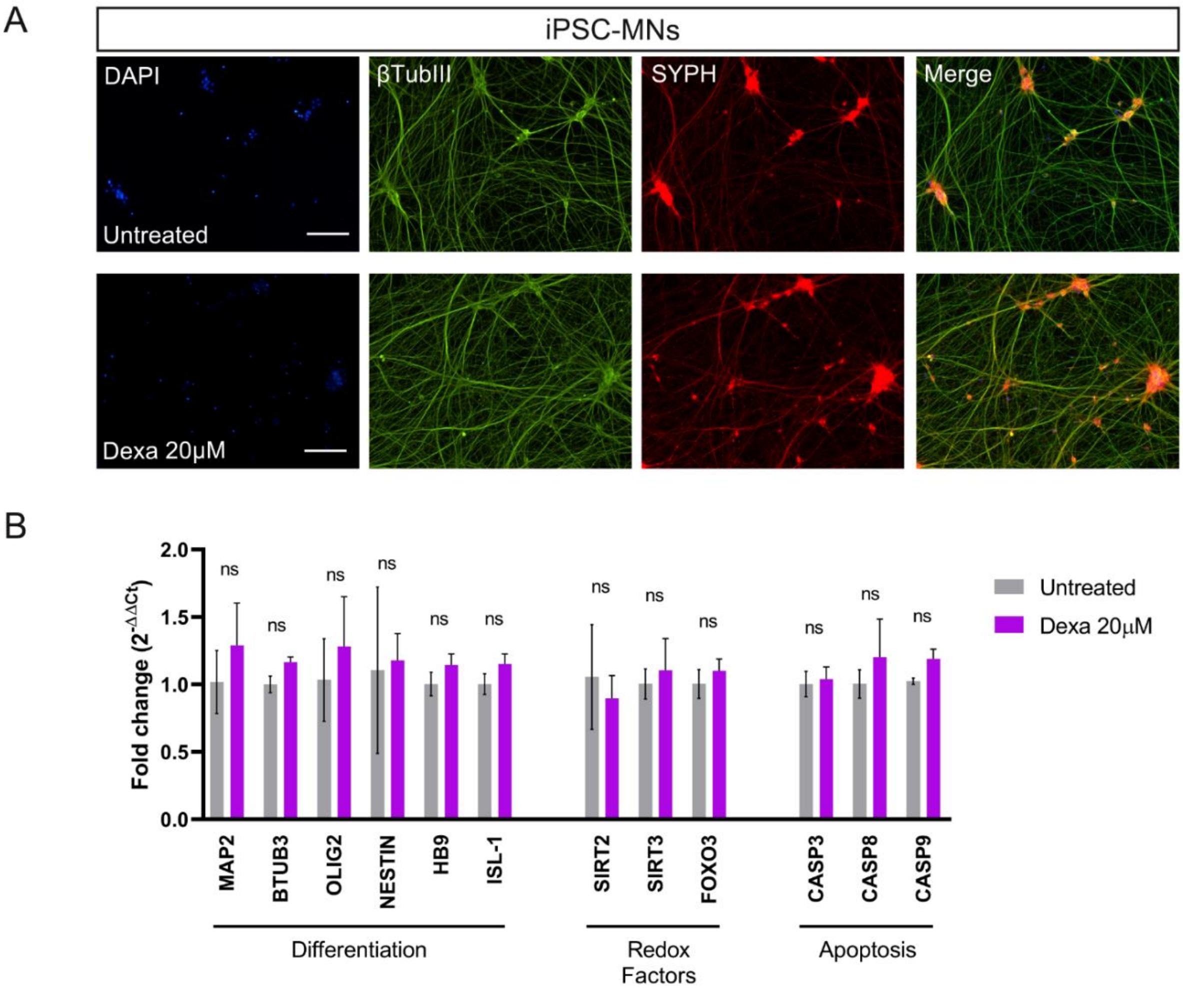

Figure III.3. Effect of Dexa on mature human iPSC-derived MNs.

(A) Representative images of iPSC-derived motor neurons (iPSC-MNs) treated or not with 20 µM Dexa (24 h) stained with β-tubulinIII (βTubIII) and synaptophysin (SYPH). Nuclei stained with DAPI. Scale bars: 75 µm.

(B) Graph showing gene expression comparison of neuronal differentiation, redox factor, and apoptosis markers of MNs treated or not with Dexa. Data shown are the mean ± SD (n=3).

5.3.3 Myotube and neurite distribution into microfluidic devices-muscle compartment and NMJ formation

To explore the result of muscle atrophy on NMJ, an *in vitro* model of MN-myotube co-culture was developed through commercially available microfluidic devices. To study muscle atrophy consequences and then the therapeutic potential of AFSC-EVs, only the muscle compartment was treated with 20 µM Dexa, while both sides with extracellular vesicles. First, we studied the alterations in myotube and neurite distribution. The number of

MyHC positive myotubes was decreased by Dexa treatment, while the presence of AFSC-EVs restored the myotube presence (***Figure III.4A***). Similarly, the analysis of neurite density into muscle compartment showed the capability of EVs in recovering the neurite network affected by atrophic muscle cells (***Figure III.4B***).

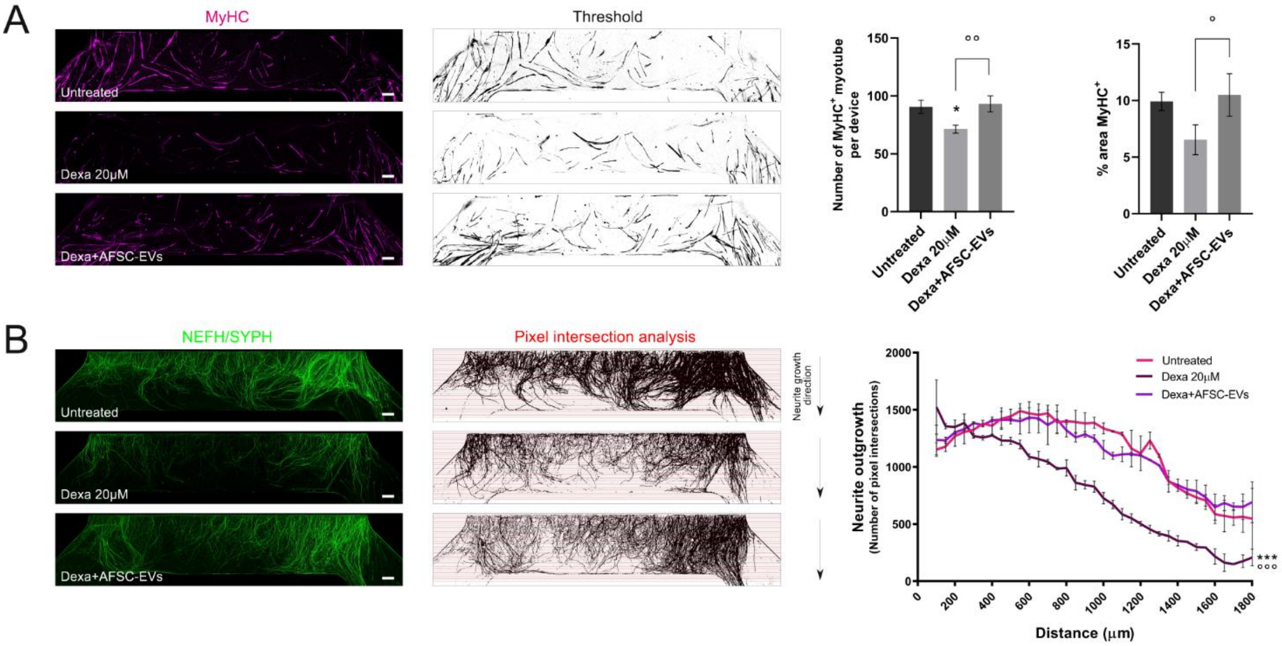

Figure III.4. Density analyses of neurite and hMAB-derived myotube into microfluidic devices muscle-compartment.

(A) Representative tile scan confocal overviews and quantification graphs of hMAB-derived myotubes (MyHC) into muscle compartment after Dexa and AFSC-EVs treatments. Scale bars: 400 µm. Graph data are the mean ± SD (n=3). °,*p value < 0.05, °°p value < 0.01.

(B) Representative tile scan confocal overviews and quantification graph of neurite density (NEFH/SYPH) into myotube compartment after Dexa and AFSC-EVs treatments. Masks of tile scan show intersection lines (red) every 50 µm starting from microgroove exit. Arrows: neurite growth direction from exit of microgrooves. Scale bars: 400 µm. Graph represents quantification of pixel intersection for each intersection line. Graph data are the mean ± SD (n=3). Untreated vs Dexa 20 µM: ***p value < 0.001, Dexa 20 µM vs Dexa+AFSC-EVs: °°°p value < 0.001.

These interesting results were conducted to investigate the repercussion of these alterations on NMJ formation. As previously described by Dittlau and colleagues [246], NMJs were identified as co-localization between αBtx-positive AChRs and neurites on myotubes (***Figure III.5A***).

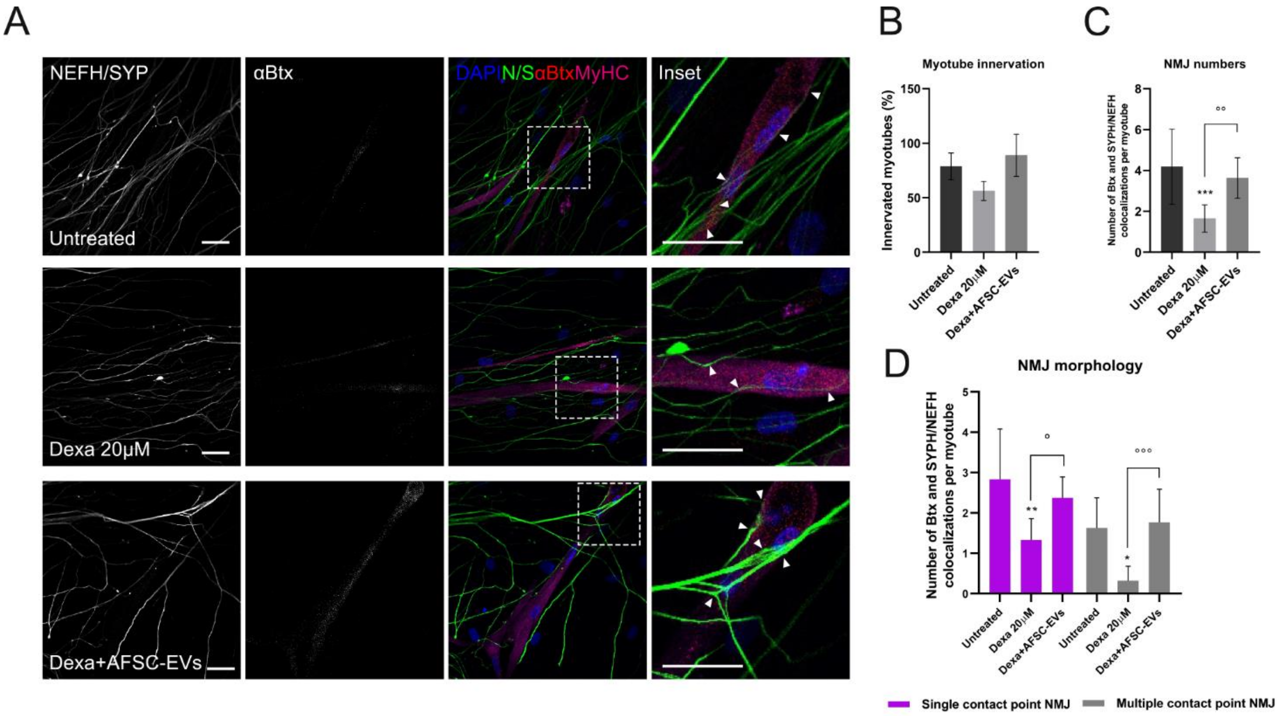

Figure III.5. AFSC-EVs therapeutic potential against NMJ morphology alteration caused by muscle atrophy.

(A) Representative confocal images of NMJs with Dexa and AFSC-EVs treatments. NMJs (arrows) are identified as co-localization between pre-synaptic markers NEFH/SYPH and AChR marker αBtx on MyHC-positive myotubes. Insets: magnification of NMJs. Scale bars: 25 µm.
(B) Percentage of innervated myotubes. Graph data are the mean ± SD (n=3).
(C) Number of α-Btx and NEFH/SYPH co-localization per myotube. Graph data are the mean ± SD (n=3). °°*p* value < 0.01, ****p* value < 0.001.
(D) Quantification of NMJ morphology: single and multiple contact points. Graph data are the mean ± SD (n=3). °,**p* value < 0.05, ***p* value < 0.01, °°°*p* value < 0.001.

Even if not significant, Dexamethasone exposure showed a reduction in innervated myotube percentage, not observed with EVs pre-treatment (***Figure III.5B***), while NMJ numbers decreased significantly only in Dexa-treated condition (***Figure III.5C***). NMJ morphology could be distinguished as less mature single contact point NMJs, when a neurite touches a AChR cluster one time, or multiple contact point NMJs, characteristic of a more mature state of co-culture when neurite will fan out and engage with the AChR cluster over a larger surface [246]. Considering that, both these types of interactions were affected in this atrophy model, while, notably, AFSC-EVs pre-exposure prevented this morphological impairment (***Figure III.5D***).

5.3.4 NMJ functionality after MN-stimulation in atrophic muscle fibers

Previously, we demonstrated that NMJ morphology and number were affected by muscle atrophy. This interesting result led us to explore in deep the possible alterations in their functionality through live-cell calcium imaging (***Figure III.6A***).

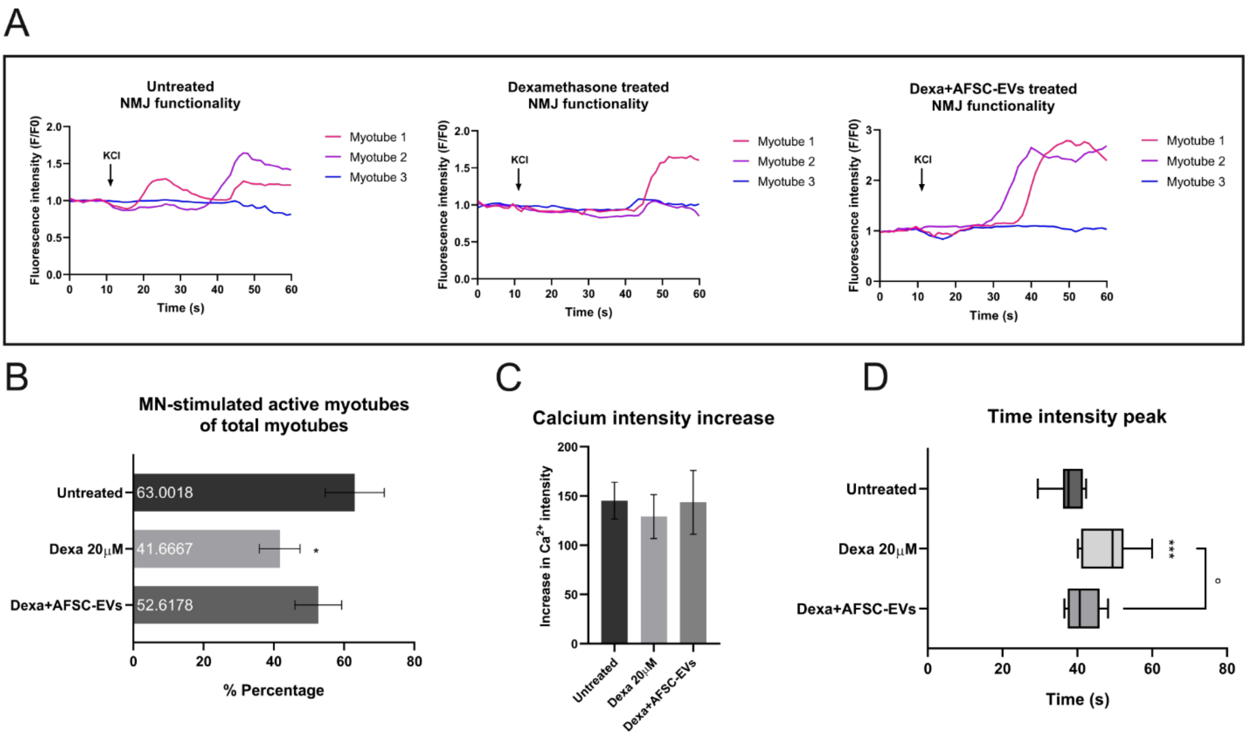

Figure III.6. NMJ functionality after human AFSC-EV and/or Dexa treatments.

(A) Representative Ca^{2+} influx curves into hMAB-myotubes after MN-KCl stimulation (arrow).
(B) Percentage of active hMAB-myotubes after MN-stimulation. Graph data are the mean ± SD (n=3). **p* value < 0.05 (Untreated vs Dexa 20µM).
(C) Ca^{2+} influx intensity after Dexamethasone and AFSC-EV treatment. Graph data are the mean ± SD (n=3).
(D) Graph comparing peak onset times with or without Dexa and AFSC-EV treatment. Graph data are the mean ± SD (n=3). °*p* value < 0.05 (Dexa 20µM vs Dexa+AFSC-EVs), ****p* value < 0.001 (Untreated vs Dexa 20µM).

We observed a significant reduction in the percentage of MN-stimulated active myotubes, compared to the untreated condition, not observed in presence of EVs (***Figure III.6B***). Then, intracellular calcium transient alterations were examined. Even if the reduction in calcium peak intensity was not significant (***Figure III.6C***), this analysis highlighted a delay in Ca^{2+} peak onset after Dexa exposure, index of alteration in NMJ/myotube functional communication (***Figure III.6D***).

5.3.5 Oxidative stress modulation through NMJ by human AFSC-EVs during muscle atrophy

During aging, alterations in oxidative stress and mitochondrial function play a pivotal role in NMJ decline, muscle strength and integrity loss [223]. In order to follow the muscle atrophy consequences on neuronal part, we performed live-imaging assays with fluorescent probes for the detection of intracellular ROS and mitochondrial $O_2^{\bullet -}$. ***Figure III.7A*** shows a schematic representation of experiments.

First, we analyze the oxidative stress rise, during the first 28 minutes of Dexa treatment, into those neurites that had crossed the microgrooves and likely took contact with the myotubes. Interestingly, AFSC-EVs protected MN elongations from ROS increase caused by atrophic muscle cells, in all the investigated time points (***Figure III.7B***).

The implication of mitochondrial superoxide ($O_2^{\bullet -}$) in this oxidative environment was investigated by MitoSox^{TM} live-cell imaging analysis of neurites (***Figure III.7C***). Notably, EVs from AFSC reduced the mitochondrial $O_2^{\bullet -}$ levels increased in Dexa-induced atrophy for each investigated time point (***Figure III.7D***).

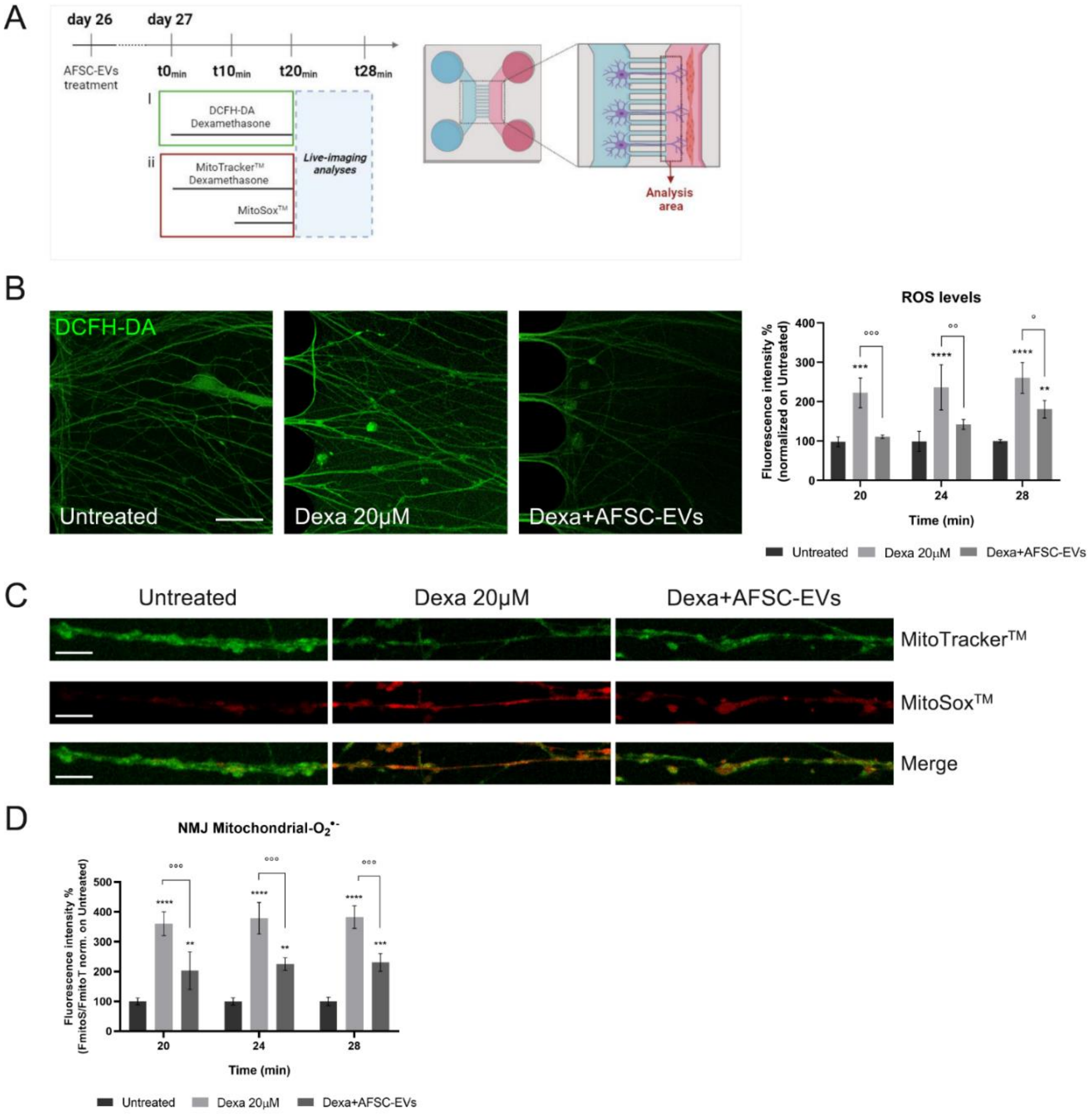

Figure III.7. Human AFSC-EV effect on MN-intracellular ROS and mitochondrial superoxide content in an in vitro co-culture system of muscle atrophy.

(A) Schematic overview of time-treatment for ROS and mitochondrial $O_2^{\bullet -}$ analyses. Created with BioRender.com.

(B) Representative confocal images of MN-neurites stained with DCFH-DA fluorescent probe (green) into hMAB-myotube compartment after 24 minutes of Dexamethasone exposure in presence or absence of AFSC-EVs. Scale bar: 50 µm. Graph shows ROS neurite content after 20, 24, and 28 minutes of Dexamethasone exposure in presence or absence of AFSC-EVs. Graph data are the mean ± SD (n=3). $^{\circ}p$ value < 0.05, $^{**,\circ\circ}p$ value < 0.01, $^{***,\circ\circ\circ}p$ value < 0.001, $^{****}p$ value < 0.0001.

(C) Representative confocal images of MN-neurites stained with MitoTracker^{TM} (green) and MitoSox^{TM} (red) after 24 minutes of Dexamethasone exposure in presence or absence of AFSC-EVs. Image length: 100µm. Scale bar: 15µm.

(D) Fluorescence intensity of MitoSox^{TM}/ MitoTracker^{TM} recorded after 20, 24, and 28 minutes of Dexamethasone treatment in presence or absence of AFSC-EVs. Graph data are the mean ± SD (n=3). $^{\circ\circ}p$ value < 0.01, $^{***,\circ\circ\circ}p$ value < 0.001.

5.4 Discussion

Despite the complexity of the age-related muscle wasting conditions, including muscle atrophy, oxidative stress has a central role in the disease progression and the reduction in protein synthesis and/or enhanced proteolysis [252]. This work aimed to explore the therapeutic potential of EVs derived from AFSCs, in counteracting the atrophic phenotype and negative consequences on NMJ integrity caused by Dexa exposure.

As already seen, FOXO3 plays a central role regulating both metabolisms and oxidative stress defenses in Dexa-induced catabolic events. Indeed, in our *in vitro* atrophy system, a FOXO3 gene expression increase was observed, accompanied with an overexpression of autophagy-related markers beclin-1 and LC3β. Consequently, the myotube morphology appeared affected, as demonstrated by the reduction of fusion index, nuclei per myotube, and myotube thickness, associated with a down-regulation in markers of late muscle differentiation (myosin heavy chain 1 and 3). On the other hand, we observed an increase in the expression of structural muscle protein Desmin. Desmin is a fundamental intermediate filament necessary for muscle structure maintenance, cellular integrity and size, mitochondrial homeostasis, and proteostasis [253]. Different studies linked the atrophy-related loss of Desmin protein to the ubiquitin-proteasome and autophagy systems [175,254], while recent studies demonstrated an up-regulation of Desmin gene in different heart failure models, as a compensatory mechanism for its increased misfolding and degradation [255–257]. In relation with that, a similar repaying response could be supposed in this Dexa-induced atrophy model. Remarkably, AFSC-EV exposure restored the myotube morphology as well as the gene expression of muscle markers altered by Dexa.

Since the pivotal role of oxidative stress in the progression of muscle atrophy, its implication in our model and the potential of EVs in redox modulation were investigated. Notably, AFSC-EV treatment reduced the ROS levels, increased by Dexa, and induced an up-regulation of SIRT3 and FOXO3 genes, as well as the antioxidant genes SOD1, GPX, PDRX3, and TRXR3. The mitochondrial NAD-dependent histone deacetylase (HDAC) SIRT3 is principally implicated in stress adaptive responses thanks to its capability to inhibit mitochondrial oxidative stress. Furthermore, FOXO family transcription factors are the main SIRT3 targets, which once deacetylated increase their transcriptional activity and reduce their ubiquitination and consequently their degradation [232]. Sirtuins-activated FOXO3 pathway upregulates different FOXO3-dependent mitochondrial antioxidant enzymes including superoxide dismutase, thioredoxin, and peroxiredoxin [258]. Recently, different studies have elected the skeletal muscle as an essential source of signals for neuron survival, axonal growth, and synaptic connection maintenance highlighting the bidirectional communication between nerve and muscle [225]. Based on that, in this work the muscle damage consequences on MN termination and AFSC-EV beneficial effects were also investigated. To focus our investigation on NMJ perturbation during muscle atrophy, we used microfluidic devices to set up an *in vitro* co-culture of human iPSC-MNs and atrophic myotubes. The fluidically isolated compartments, where only neurites can growth through microgrooves, not only allows the maintenance of a cell-type-specific microenvironment, but also the subcellular isolation of compartments, such as axonal distal and proximal parts, to perform region specific analyses [174,259]. The presence of mature myotubes into the muscle side was reduced by Dexa, as expected, but, interestingly, the muscle wasting environment negatively influenced the neurite co-presence and consequently, the NMJ maintenance. Moreover, we observed that both types of NMJs, the mature multiple contact point and newly formed compensatory single contact point, were equally impaired by Dexa. In addition, the presence of AFSC-EVs prevented all these muscle and neuronal alteration, probably protecting MNs from the detrimental environment created into the synaptic space during atrophy-related muscle wasting. Looking into the consequences on functionality, we observed an impairment in the number of active myotubes after MN-stimulation, compared to the total active myotubes, in presence of Dexa. Even though during stimulation the intensity peak of calcium influx didn’t change after Dexa treatment, we observed a delay in myotube response reactivity to MN-stimulation over time in atrophic conditions. Interestingly, AFSC-EV pre-treatment was able to reverse this effect. Notably, different studies on amyotrophic lateral sclerosis (ALS) models showed that among the principal causes of presynaptic transmitter release affection we can found increased oxidative stress and compromised mitochondria [260,261]. In G93A-SOD1 ALS mice model the exposure of diaphragm muscle NMJs to exogenous H_2O_2 induced a strong inhibition of spontaneous neurotransmitter release. Considering this, we propose that the observed alterations in myotube contraction timing could be explained as an impairment in the synaptic vesicles’ release by presynaptic terminals affected by an atrophy-related redox imbalance. However, an impairment in myotube contractile machine cannot be excluded. Besides, further studies on mutant SOD1 mouse models showed an oxidative stress increase in distal muscle also before the ALS pathology onset. This interesting finding suggests that the oxidative damage could start at the muscular postsynaptic side and then propagates to MN-presynapse and further up to the axon in a retrograde way towards the neuronal soma, finally causing the apoptosis of the entire cell [262–264]. To evaluate this observation in our model, we decided to investigate the oxidative stress and the attenuating potential of AFSC-EVs during atrophy-related NMJ deterioration. To this purpose, the oxidative stress alterations were followed on that neurites that reach the myotube side, the ones likely creating NMJs. Interestingly, AFSC-EV pre-treatment counteracted the ROS increase as well as the mitochondrial superoxide ($O_2^{\bullet-}$) overproduction in neurites, following atrophy induction. The re-equilibrating effect of EVs on redox unbalance in affected NMJ could be due to the direct effect on ROS scavenging of their cargo in antioxidant proteins, including SOD1. Centrally, increased ROS in the synaptic space are linked to the loss in MN and NMJ integrity and muscle contraction efficiency, and the permanence of this toxic unbalance could finally leads to irreversible damage of structure and activity [265,266]. Altogether, these data suggested a protective effect of AFSC-EVs by the re-equilibration of redox imbalance and their immunomodulatory and neurogenic capability on NMJ and motor neuron injuries induced by muscle atrophy.

Chapter IV – Neurons and microglia in Alzheimer's disease: human AFSC-EVs protective effect against Aβ

6.1 Introduction

6.1.1 Alzheimer's disease: the role of oxidative stress in brain aging

Alzheimer's disease (AD) is the most widespread neurodegenerative disorder, characterized by a progressive damage in neuronal cells which principally leads to impaired cognitive functions [267]. AD is a growing global health issue with huge implications for people's daily lives and society. In the United States it is the sixth leading cause of death [268]. Its pathophysiology is mainly associated with the extracellular deposition of amyloid beta (Aβ) plaques and the accumulation of intracellular neurofibrillary tangles (NFT) [269]. There are different mechanisms underpinned to the neurotoxic action of Aβ, but the crucial one is the high ROS generation associated with the prominent oxidative state. For example, Aβ accumulation can decrease calcium ion storage in the endoplasmic reticulum, resulting in cytosolic Ca^{2+} overload. Consequently, the Ca^{2+} rise leads to a reduction in glutathione (GSH) levels and then, a cellular ROS overaccumulation [270]. Moreover, Aβ can activate the NADPH oxidase, directly leading to free radical formation [271]. The oxidative stress caused by Aβ is also due to the formation of complex with redox active metals, such as copper, zinc, and iron that bind Aβ promoting plaque aggregation. This metal-amyloid complex oxidative stress can cause excitotoxicity, stimulate membrane depolarization, and impairs mitochondrial functions [272,273]. Dysfunctional mitochondria are also implicated in AD pathogenesis and are mainly characterized by functional alterations, increased ROS generation, affected mitochondrial numbers and morphology (small and fragmented) [274]. Several studies highlighted the presence of Aβ accumulations in mitochondria of brains of AD mouse models and demonstrated its direct interference with the mitochondrial function leading to the metabolic deficiencies and neurological dysfunction characteristic of AD brain patients [275]. On the other hand, according to the mitochondrial cascade hypothesis, the age-related loss of functional mitochondria also affects the metabolism of amyloid precursor protein (APP), producing Aβ toxic oligomers that accumulate into Aβ plaques [276], fueling a vicious cycle.

Interestingly, it has been demonstrated that ROS are implicated in the JNK/stress-activated protein kinase pathways. The activation of these cascades finally leads to the hyperphosphorylation of Tau proteins and to Aβ-mediated cell death [277].

Finally, in the brain, the inflammatory response, mediated by microglia, is activated as a tentative to prevent the aggregation of these toxic proteins, inducing a marked ROS release and subsequent increase in oxidative stress [278,279]. Therefore, a vicious cycle, in which the ROS level increases, seems to be activated. (***Figure 5***).

The exact ROS mechanism of action is not yet completely understood; however, several hypotheses consider them as aggravating players in the disease progression through the imbalance of the redox state [280,281].

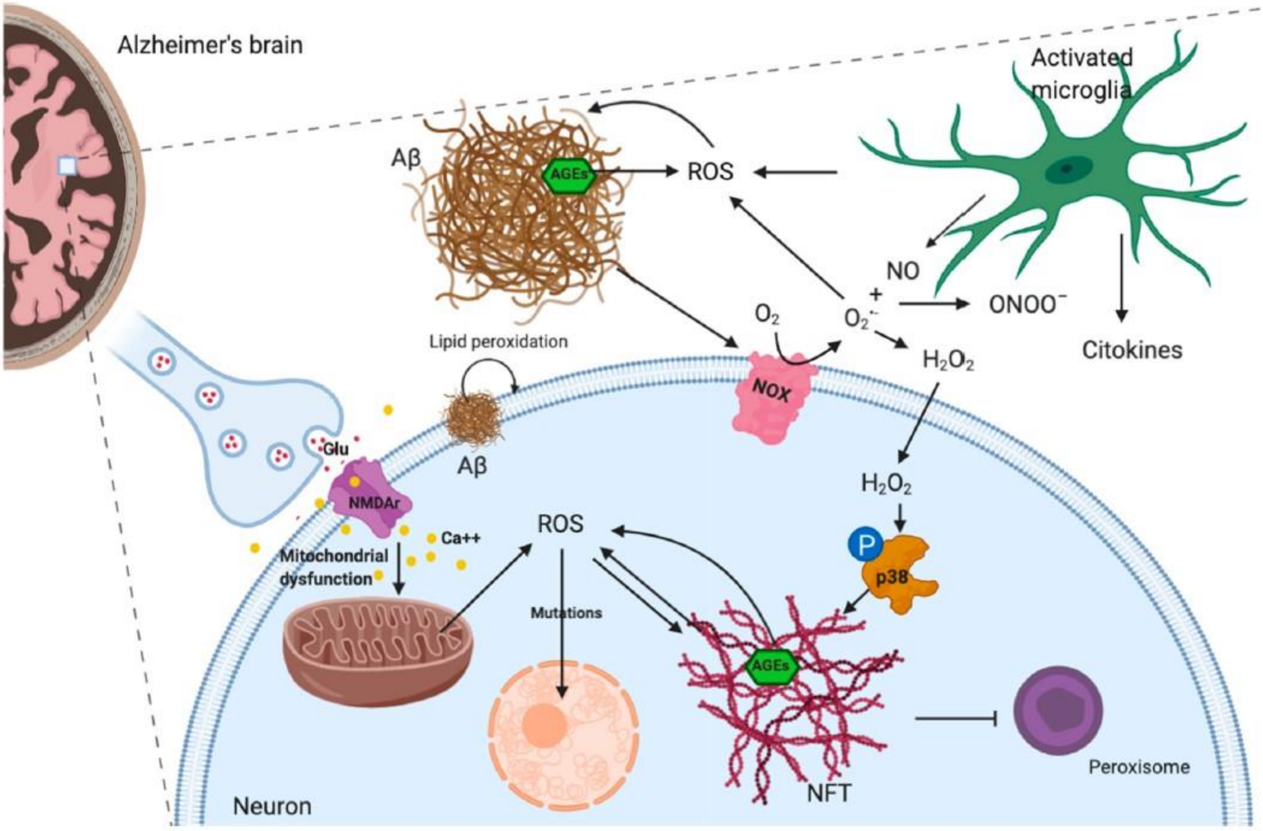

Figure 5: Schematic representation of ROS sources and their molecular targets in AD. Image Created with BioRender.com [282].

6.1.2 Neuroinflammation: the microglial role in neurodegeneration

Microglia are the resident predominant immune cells in the CNS, known to quickly respond to variation in brain homeostasis, due to stress, trauma, or pathologies [278]. They were originally thought to be responsible for regulating the neuroinflammation and thus cause neurodegeneration, but they were also linked to the maintenance of CNS homeostasis, as well as the regulation of synaptic plasticity, learning and memory mechanisms [283]. Exploring the implication of microglia in AD onset and progression, several roles can be attributed to these immune cells. Indeed, microglial cells are strictly linked to neuroinflammation, Aβ accumulation, Tau pathology, and neuronal and synaptic loss, but they also actively participate in the neuroprotection, especially through the phagocytic clearance of Aβ [278].

In AD pathology, Aβ aggregates can stimulate the Toll-like receptors on microglial cells activating the inflammasome complex. As a consequence, caspase1 is recruited and several pro-inflammatory mediators, namely TNFα and IL1β, are released to stimulate further pro-inflammatory response by microglia and other brain immune cells, such as astrocytes [284]. The prolonged inflammatory state that leads to an overproduction of inflammatory cytokines, and nitric oxide (NO) that in presence of ROS generates $ONOO^-$ and other reactive nitrogen species (NOS), that are crucial contributors to oxidative stress in AD [285].

Furthermore, a recent study demonstrated that microglia could increase the Aβ oligomers formation and stimulate their aggregation due to the high affinity binding of Aβ to ASC (adapter protein apoptosis associated speck-like protein) complex released by microglial cells. This evidence suggests a direct implication of microglial inflammasome in spreading the Aβ pathology in AD patients [286].

Moreover, the microglia activation seems to exacerbate Tau pathology in AD mouse models, *via* mechanisms still not clear. In an *in vitro* mouse model of AD with mutant Tau, microglia have been linked to the cell-to-cell spread of Tau pathology across the brain, probably *via* microglial uptake and exosomal release of Tau protein [287].

As mentioned before, several pieces of evidence suggest a heterogeneous role of activated microglia in the CNS, which can be classified into two opposite types: M1 and M2 phenotypes. Microglial cells can exert both neurotoxic and neuroprotective effects, depending on the activated phenotype. Overall, M1 microglia predominate at the injured site in the final disease stage, when the immuno-resolutive and regenerative tentative of M2 one is reduced. This phenotype switch is very complicated in AD, given the precarious balance between resolution tentative and cytotoxicity. Moreover, the endogenous stimuli, namely mutated superoxide dismutase, Aβ, Tau and α-synuclein aggregates, may exert a persistent activation of M1 pro-inflammatory response, which finally leads to an irreversible neuronal damage. Based on that, the stage and severity of AD have been strictly linked to the transition between the two microglial phenotypes [288].

So, this microglial double-edged sword of function in AD complicates the therapeutic approach that targets these immune cells. Indeed, the stimulation of microglia may be helpful in the early phases, preventing AD onset, but it could be detrimental in the subsequent phases, when the disease has reached a highly inflamed and neurotoxic state [287].

6.1.3 Application of MSCs and their secretome in AD

MSCs, and MSC-EVs as well, have been proposed as therapeutic approaches to counteract several neurodegenerative disease, including AD. Considering the MSC-EV promising cargo, which includes lipids, proteins, enzymes, and miRNAs endowed with anti-inflammatory, neurotrophic, and Aβ degrading systems, these cells could be a therapeutic strategy combining different effects that can finally leads to the repair of synaptic function, the reduction of neuronal death and the slowdown of memory impairment [289]. In literature there are different studies that demonstrated the beneficial effects of MSC-EVs in reducing the AD features in several AD *in vitro* and *in vivo* models (***Figure 6***).

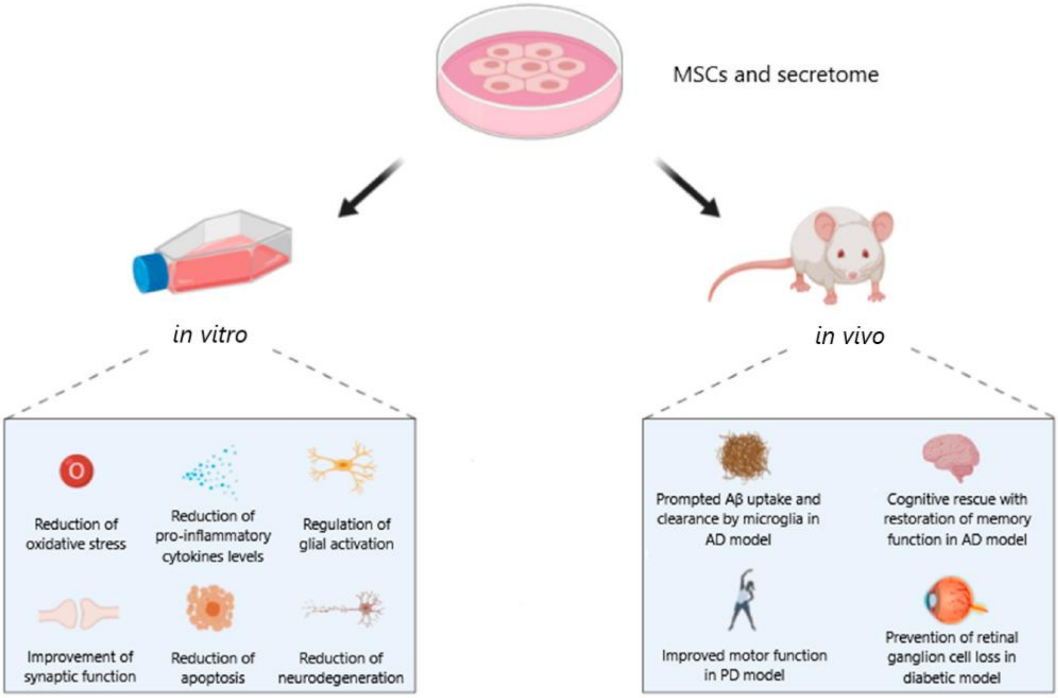

Figure 6: Schematic representation of the demonstrated effects of MSCs in counteracting neurodegeneration *in vitro* and *in vivo*. Image Created with BioRender.com [282].

Initially, the MSC-EV potential was investigated by treating a cellular model of AD with EVs obtained from adipose tissue MSCs. Interestingly, the vesicles administration reduced both secreted and intracellular Aβ levels [290]. Later, de Godoy and colleagues co-cultured, using a transwell system, rat neurons, exposed to soluble oligomers of Aβ, with MSCs. They observed an increase in Aβ oligo internalization and degradation, in the release of EVs enriched in active catalase, and specific secretion of IL6, IL10, and vascular endothelial growth factor into the medium [192].

Moreover, the positive action of MSCs against neurodegeneration was also confirmed by the observation of the inhibitory effect on oxidative stress and pro-inflammatory mediator release, operating not only on neuronal cells but also on microglia. Indeed, it has been found that human bone marrow MSCs are able to significantly reduce the lipopolysaccharide (LPS) activation of microglial cells *in vitro* [291]. The potential of MSC treatment to ameliorate Aβ pathology and to modulate oxidative stress *via* microglia regulation was recently demonstrated by Yokokawa et al. [292] *in vitro*, co-culturing a mouse microglial cell line with MSCs, and *in vivo* as well, using an AD mouse model. Indeed, MSCs promoted the microglial phenotype switch from M1 to M2 and diminished the secretion of pro-inflammatory cytokines. Furthermore, the MSC transplantation stimulated the accumulation of these immune cells around the Aβ deposits, triggering its uptake and elimination. In addition, MSCs injected into the tail vein reduced the Aβ deposition in the cortex and hippocampus, leading to ameliorated spatial memory abilities. Based on this evidence, it has been supposed that the neuronal positive effect of MSCs is, at least in part, due to the release of neurotrophic factors and the maintenance of redox balance, that together preserve the neuronal functions [293]. Moreover, the MSC secretome, which includes the soluble part as well as EVs, can preserve hippocampal neurons from pro-oxidative stimuli and avoid the synapse loss mediated by Aβ. This interesting finding was demonstrated by using the secretome derived from human Wharton's jelly MSCs, in a study of Bodart-Santos and colleagues [294].

So, these observations highlight that the interplay between neurons and microglia, which generate a deleterious vicious cycle, could be a potential target to counteract the AD pathogenesis and progression.

6.2 Materials and Methods

6.2.1 Animals

5xFAD mice co-overexpress a triple-mutant human amyloid precursor protein (APP) (Swedish mutation: K670N, M671L; Florida mutation: I716V; London mutation: V717I) and a double-mutant human presenilin 1 (PS1) (M146L and L286V mutations) transgenes under the transcriptional control of the neuron specific Thy-1 promotor. Progenitors were purchased from Jackson Laboratories, Bar Harbor, and 5xFAD line was maintained by crossing hemizygous 5xFAD mice with B6SJL/J breeder. Mice were kept in conditioned rooms with stable temperature (22 ± 1°C) and humidity (60%), on a light/dark cycle of 12 hours, with food and water ad libitum. All animal procedures were approved by the Committee on Animal Health and Care of the University of Modena and Reggio Emilia (protocol number: 974/2016-PR del 13-10-2016) and conducted in accordance with National Institutes of Health guidelines. For genotyping procedure, APP and PS1 lines were analyzed as previously reported [295]. Tail samples from WT and 5xFAD mice were examined by using primers supplied by Jackson Laboratories to identify either the mutation or the wild-type allele with the polymerase chain reaction (PCR): forward, 5′-AGGACTGACCACTCGACCAG-3′ and reverse, 5′-CGGGGGTCT AGTTCTGCAT-3′ for APP transgenes; forward, 5′-CTAGGCCACAGAATTGAAAGATCT-3′ and reverse 5′-GTAGGTGGAAATTCTAGCATCA-TCC-3′ for positive control; forward, 5′-AAT AGA GAA CGG CAG GAG CA-3′ and reverse 5′-GCC ATG AGG GCA CTA ATC AT-3′ for hPRES transgene. DNA was polymerized at 94°C for 3min; 35 cycles of 94 ° C for 15 s; 54°C for 1min; 72°C for 1min; and 72 ° C for 2min; stored at 4°C. The PCR products were run on a 1% agarose gel, using ethidium bromide ultraviolet (UV) detection for the bands at 377 bp (APP transgene) or 324 bp (positive control) and 608 bp (hPRES).

6.2.2 Preparation of primary cultured cortical neurons and AFSC-EVs treatment

Cortical and hippocampal neurons from wild type (WT) (N = 18) and 5xFAD (FAD) (N = 25) mice were collected within 24 h from birth [296]. Brains were removed, meninges were gently peel off, and cortical and hippocampal tissue dissected. Tissues were incubated in a buffer solution containing HBSS (Hanks' Balanced Salt Solution) (GIBCO, Thermo Fisher Scientific, Milan, Italy) with BSA 0.3% (Microgem Srl, Naples, Italy) and trypsin 0.025% (EuroClone, Milan, Italy) at 37°C for 15 min. Then, tissues were triturated with a plastic

1000 μl pipette tip in a HBSS buffer containing 0.004% deoxyribonuclease I (DNAseI) (Sigma Aldrich, Milan, Italy) and 10% fetal bovine serum (FBS) (Microgem Srl, Naples, Italy). After centrifugation at 500 g for 5 min, cells were suspended in Neurobasal medium supplemented with 2% B27 (GIBCO, Thermo Fisher Scientific, Milan, Italy), 2mM glutamine, 100U/ml penicillin and, 100 μg/ml streptomycin (EuroClone, Milan, Italy) and plated on poly-L-lysine (Merck Millipore, Milan, Italy) coated plastic or coverslips at 5 x 10^5 cells/cm^2. Cells were maintained at 37°C and 5% CO_2. After 48 h, cells were treated with 5 μM cytosine β-D-arabinofuranoside (Sigma Aldrich, Milan, Italy) for 24 h. For *in vitro* experiments, 10 μg of extracellular vesicles, obtained from the two human samples of hAFSCs by Total Exosomes Isolation Kit (Invitrogen, Life Technologies, CA, USA), resuspended in PBS, were added to 1 x 10^6 cells at DIV (days *in vitro*) 3 for 7 up to 14 days. Wortmannin (Sigma Aldrich, Milan, Italy) treatment was performed for 2 h prior the EV exposure.

6.2.3 Cell line cultures and treatments

The SH-SY5Y cell line was purchased from Sigma-Aldrich (ECACC 94030304) (St. Louis, MO, USA) and was grown in high-glucose DMEM supplemented with 10% FBS, 2 mM L-glutamine, 50 U/mL penicillin and 50 μg/mL streptomycin, as previously reported [142]. The cells were used for experiments after inducing their differentiation with 10 μM all-trans retinoic acid (RA) for 7 days. Differentiated SH-SY5Y cells were treated for 24 h with 10 μM $A\beta_{1\text{–}42}$ fibrils (GenScript, Piscataway, NJ, USA) obtained after incubation at 37° C for 24 h. BV2 murine microglial cells were a kind gift of Prof. Elisabetta Blasi (University of Modena and Reggio Emilia, Modena, Italy). The cells were cultured in RPMI supplemented with 10% low-endotoxin FBS (Euroclone, Milano, Italy), 2 mM L-glutamine, 50 U/mL penicillin and 50 μg/mL streptomycin. The cells were maintained in a humidified incubator at 37 °C with 5% CO_2 and detached by vigorous shaking. The BV2 cells were pretreated with 0.5 x 10^9 EVs/10^6 cells for 4 h before the addition of 1 μg/mL lipopolysaccharide (LPS) for 24 h. For experiments with the BV2-conditioned medium (BV2-CM), SH-SY5Y cells were plated (4 x 10^4 cells/cm^2) on 6-well plates. After the differentiation procedure described above, the medium was replaced with a CM for 24 h. Transwells are a well-characterized 3D model of a co-culture and have been used extensively for neuronal co-cultures including SH-SY5Y and BV2. BV2 cells were plated (4 x 10^4 cells/cm^2) on top of the transwell inserts in an RPMI medium w/o FBS. After the treatments with extracellular vesicles and LPS as previously described, the transwell inserts (BioBasic Inc., Toronto, Canada) were placed on top of the 24-well containing SH-SY5Y (4×10^4 cells/ cm^2) in a medium containing 50% RPMI and 50% DMEM. See ***Figure IV.6*** below for a diagram of the treatment. The cells were treated with 10 µM $A\beta_{1-42}$ for 24 h.

6.2.4 MTT assay

Cells (primary neurons, SH-SY5Y and BV2) were seeded in 96-well plate in 200 µl of culture medium, 4 replicates for each condition, at a density of 5×10^5 cells/cm^2 for FAD neurons, while $3{,}3 \times 10^4$ cells/cm^2 for SH-SY5Y and BV2 cells. At the end of each experiment, MTT assay was performed as previously described (*Section 4.2.2*).

6.2.5 ROS and Glutathione detection

FAD primary neurons, SH-SY5Y, and BV2 cells were seeded in a black 96-well plate, 4 replicated for each condition, at a density of $3{,}3 \times 10^4$ cells/cm^2. To measure intracellular ROS content, dichlorodihydrofluorescein diacetate (DCFH-DA) assay was performed similarly to as previously described in *Section 4.2.3*.

Similarly, reduced GSH levels, into primary neurons, were evaluated using monochlorobimane (MCB) (Sigma-Aldrich, Milan, Italy) assay (previously described in *Section 4.2.3).*

6.2.6 NO detection

Nitrogen species (NO) production, index of BV2 cell activation, was measured by Griess assay (Sigma Aldrich, Milan, Italy). Supernatants and Griess reagent were mixed 1:1 into a 96-well plate and after 10 minutes the samples were analyzed by a spectrophotometer at 546 nm. The NO production was expressed in µM.

6.2.7 Cellular extract preparation

Total cell lysates (TL) were obtained as previously described (*Section 4.2.4*). Briefly, at the end of experiments cellular pellets were treated with lysis buffer, added with a protease inhibitor cocktail and para-nitrophenylphosphate (both from Sigma Aldrich, Milan, Italy), at 4°C for 20 min. The lysates were sonicated, cleared by centrifugation, and immediately boiled in SDS, reducing sample buffer.

6.2.8 SDS Page and Western Blot

The TL, from 5xFAD, SH-SY5Y and BV2 cells, were processed as previously described (*Section 4.2.7*). Primary antibodies used are against the following molecules: actin, Nox4 (Sigma-Aldrich, St Louis, MO, USA), total-Akt, SOD1, SIRT1, gp91phox, TrxR1, TrxR2, Gpx1, MAP LC3β, PARP, TIA-1 (Santa Cruz Biotechnology, CA, USA), pAkt^{ser473} (Cell Signaling Technology, MA, USA), β- Amyloid clone 6E10 (Bio Legend, CA, USA), pTau^{ser422} (Ori-Gene Technologies, MD, USA), Bcl-2 (Bio Source, CA, USA), caspase7, IL1R1 (Santa Cruz Biotechnology, CA, USA), TGFβ, CD86 (Novus Biologicals, Milano, Italy), and βTubIII (Cell Signaling Technology, Lieden, The Netherlands). Secondary antibodies (Thermo Fisher Scientific, Waltham, MA, USA) were used at 1:3000 dilution.

6.2.9 ELISA assay for Aβ quantification

Secreted amyloid beta peptide 1-42 (Aβ_{1-42}) was analyzed in the supernatants of primary cortical neurons and SH-SY5Y cells by BETA-APP42 ELISA Kit (Human) (Aviva Systems Biology, San Diego, CA, USA) according to manufacturer's protocol. Medium from 5xFAD cells (5×10^5 cells/cm^2) treated with AFSC-EVs for 7 days and untreated control were collected and then centrifuged at 300 x *g* for 10 minutes at RT for 10 minutes to remove cellular debris. Supernatants were concentrated about 10 times by lyophilization with LIO5P (5Pascal, Milan, Italy) [297]. Freeze-dried powder obtained from 6 ml of medium exposed to neurons was rehydrated with 600 µl of purified water and stored at 4°C until analysis. Concentrated supernatants were used for ELISA assay. Indeed, media from SH-SY5Y and BV2 co-culture transwell system, exposed or not to EVs, were collected and stored at 4°C before ELISA assay.

6.2.10 Immunofluorescence and confocal microscopy

For immunofluorescence analysis, primary FAD neurons and SH-SY5Y cells seeded on coated coverslip were processed as previously described in *Section 4.2.8*. Primary antibodies were raised against the following molecules: βTubIII (Millipore, CA, USA), pTau^{ser422} (OriGene Technologies, MD, USA), 6E10 (Bio Legend, CA, USA), and MAP2 (Cell Signaling Technology, MA, USA). Alexa secondary antibodies (Thermo Fisher Scientific, Waltham, MA, USA) were used at 1:200 dilutions. The confocal serial sections were processed with ImageJ software to obtain three-dimensional projections. The image rendering was performed by Adobe Photoshop software.

For apoptosis detection, FAD neurons were washed three times with 50 µl of binding buffer (10 mM HEPES, pH 7.5, containing 140 mM NaCl, and 2.5 mM $CaCl_2$), and then incubated for 15 minutes with 50 µl of double staining solution (binding buffer containing 25 µl of annexin V-FITCH and 0.25 µl of propidium iodide (PI)) (BD Pharmingen^{TM}, Erembodegem, Belgium). Lastly, samples were washed 5 times with 50 µl of binding buffer, mounted with 15 µl of binding buffer, and visualized under fluorescence microscopy [83] .

6.2.11 Cellular morphology analysis

Cellular images were acquired using an EVOS XL Core Cell Imaging System (Thermo Fisher Scientific, Vantaa, Finland) as previously described [295]. The parameters and area were measured with ImageJ. The cellular elongation was calculated using the following formula:

$$\text{Cellular elongation} = 2p/4\pi \times A$$

Where p is the cellular perimeter, π is equivalent to 3.14 and A represents the cellular area.

6.2.12 Statistical analysis

All the experiments were performed in 3 biological replicates. For quantitative comparisons, the values were reported as the mean ± SD based on a triplicate analysis for each sample. One-way ANOVA with Bonferroni post hoc test or a Student's *t*-test were applied to test the significance of the observed differences amongst the study groups. Statistically significant was considered a p-value < 0.05. Statistical analysis and plot layout were obtained by using GraphPad Prism® release 8.0 software.

6.3 Results

6.3.1 AFSC-EV effect on morphological alteration of FAD primary neurons

First, FAD neurons appeared unhealthy compared to wild type ones. It could be due to the prominent neurodegeneration characteristic of AD neurons, as suggested by shrunken nuclear envelope (***Figure IV.1A***) and neurite deterioration (***Figure IV.1B***, upper), confirmed by neurite number, length, and diameter analyses (***Figure IV.1B***, lower). 14 days AFSC-EV treatment counteracted the nuclear envelope impairment and neurite loss since neurite measurements were brought back similar to healthy WT ones.

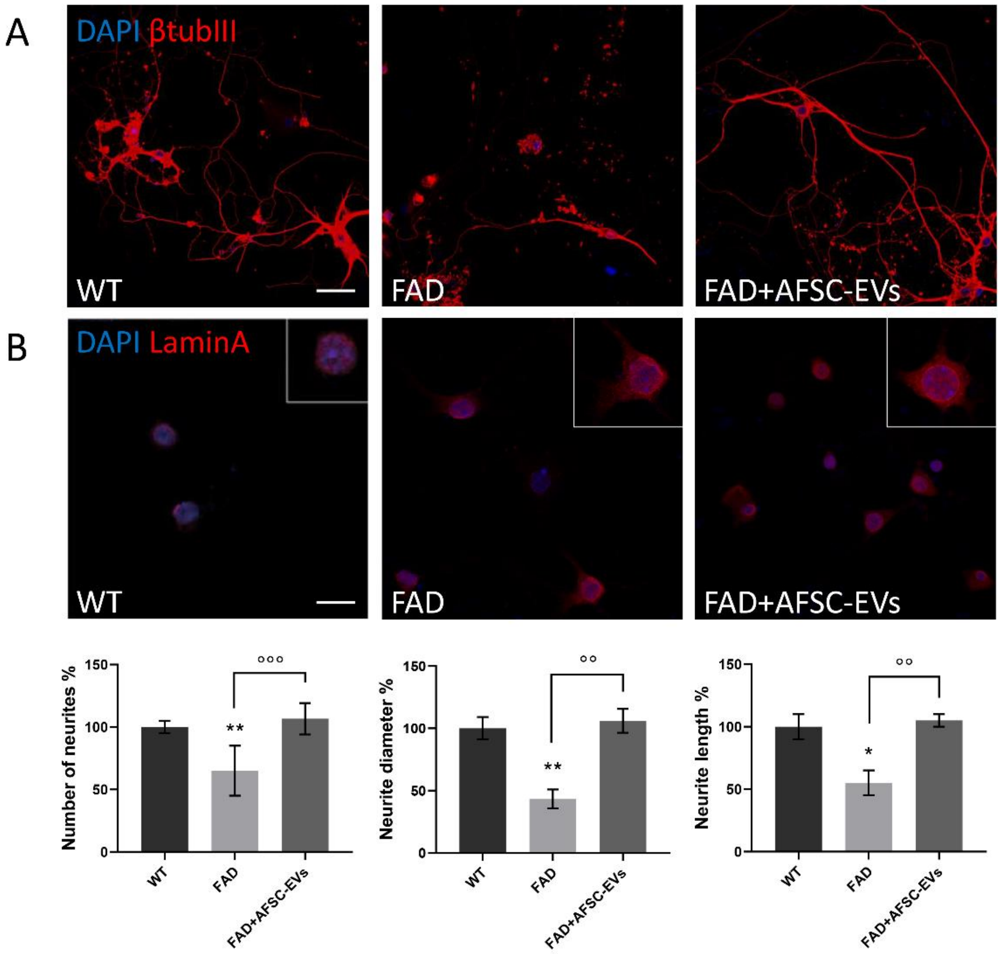

Figure IV.1. FAD neurons morphology after AFSC-EV treatment

(A) Representative confocal images of WT and FAD neurons in presence or absence of 14 days AFSC-EV treatment, stained with Lamin A (red) and DAPI (blue) for nuclei. Insets: magnification of nuclei. Scale bar: 10 µm.

(B) Representative confocal images of WT and FAD neurons in presence or absence of 14 days AFSC-EV treatment, stained with β-tubulinIII (βtubIII) (red) and DAPI (blue) for nuclei.

Scale bar: 10 µm. Graphs relative to analysis of neurite number, length, and diameter. Graph data are the mean ± SD (n=3). *p value < 0.05, **$^{,°°}p$ value < 0.01, °°°p value < 0.001.

6.3.2 Oxidative stress pathway modulation by AFSC-EVs in FAD neurons

ROS content analysis revealed increased levels in FAD neurons compared to WT, as expected (***Figure IV.2A***). On the other hand, we observed a reduction, even if not significant, in GSH content in FAD cells (***Figure IV.2B***). Interestingly, AFSC-EV exposure reduced the ROS content, while allowing the increase in GSH level (***Figures IV.2A*** and ***IV.2B***).

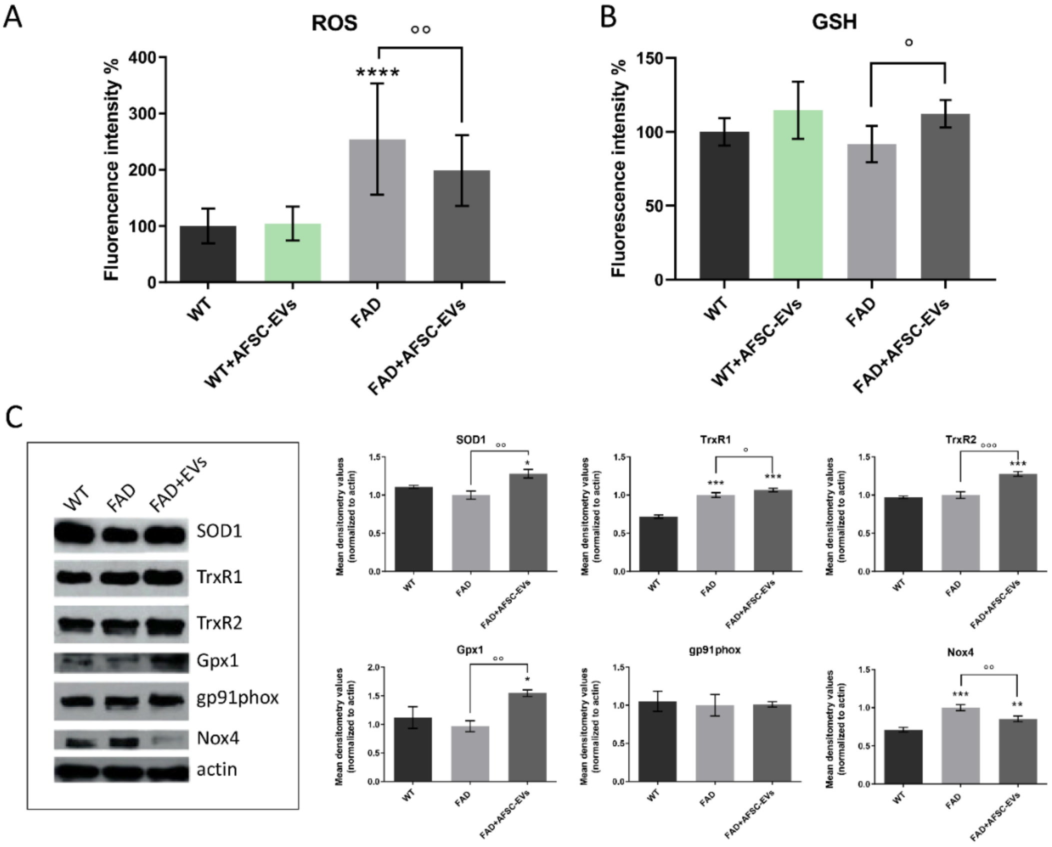

Figure IV.2. Effect of AFSC-EV exposure on oxidative stress modulation in FAD primary neurons

(A) Graph shows ROS content in primary WT and FAD neurons after 14 days of AFSC-EV treatment or not. Graph data are the mean ± SD (n=4). °°p value < 0.01, ****p value < 0.0001.

(B) Graph shows GSH content in primary WT and FAD neurons after 14 days of AFSC-EV treatment or not. Graph data are the mean ± SD (n=4). °p value < 0.05.

(C) Representative images of WB analysis of WT and FAD total lysates treated or not with EVs, revealing the indicated protein levels. The graphs represent the mean ± SD of densitometric analysis (n=3) normalized to actin values. $*, ^{\circ}p$ value < 0.05, $**, ^{\circ\circ}p$ value < 0.01, $***, ^{\circ\circ\circ}p$ value < 0.001.

Then we explored the expression alteration in ROS modulation-related protein through western blot. Antioxidant enzymes superoxide dismutase (SOD1), thioredoxin reductases 1 and 2 (TrxR1 and TrxR2), and glutathione peroxidase 1 (Gpx1) appeared all increased in EV treated FAD neurons, compared to untreated ones (***Figure IV.2C***). However, apart from TrxR1, the other antioxidant markers did not show differences between FAD and WT neurons. The increase in TrxR1 levels in affected neurons suggested a tentative from intracellular defenses to counteract the ROS rise previously observed. Among the ROS producing enzymes, we found high levels of Nox4 in FAD neurons. The presence of EVs reduced, at least in part, this alteration. Nox4 is constitutively active, so it does not need cytosolic subunits for activation, though they are able to modulate Nox4 activity. Another NADPH oxidase expressed into the brain is Nox2, which has been found not only in phagocytic cells, such as microglia, but also in endothelial and neuronal cells [298]. In this case, no differences were observed for the expression ofgp91phox, the typical Nox2 subunit (***Figure IV.2C***).

6.3.3 Apoptotic and autophagic pathways: effect of AFSC-EVs

Neuronal viability in FAD neurons was significantly reduced after 14 days of cultures than WT neurons (***Figure IV.3A***). Meanwhile, the apoptotic pathway implication was confirmed by annexin V and propidium iodide (PI) assays (***Figure IV.3B***). Interestingly, both cell viability and annexin V/PI staining were brought back similar to WT control by AFSC-EVs administration (***Figures IV.3A*** and ***IV.3B***).

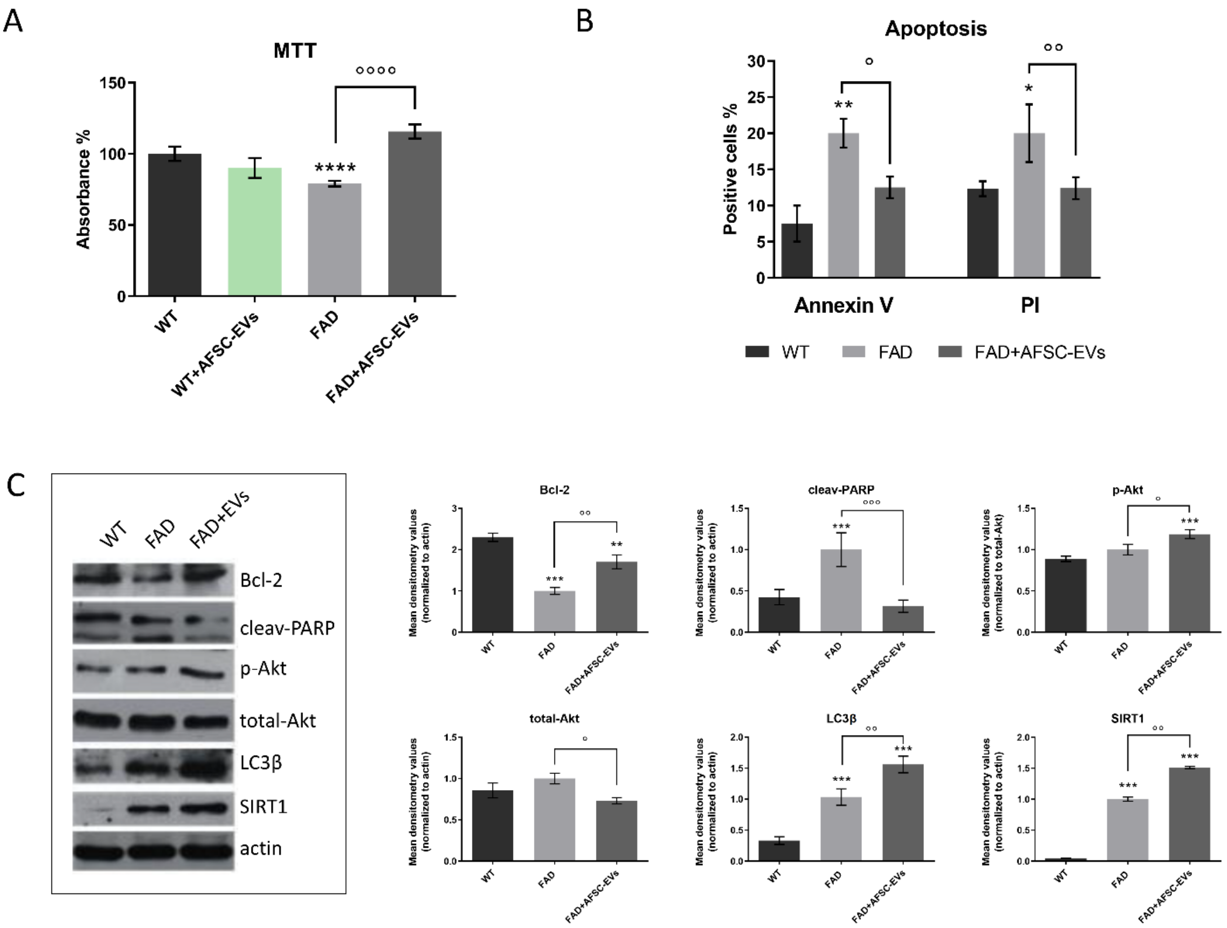

Figure IV.3. Effect of AFSC-EV treatment on apoptotic and autophagic pathways in FAD primary neurons

(A) Graph shows MTT assay of primary WT and FAD neurons after 14 days of AFSC-EV treatment or not. Graph data are the mean ± SD (n=4). $^{****,\circ\circ\circ\circ}$*p* value < 0.0001.
(B) Graph shows percentage of positive cells to Annexin V/propidium iodide assay in primary WT and FAD cultures after 14 days of AFSC-EV treatment or not. Graph data are the mean ± SD (n=3). $^{*,\circ}$*p* value < 0.05, $^{**,\circ\circ}$p value <0.01.
(C) Representative images of WB analysis of WT and FAD total lysates treated or not with EVs, revealing the indicated protein levels. The graphs represent the mean ± SD of densitometric analysis (n=3) normalized to actin values. °*p* value < 0.05, °°*p* value < 0.01, $^{***,\circ\circ\circ}$*p* value < 0.001.

In line with these results, EV-treated FAD neurons showed an increase in Akt activation through its phosphorylation, key signaling molecule for neuron survival, accompanied by an increase in the anti-apoptotic marker Bcl-2 (***Figure IV.3C***). In parallel, PARP cleavage, significantly higher in FAD neurons than WT ones, was reduced by AFSC-EV treatment. These results suggested a positive effect of AFSC-EVs in counteracting the apoptotic pathway activation in affected neurons.

Together with apoptosis the autophagic pathway was modulated by AFSC-EVs in this *in vitro* AD model. Indeed, an increase in SIRT1, a NAD-dependent class III histone and nonhistone protein deacetylase, and LC3β protein levels was observed after EVs exposure (***Figure IV.3C***). Both these proteins are autophagy markers, normally altered during AD [299].

6.3.4 AD marker modulation in FAD neurons treated with AFSC-EVs

Finally, the modulation of intracellular AD markers was carried out. To analyze amyloid precursor protein (APP), Aβ oligomers, and other molecules generated from APP cleavage operated by secretase, we used the specific antibody 6E10 [300,301], while anti-Tau phosphorylated in Serine 422 was used to detect Tau pathological epitope and one of the neurofibrillary degeneration markers [302]. Both are neuropathological hallmarks of AD. So, western blot analysis showed that AFSC-EVs were able to reduce the augmented levels of APP, Aβ oligo, and p-Tau^{ser422} (***Figures IV.4B*** and ***IV.4C***).

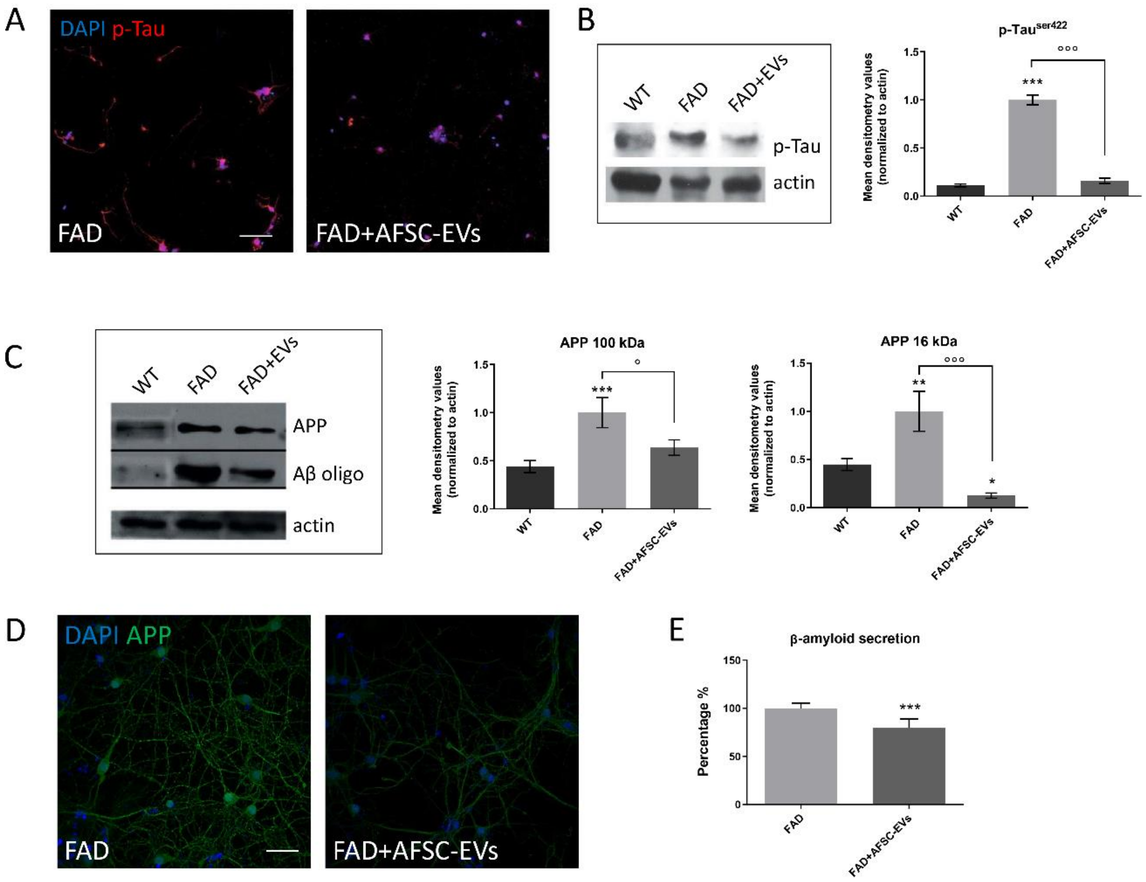

Figure IV.4. Effect of AFSC-EV treatment on AD markers in FAD primary neurons

(A) Representative confocal images of WT and FAD neurons in presence or absence of 14 days AFSC-EV treatment, stained with p-Tau (red) and DAPI (blue) for nuclei. Scale bar: 10 µm.
(B) Representative images of WB analysis of WT, FAD and FAD+EVs total lysates revealed with anti-p-Tau^{ser422} antibody. The graphs represent the mean ± SD of densitometric analysis (n=3) normalized to actin values. $^{***,°°°}$*p* value < 0.001.
(C) Representative images of WB analysis of WT, FAD and FAD+EVs total lysates revealed with 6E10 antibody. APP (100 kDa) and Aβ oligo (16 kDa) bands, with 6E10, are shown. The graphs represent the mean ± SD of densitometric analysis (n=3) normalized to actin values. $^{*,°}$*p* value < 0.05, ***p* value < 0.01, $^{***,°°°}$*p* value < 0.001.
(D) Representative confocal images of WT and FAD neurons in presence or absence of 14 days AFSC-EV treatment, stained with APP (green) and DAPI (blue) for nuclei. Scale bar: 10 µm.
(E) Graph shows percentage variations of secreted β-amyloid in conditioned medium from FAD neurons treated or not with AFSC-EVs analyzed by ELISA assay. Graph data are the mean ± SD (n=4). ****p* value < 0.001.

Moreover, immunofluorescence staining confirmed this positive trend in EV-treated FAD neurons, as shown by ***Figures IV.4A*** and ***IV.4D***.

Finally, the investigation of Aβ secretion demonstrated the positive effect of AFSC-EVs in reducing the release of $A\beta_{42}$, normally increased in FAD neurons (***Figure IV.4E***).

6.3.5 Anti-inflammatory activity of AFSC-EVs on microglia

To investigate the *in vitro* anti-inflammatory activity of AFSC-EVs in this neurodegenerative disease, we decided to use microglial BV2 cells activated by lipopolysaccharide (LPS), a widely used inflammatory mediator for activating microglial cells *in vitro* and initiate the pro-inflammatory signaling cascade [303]. First, typical markers of activated microglia (CD86, IL1R1) were examined by western blot analysis, in order to investigate the EV effect on the macrophagic switch between M1 and M2 phenotypes. Interestingly, ***Figure IV.5*** shows the capability of these vesicles in decreasing M1 marker levels. Among the reactive mediator molecules crucial for the neuroinflammation process, we analyzed NO levels, produced by inducible nitric oxide synthase (iNOS), in LPS-activated BV2 microglial cells treated or not with AFSC-EVs. Notably, the NO production was reduced in activated cells by EVs pre-treatment (***Figure IV.5C***). In parallel, the expression of neuroprotective microglia markers, such as arginase1 and TGFβ, was not affected by AFSC-EVs (***Figures IV.5A*** and ***IV.5B***).

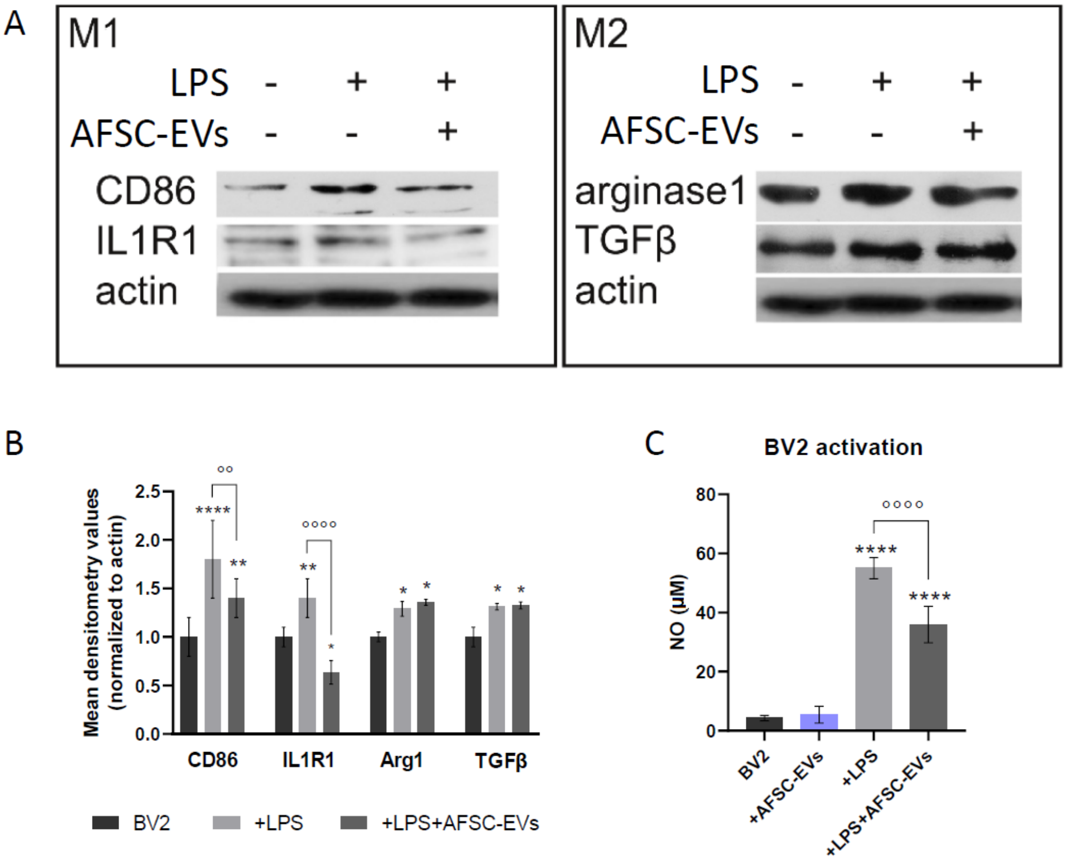

Figure IV.5. Effect of AFSC-EV treatment on LPS-activated BV2 microglial cells.

(A) Representative images of WB analysis of BV2-M1 and M2 phenotype markers in presence or absence of LPS and AFSC-EVs.

(B) The graph represents the mean ± SD of densitometric analysis (n=3) of CD86, IL1R1, Arginase 1 (Arg1), and TGFβ normalized to actin values. **p* value < 0.05, **$^{,\circ\circ}$*p* value < 0.01, ****$^{,\circ\circ\circ\circ}$*p* value < 0.0001.

(C) Graph shows Griess assay of BV2 cells exposed to LPS and/or AFSC-EVs. Graph data are the mean ± SD (n=4). ****$^{,\circ\circ\circ\circ}$*p* value < 0.001.

6.3.6 Protective effect of AFSC-EVs on AD co-culture system

Considering the crucial crosstalk between microglia and neuron cells during AD progression, we decided to set up an *in vitro* co-culture model between BV2 cells and differentiated SH-SY5Y, a neuroblastoma cell line, exposed to Aβ, and then to investigate the eventual AFSC-EV positive effect.

Firstly, we treated SH-SY5Y cells with Aβ in presence of a conditioned medium (CM) obtained from microglial BV2 cells activated by lipopolysaccharide (LPS) (BV2-CM).

Then, the beneficial effect of AFSC-EVs on this system was investigated, as shown in ***Figure IV.6***.

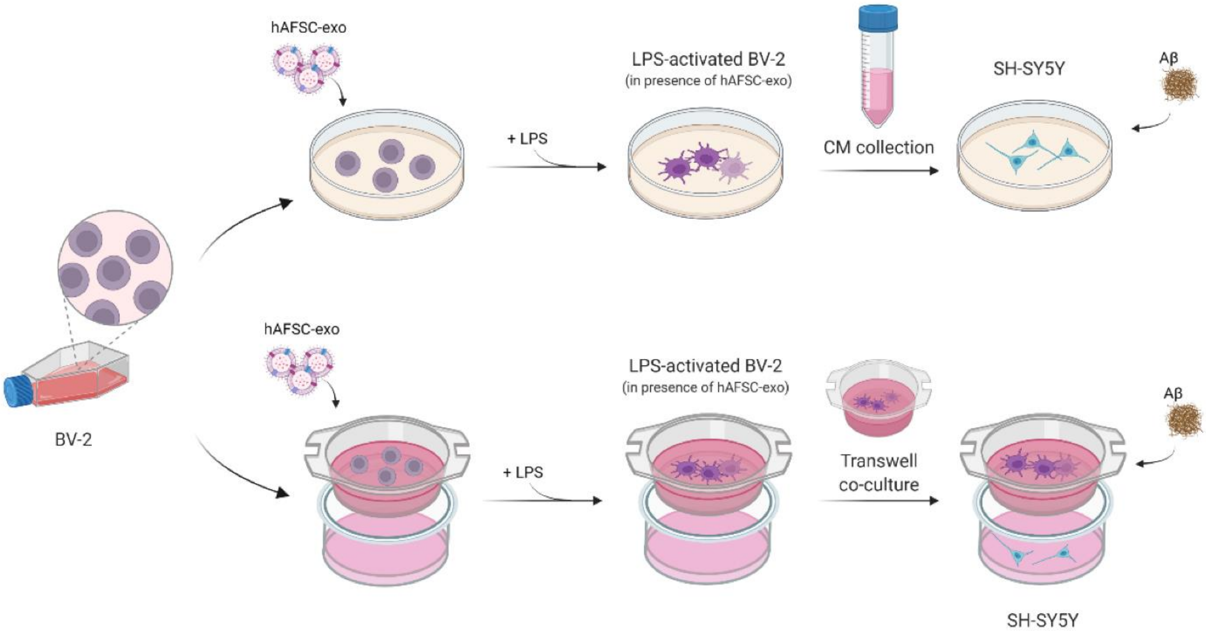

Figure IV.6. Schematic representation of experimental design. SH-SY5Y cells exposed to BV2-CM or to BV2 co-culture in the trans-well system in presence or absence of Aβ and AFSC-EVs. Image elaborated with BioRender.

Notably, SH-SY5Y cell viability was significantly increased by AFSC-EV pre-treatment (***Figure IV.7A***) by reducing the oxidative stress induced by the microglial CM and Aβ (***Figure IV.7B***). Since the cell viability was differently modulated in each condition, the intracellular ROS content was evaluated as a ratio between the probe and fluorescence and MTT absorbance. The oxidative stress increase was accompanied by an activation of the apoptotic pathway: BV2-CM induced the activation of caspase7 and PARP by cleavage, while AFSC-EVs prevent these effects (***Figure IV.7C***).

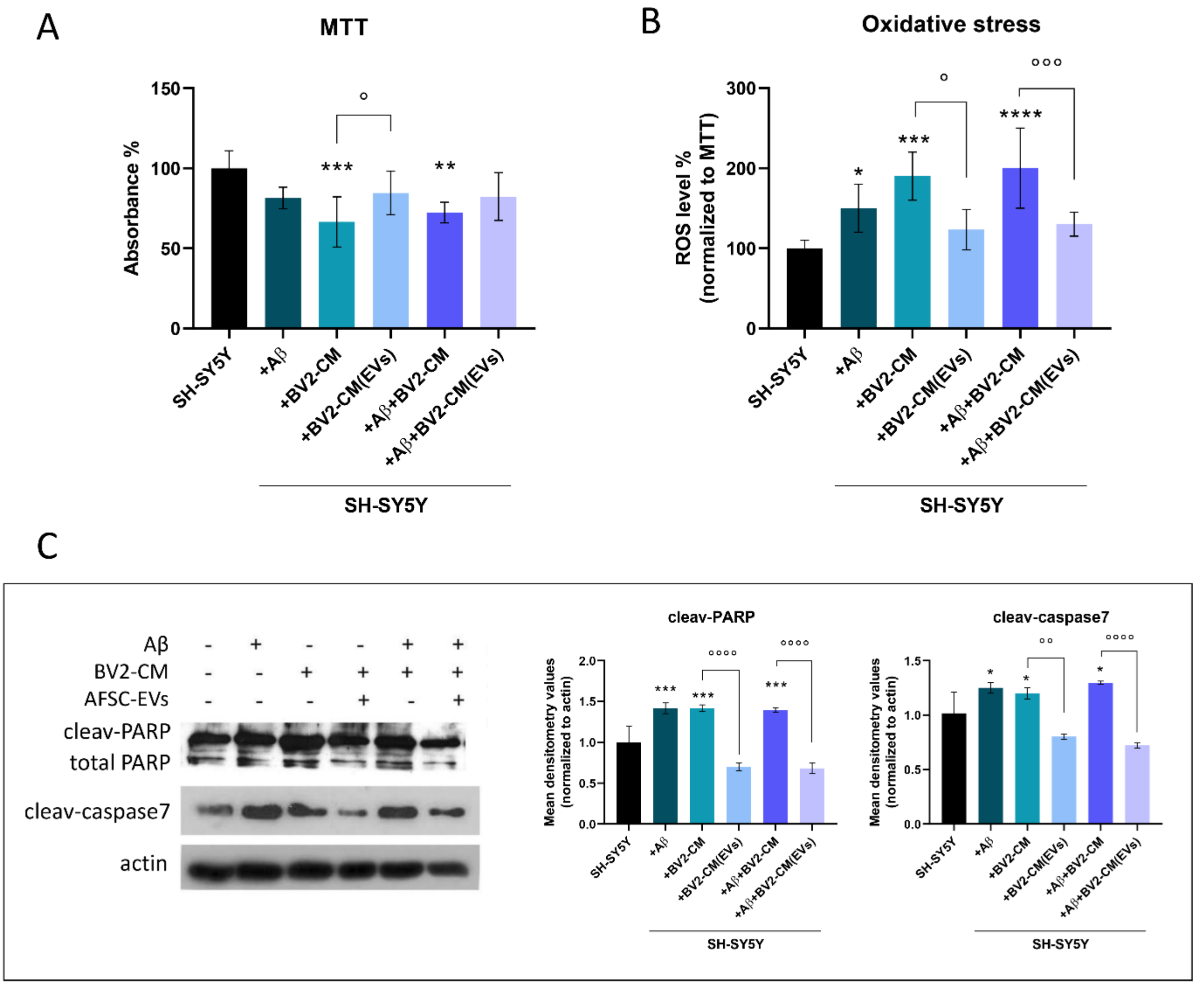

Figure IV.7. Indirect effect of AFSC-EV treatment on SH-SY5Y viability.

(A) Graph shows MTT assay of SH-SY5Y neuron cells exposed to BV2-CM and/or Aβ in presence or absence of AFSC-EVs. Graph data are the mean ± SD (n=4). °*p* value < 0.05, ***p* value < 0.01, ****p* value < 0.001.

(B) Graph shows ROS content normalized to MTT in SH-SY5Y neuron cells exposed to BV2-CM and/or Aβ in presence or absence of AFSC-EVs. Graph data are the mean ± SD (n=4). °,* *p* value < 0.05, °°°*p* value < 0.001, *****p* value < 0.0001.

(C) Representative images of WB analysis of total lysates of SH-SY5Y exposed to BV2-CM pre-treated or not with AFSC-EVs revealed with anti-PARP and cleav-caspase7 antibodies. The graphs represent the mean ± SD of densitometric analysis (n=3) normalized to actin values. **p* value < 0.05, °°*p* value < 0.01, ****p* value < 0.001, °°°°*p* value < 0.0001.

Then, the neuron morphology and the potential of EVs in counteracting the neurodegeneration induced by microglial activation were investigated though immunofluorescence assays (***Figure IV.8A***). Neurites of SH-SY5Y cells exposed to Aβ and BV2-CM treatments, together or alone, were affected. Interestingly, AFSC-EVs pretreatment on microglial cells reduced this alteration, as shown by the analysis of neurite length and thickness (***Figure IV.8B***). Moreover, a similar trend was observed for the protein expression of MAP2, typical markers of mature neurons (***Figure IV.8C***).

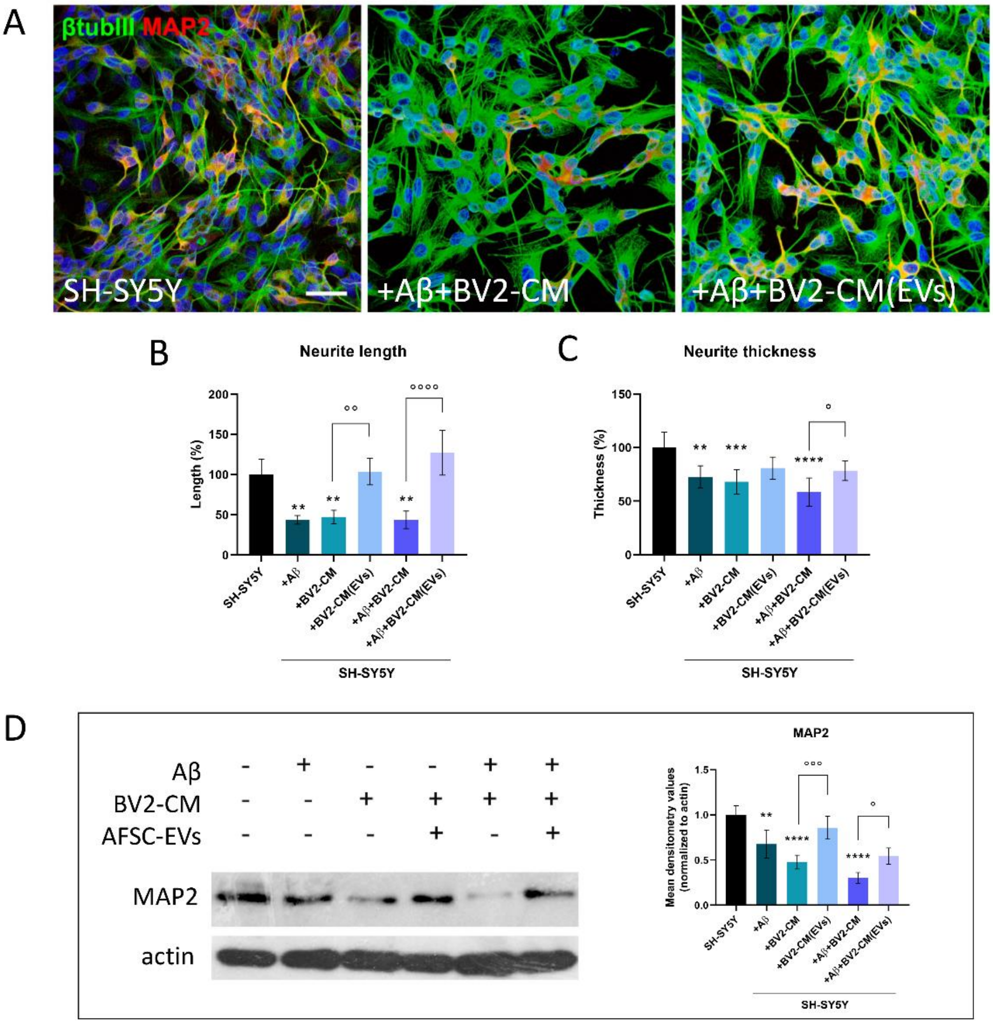

Figure IV.8. Indirect effect of AFSC-EV treatment on SH-SY5Y morphology.

(A) Representative confocal images of SH-SY5Y neurons treated with Aβ and/or CM with or without AFSC-EV pre-treatment, stained with β-TubIII (green), MAP2 (red) and DAPI (blue) for nuclei. Scale bar: 20 µm.

(B) Graphs show neurite length and thickness measured in SH-SY5Y considering β-TubIII staining. Graph data are the mean ± SD (Biological replicates=3). °*p* value < 0.05, **,°°*p* value < 0.01, ***p value < 0.001, ****,°°°°*p* value < 0.0001.

(C) Representative images of WB analysis of total lysates of SH-SY5Y exposed to Aβ and/or BV2-CM pre-treated or not with AFSC-EVs revealed with anti-MAP2 antibody. The graph represents the mean ± SD of densitometric analysis (n=3) normalized to actin values. °*p* value < 0.05, ***p* value < 0.01, °°°*p* value < 0.001, *****p* value < 0.0001.

To explore the efficacy of AFSC-EVs in a more dynamic system, we set up a transwell co-culture system between SH-SY5Y on the bottom side and activated BV2 cells on the top, as previously shown in ***Figure IV.6***. Aβ treatment and LPS-activated BV2 cells, alone or together, induced a ROS increase linked to a decrease in cell viability, as expected. Interestingly, the co-culture with non-activated microglial cells increased SH-SY5Y viability, and for this reason we considered this condition as the real control point (***Figure IV.9A***). Moreover, EVs presence counteracted the ROS rise, thus avoiding cell death (***Figures IV.9A*** and ***IV.9B***), supporting the results previously obtained from the BV2-CM exposure (***Figures IV.7A*** and ***IV.7B***).

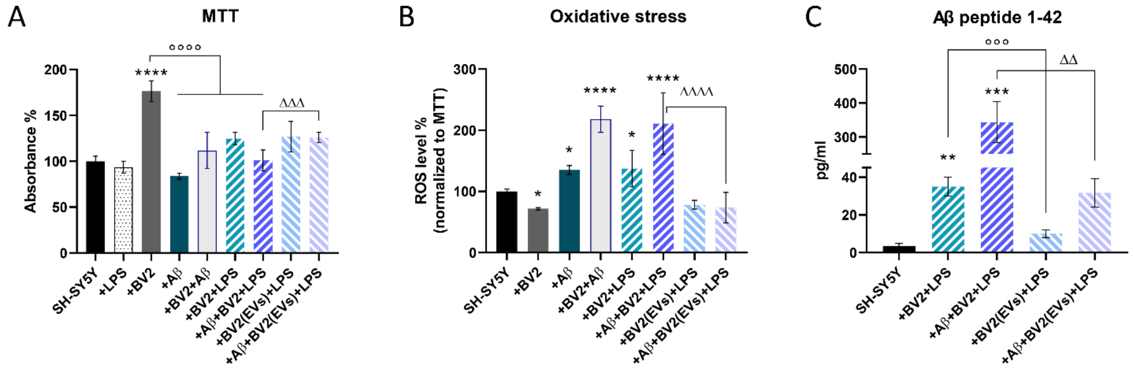

Figure IV.9. Effect of AFSC-EV treatment on SH-SY5Y and BV2 transwell co-culture.

(A) Graph shows MTT assay of SH-SY5Y neuron cells exposed to BV2 (±LPS) and/or Aβ in presence or absence of AFSC-EVs. Graph data are the mean ± SD (n=4). $^{\Delta\Delta\Delta}p$ value < 0.001, $^{****,\circ\circ\circ\circ}p$ value < 0.0001.

(B) Graph shows ROS content normalized to MTT in SH-SY5Y neuron cells exposed to BV2 (±LPS) and/or Aβ in presence or absence of AFSC-EVs. Graph data are the mean ± SD (n=4). * p value < 0.05, $^{****,\Delta\Delta\Delta\Delta}p$ value < 0.0001.

(C) Graph shows ELISA assay of Aβ concentration in conditioned medium obtained from SH-SY5Y and BV2 co-culture transwell treated or not with LPS, Aβ in presence or absence of AFSC-EVs. The graph represents the mean ± SD of densitometric analysis (n=4). $^{**,\Delta\Delta}p$ value < 0.01, $^{***,\circ\circ\circ}p$ value < 0.001.

Finally, the analysis of amyloid β peptide 1-42 ($A\beta_{42}$) was performed on the supernatants deriving from the co-culture. The highest value was obtained in the co-treatment condition (activated BV2 cells and exogenous Aβ, but notably also the only presence of activated BV2 cells induced a clear $A\beta_{42}$ detection. AFSC-EV presence dramatically reduced the presence of Aβ (***Figure IV.9C***), suggesting a promotion of its clearance.

6.4 Discussion

Alzheimer's disease is a progressive neurodegenerative disease, which significantly affects motor and/or cognitive functions. It is characterized by neuronal loss principally caused by an abnormal accumulation of Aβ aggregates, that leads to an increase of environmental oxidative stress and neuroinflammation. Since the increase in endogenous oxidative stress and inflammation, mediated by microglia activation, may be a central factor inducing the AD-related neuronal loss [304–306], here we investigated the beneficial effects of AFSC-derived extracellular vesicles in an *in vitro* model of AD, which includes human neurons and microglia individually but also in a co-culture system. In the first part of this study, we explored the protective potential of AFSC-EVs against AD progression in an *in vitro* model of affected FAD primary neurons. Interestingly, the presence of EVs restored the neuronal viability affected in AD neurons, and in parallel decreased the ROS content increased during AD. These positive effects are accompanied by a reduction in intracellular APP and Aβ oligos as well as extracellular β-amyloid accumulation. Accordingly, evidence indicates that ROS play a central role in AD transforming Aβ into toxic products, which progressively aggregate into senile plaques and finally lead to cell death [307]. In parallel to the reduction of cell death after AFSC-EVs exposure, a decrease in the apoptotic markers levels was observed. To confirm the neuroprotective effect of these vesicles, we analyzed the morphological phenotype, observing a significant improvement in neurite structure and nuclear envelope regularity, index of a reduction in AD-associated neurotoxicity. Indeed, in different age-related pathologies [308], including AD [309], nuclear envelope and lamina structure alterations were observed and linked to AD characteristic nuclear abnormalities. Since oxidative stress was recently related to Tau phosphorylation promotion and to autophagy efficiency loss [267], we also investigated these relevant AD features. Furthermore, growing evidence highlighted the connection between Tau hyperphosphorylation, APP/Aβ pathology and autophagy dysfunctions, represented by an increase of lysosomal protease [310]. In our AD model, FAD samples showed higher levels of LC3β, a fundamental protein necessary for autophagosome vacuoles formation, demonstration of a primary cellular tentative to eliminate toxic protein accumulation, which results insufficient to counteract the disease progression. More interestingly, AFSC-EV treatment induced a further increase in this autophagic marker (LC3β) accompanied by SIRT1 rise. As already discussed, Sirtuins are important mediators of antioxidant and antiapoptotic pathway as well as lysosomal autophagy regulation, fundamental for AD progression/treatment [311], so these data confirm the positive effect of AFSC-EVs on Sirtuin regulation. In addition, another hypothesis recently proposed suggests the ROS role in regulating autophagy through PI3K/Akt and AMPK. Both these pathways seem to be central in Tau protein hyperphosphorylation during AD, while PI3K/Akt is mainly implicated in the neuroprotection and inhibition of apoptosis favoring SOD proteins expression [312]. In line with this, in our system EVs promoted Akt pathway increasing its phosphorylation.

Moreover, AFSC-EV exposure reduced Tau phosphorylation in the AD characteristic site, the serine 422 [302], suggesting the EV potential in counteracting AD pathogenesis *via* the redox regulation. This is in line with the hypothesis that suggest a primitive role of redox unbalance in the development of sporadic AD before the onset of amyloid and Tau pathology [313]. These interesting results are consistent with the mechanism proposed by de Godoy et al. [192], to explain, at least in part, the neuroprotective activity of extracellular vesicles derived from MSC. The authors hypothesized that the EV-beneficial effects could be mediated by their cargo in antioxidant enzymes, anti-inflammatory and/or trophic molecules, such as endogenous catalase responsible for ROS scavenging activity. Comparably, in Chapter I we previously showed the presence of SOD1 into AFSC-EV, and we can suppose that the presence of this antioxidant protein might be one of the neuroprotective mechanisms of EVs, reducing the oxidative stress accumulation. Since a decrease in reduced glutathione (GSH) can cause an increase in ROS accumulation that leads to oxidative stress promoting AD pathogenesis [314], GSH and antioxidant protein levels were investigated. Interestingly, EV treatment significantly increased not only the GSH but also the glutathione peroxidase (Gpx) enzyme levels in FAD primary neurons. Even in not significant, FAD neurons showed slightly reduced expression of GSH, compared to WT, in accordance with the data obtained by Resende and colleagues in a similar AD mouse model, 3xTg-AD mice, where they observed decreased levels of GSH [315]. We suppose that this slight difference in GSH content after 7 days in culture could be due to intracellular antioxidant defenses carried out against the redox unbalance, as demonstrated by the increase in the antioxidant enzyme TrxR1. Importantly, both TrxR1 and TrxR2, together with SOD1 and Gpx1 increased in FAD neurons after EV treatment, contributing to ROS levels reduction. This complex redox balance is also influenced by the presence of pro-oxidant enzymes, the NADPH oxidases. In this system, the isoform constitutively active Nox4 appeared significantly increased in FAD neurons, but at least in part restored by EV treatment. On the other hand, no difference was observed for the specific Nox2-subunit gp91phox, probably because this isoform derived from a regulating subunit interaction [298].

This first part of data demonstrated that stem cell-EVs can have a direct effect on AD neurons, principally modulating the ROS content. In the meantime, growing evidence in literature suggested also an indirect therapeutic potential of stem cells, *via* the regulation of neuroinflammation reducing the microglial activation [316–318]. Moreover, studies about the efficacy of human umbilical cord blood-derived mesenchymal stem cells (hUCB-MSCs) in counteracting the disease progression in *in vivo* transgenic AD mouse model, demonstrated that these cells can increase, through a paracrine way, the microglial expression of Aβ-degrading enzymes neprilysin leading to an increase of Aβ degradation by microglial cells [319,320]. Notably, in Chapter I of this work it has been also shown the presence into AFSC-EVs of anti-inflammatory molecules, namely HGF, TGFβ, and IDO. Considering that, in the second part of this chapter the potential AFSC-EV mitigating effect on microglia activation during AD was explored. To focus our attention on the indirect effect of these vesicles *via* microglial cells, a simpler model has been set up: SH-SY5Y neuroblastoma cells treated with Aβ have been cultured with the conditioned medium derived from BV2 microglial cells exposed to AFSC-EVs that had been activated by lipopolysaccharide (LPS) as a neuroinflammation model. First, we observed an increase in SH-SY5Y neuronal death after activated BV2-CM exposure, but, interestingly, AFSC-EV pre-treatment of BV2 reduced the BV2 mediated apoptosis. This positive effect could be linked to the inhibition of microglial neuroinflammation by extracellular vesicles, thanks to their capability to reduce the ROS/NOS production by BV2 cells after LPS stimulation. Moreover, AFSC-EV positive effect against Aβ-induced indirect neurotoxicity could be acted by the inhibition of NO production and parallel promotion of TGFβ and arginase1 in BV2 cells, without excluding the protective action on neuronal cells against toxic inflammatory mediators. Indeed, the presence of TGFβ into AFSC-EVs could stimulate a positive loop since the fundamental role of TGFβ1 and TGFβ signaling in the control of microglial maturation, adult microglial homeostasis and microglia activation in CNS pathologies [321]. To explore in deep the effects of microglial cells treated with AFSC-EVs on neuronal features after Aβ exposure, a transwell co-culture system was established. Curiously, the cell viability of SH-SY5Y increased when co-cultured with inactivated BV2 cells, while the LPS-mediated activation of microglial cells induced a cell death, which further increased with the Aβ co-treatment. In parallel, the oxidative stress appeared increased in presence of both these treatments, as expected. On the other hand, the presence of AFSC-EVs prevented the redox unbalance and the neuronal death induced by the co-presence of microglial activation and Aβ. We supposed that this positive effect could be due to a double effect on microglial cells: the M1 phenotype inhibition in favor of the M2 one and the stimulation of Aβ clearance, as shown by the ELISA assay.

Concluding, the positive effect of AFSC-extracellular vesicles on both fronts, neurons and microglia, could be the winning key to treat AD-related neurodegeneration.

7. Conclusion

In conclusion, all the results obtained during my PhD provide the basis for the therapeutic application of AFSC-derived EVs in age-related conditions that affect several body districts. In particular, we demonstrated their pro-differentiative, regenerative, antioxidant and anti-inflammatory effects *in vitro* models of osteoporosis[322], atrophy-related peripheral neuropathy (under review) and Alzheimer's disease[142,295].

Since the central role played by oxidative stress in the onset and progression of these pathologies, particular attention was focus on the age-related redox unbalance between ROS production and antioxidant defenses. Interestingly, for all these models we observed a reduction in ROS accumulation after AFSC-EV exposure accompanied by an increase in antioxidant proteins, significantly reduced during aging. From the collected results, we can speculate on a possible promotion of Sirtuin/FOXO antioxidant defenses pathway acted by AFSC-EVs. Indeed, in all our experimental models the administration of AFSC-EVs induced an up-regulation of the Sirtuin/FOXO3 axis with a parallel increase in ROS scavenger proteins, namely SOD1, TrxRs, HOx1, and Gpx1, that finally lead to oxidative stress reduction.

The antioxidant effect of these vesicles could be a promising therapeutic strategy for counteracting the oxidative damage which occur during aging.

8. References

1. Loukogeorgakis, S. P. & de Coppi, P. Stem cells from amniotic fluid--Potential for regenerative medicine. *Best Pract Res Clin Obstet Gynaecol* **31**, 45–57 (2016).

2. Kolios, G. & Moodley, Y. Introduction to stem cells and regenerative medicine. *Respiration* **85**, 3–10 (2013).

3. Smith, A. A glossary for stem-cell biology. *Nature 2006 441:7097* **441**, 1060–1060 (2006).

4. Hernández, R. *et al.* Differentiation of Human Mesenchymal Stem Cells towards Neuronal Lineage: Clinical Trials in Nervous System Disorders. *Biomol Ther (Seoul)* **28**, 34–44 (2020).

5. Evans, M. J. & Kaufman, M. H. Establishment in culture of pluripotential cells from mouse embryos. *Nature* **292**, 154–156 (1981).

6. Sierra, R. A. *et al.* TCF7L1 suppresses primitive streak gene expression to support human embryonic stem cell pluripotency. *Development (Cambridge)* **145**, (2018).

7. Baharvand, H. *et al.* Generation of new human embryonic stem cell lines with diploid and triploid karyotypes. *Dev Growth Differ* **48**, 117–128 (2006).

8. Macrin, D., Joseph, J. P., Pillai, A. A. & Devi, A. Eminent Sources of Adult Mesenchymal Stem Cells and Their Therapeutic Imminence. *Stem Cell Reviews and Reports 2017 13:6* **13**, 741–756 (2017).

9. Liang, J. *et al.* Nanog and Oct4 associate with unique transcriptional repression complexes in embryonic stem cells. *Nature Cell Biology 2008 10:6* **10**, 731–739 (2008).

10. Wang, Z., Oron, E., Nelson, B., Razis, S. & Ivanova, N. Distinct lineage specification roles for NANOG, OCT4, and SOX2 in human embryonic stem cells. *Cell Stem Cell* **10**, 440–454 (2012).

11. Hambiliki, F., Ström, S., Zhang, P. & Stavreus-Evers, A. Co-localization of NANOG and OCT4 in human pre-implantation embryos and in human embryonic stem cells. *J Assist Reprod Genet* **29**, 1021 (2012).

12. Rami, F. *et al.* Recent Advances in Therapeutic Applications of Induced Pluripotent Stem Cells. *https://home.liebertpub.com/cell* **19**, 65–74 (2017).

13. Takahashi, K. *et al.* Induction of Pluripotent Stem Cells from Adult Human Fibroblasts by Defined Factors. *Cell* **131**, 861–872 (2007).

14. Ilic, D. & Polak, J. M. Stem cells in regenerative medicine: introduction. *Br Med Bull* **98**, 117–126 (2011).

15. Cananzi, M. & de Coppi, P. CD117+ amniotic fluid stem cells. *http://dx.doi.org/10.4161/org.22426* **8**, 77–88 (2012).

16. Balbi, C. & Bollini, S. Fetal and perinatal stem cells in cardiac regeneration: Moving forward to the paracrine era. *Placenta* **59**, 96–106 (2017).

17. McCormick, J. B. & Huso, H. A. Stem cells and ethics: Current issues. *J Cardiovasc Transl Res* **3**, 122–127 (2010).

18. Yeung, T. M., Chia, L. A., Kosinski, C. M. & Kuo, C. J. Regulation of self-renewal and differentiation by the intestinal stem cell niche. *Cellular and Molecular Life Sciences* **68**, 2513–2523 (2011).

19. Kiefer, J. C. Primer and interviews: The dynamic stem cell niche. *Developmental Dynamics* **240**, 737–743 (2011).

20. Kulkarni, V., Khadilkar, R. J., Srivathsa, M. S. & Inamdar, M. S. Asrij Maintains the Stem Cell Niche and Controls Differentiation during Drosophila Lymph Gland Hematopoiesis. *PLoS One* **6**, e27667 (2011).

21. He, X. C. *et al.* BMP signaling inhibits intestinal stem cell self-renewal through suppression of Wnt–β-catenin signaling. *Nature Genetics 2004 36:10* **36**, 1117–1121 (2004).

22. Wagers, A. J. The stem cell niche in regenerative medicine. *Cell Stem Cell* **10**, 362–369 (2012).

23. Simerman, A. A., Perone, M. J., Gimeno, M. L., Dumesic, D. A. & Chazenbalk, G. D. A mystery unraveled: nontumorigenic pluripotent stem cells in human adult tissues. *Expert Opin Biol Ther* **14**, 917–929 (2014).

24. Samsonraj, R. M. *et al.* Concise Review: Multifaceted Characterization of Human Mesenchymal Stem Cells for Use in Regenerative Medicine. *Stem Cells Transl Med* **6**, 2173–2185 (2017).

25. Billing, A. M. *et al.* Comprehensive transcriptomic and proteomic characterization of human mesenchymal stem cells reveals source specific cellular markers. *Sci Rep* **6**, (2016).

26. Chen, J. Y., Mou, X. Z., Du, X. C. & Xiang, C. Comparative analysis of biological characteristics of adult mesenchymal stem cells with different tissue origins. *Asian Pac J Trop Med* **8**, 739–746 (2015).

27. Davies, J. E., Walker, J. T. & Keating, A. Concise Review: Wharton’s Jelly: The Rich, but Enigmatic, Source of Mesenchymal Stromal Cells. *Stem Cells Transl Med* **6**, 1620–1630 (2017).

28. Kwon, A. *et al.* Tissue-specific Differentiation Potency of Mesenchymal Stromal Cells from Perinatal Tissues. *Sci Rep* **6**, (2016).

29. Elahi, K. C. *et al.* Human Mesenchymal Stromal Cells from Different Sources Diverge in Their Expression of Cell Surface Proteins and Display Distinct Differentiation Patterns. *Stem Cells Int* **2016**, (2016).

30. Dominici, M. *et al.* Minimal criteria for defining multipotent mesenchymal stromal cells. The International Society for Cellular Therapy position statement. *Cytotherapy* **8**, 315–317 (2006).

31. Wang, S., Qu, X. & Zhao, R. C. Clinical applications of mesenchymal stem cells. *J Hematol Oncol* **5**, (2012).

32. Soares, M. B. P. *et al.* Current Status of Mesenchymal Stem/Stromal Cells for Treatment of Neurological Diseases. *Front Mol Neurosci* **15**, (2022).

33. Chien, K. R. Regenerative medicine and human models of human disease. *Nature 2008 453:7193* **453**, 302–305 (2008).

34. Streubel, B., Martucci-Ivessa, G., Fleck, T. & Bittner, R. E. [In vitro transformation of amniotic cells to muscle cells--background and outlook]. *Wien Med Wochenschr* **146**, 216–217 (1996).

35. in ’t Anker, P. S. *et al.* Amniotic fluid as a novel source of mesenchymal stem cells for therapeutic transplantation. *Blood* **102**, 1548–1549 (2003).

36. Brivanlou, A. H. *et al.* Setting standards for human embryonic stem cells. *Science (1979)* **300**, (2003).

37. de Coppi, P. *et al.* Isolation of amniotic stem cell lines with potential for therapy. *Nat Biotechnol* **25**, 100–106 (2007).

38. de Coppi, P. *et al.* Amniotic Fluid and Bone Marrow Derived Mesenchymal Stem Cells Can be Converted to Smooth Muscle Cells in the Cryo-Injured Rat Bladder and Prevent Compensatory Hypertrophy of Surviving Smooth Muscle Cells. *J Urol* **177**, 369–376 (2007).

39. Villa, F. *et al.* The human fetal and adult stem cell secretome can exert cardioprotective paracrine effects against cardiotoxicity and oxidative stress from cancer treatment. *Cancers (Basel)* **13**, (2021).

40. Xia, J., Minamino, S., Kuwabara, K. & Arai, S. Stem cell secretome as a new booster for regenerative medicine. *Biosci Trends* **13**, 299–307 (2019).

41. Beretti, F. *et al.* Amniotic fluid stem cell exosomes: Therapeutic perspective. *Biofactors* **44**, 158–167 (2018).

42. Zavatti, M., Beretti, F., Casciaro, F., Bertucci, E. & Maraldi, T. Comparison of the therapeutic effect of amniotic fluid stem cells and their exosomes on monoiodoacetate-induced animal model of osteoarthritis. *Biofactors* **46**, 106–117 (2020).

43. Leyane, T. S., Jere, S. W. & Houreld, N. N. Oxidative Stress in Ageing and Chronic Degenerative Pathologies: Molecular Mechanisms Involved in Counteracting Oxidative Stress and Chronic Inflammation. *Int J Mol Sci* **23**, (2022).

44. Hajam, Y. A. *et al.* Oxidative Stress in Human Pathology and Aging: Molecular Mechanisms and Perspectives. *Cells* **11**, (2022).

45. Bao, Q. *et al.* Aging and age-related diseases – From endocrine therapy to target therapy. *Mol Cell Endocrinol* **394**, 115–118 (2014).

46. Jia, Q. Q. *et al.* Sesquiterpene Lactones and Their Derivatives Inhibit High Glucose-Induced NF-κB Activation and MCP-1 and TGF-β1 Expression in Rat Mesangial Cells. *Molecules 2013, Vol. 18, Pages 13061-13077* **18**, 13061–13077 (2013).

47. Martin, J. E. & Sheaff, M. T. The pathology of ageing: concepts and mechanisms. *J Pathol* **211**, 111–113 (2007).

48. Liang, R. & Ghaffari, S. Stem cells, redox signaling, and stem cell aging. *Antioxid Redox Signal* **20**, 1902–1916 (2014).

49. Bonomini, F., Rodella, L. F. & Rezzani, R. Metabolic Syndrome, Aging and Involvement of Oxidative Stress. *Aging Dis* **6**, 109–120 (2015).

50. Beckman, K. B. & Ames, B. N. The free radical theory of aging matures. *Physiol Rev* **78**, 547–581 (1998).

51. Liguori, I. *et al.* Oxidative stress, aging, and diseases. *Clin Interv Aging* **13**, 757–772 (2018).

52. Starkov, A. A. The Role of Mitochondria in Reactive Oxygen Species Metabolism and Signaling. *Ann N Y Acad Sci* **1147**, 37–52 (2008).

53. Sharifi-Rad, M. *et al.* Lifestyle, Oxidative Stress, and Antioxidants: Back and Forth in the Pathophysiology of Chronic Diseases. *Front Physiol* **11**, 694 (2020).

54. García-Sánchez, A., Miranda-Díaz, A. G. & Cardona-Muñoz, E. G. The Role of Oxidative Stress in Physiopathology and Pharmacological Treatment with Pro- And Antioxidant Properties in Chronic Diseases. *Oxid Med Cell Longev* **2020**, (2020).

55. Rohan Fernando, M. *et al.* Mitochondrial thioltransferase (glutaredoxin 2) has GSH-dependent and thioredoxin reductase-dependent peroxidase activities in vitro and in lens epithelial cells . *The FASEB Journal* **20**, 2645–2647 (2006).

56. Hanukoglu, I. Antioxidant Protective Mechanisms against Reactive Oxygen Species (ROS) Generated by Mitochondrial P450 Systems in Steroidogenic Cells. *http://dx.doi.org/10.1080/03602530600570040* **38**, 171–196 (2008).

57. Kaludercic, N., Mialet-Perez, J., Paolocci, N., Parini, A. & di Lisa, F. Monoamine oxidases as sources of oxidants in the heart. *J Mol Cell Cardiol* **73**, 34–42 (2014).

58. Liu, Y., Weng, W., Gao, R., Liu, Y. & Monacelli, F. New Insights for Cellular and Molecular Mechanisms of Aging and Aging-Related Diseases: Herbal Medicine as Potential Therapeutic Approach. *Oxid Med Cell Longev* **2019**, (2019).

59. Chandrasekaran, A., Idelchik, M. del P. S. & Melendez, J. A. Redox control of senescence and age-related disease. *Redox Biol* **11**, 91–102 (2017).

60. Almeida, M. & Porter, R. M. Sirtuins and FoxOs in osteoporosis and osteoarthritis. *Bone* **121**, 284–292 (2019).

61. Ferrara, N. *et al.* Exercise training promotes SIRT1 activity in aged rats. *Rejuvenation Res* **11**, 139–150 (2008).

62. Momken, I. *et al.* Resveratrol prevents the wasting disorders of mechanical unloading by acting as a physical exercise mimetic in the rat. *The FASEB Journal* **25**, 3646–3660 (2011).

63. Shakibaei, M. *et al.* Resveratrol Mediated Modulation of Sirt-1/Runx2 Promotes Osteogenic Differentiation of Mesenchymal Stem Cells: Potential Role of Runx2 Deacetylation. *PLoS One* **7**, (2012).

64. Salminen, A., Kaarniranta, K. & Kauppinen, A. Crosstalk between Oxidative Stress and SIRT1: Impact on the Aging Process. *Int J Mol Sci* **14**, 3834 (2013).

65. López-Otín, C., Blasco, M. A., Partridge, L., Serrano, M. & Kroemer, G. The Hallmarks of Aging. *Cell* **153**, 1194–1217 (2013).

66. Mathers, C. D., Stevens, G. A., Boerma, T., White, R. A. & Tobias, M. I. Causes of international increases in older age life expectancy. *Lancet* **385**, 540–548 (2015).

67. Zhu, Y., Ge, J., Huang, C., Liu, H. & Jiang, H. Application of mesenchymal stem cell therapy for aging frailty: from mechanisms to therapeutics. *Theranostics* **11**, 5675–5685 (2021).

68. Duncan, T. & Valenzuela, M. Alzheimer’s disease, dementia, and stem cell therapy. *Stem Cell Res Ther* **8**, 1–9 (2017).

69. lo Furno, D., Mannino, G. & Giuffrida, R. Functional role of mesenchymal stem cells in the treatment of chronic neurodegenerative diseases. *J Cell Physiol* **233**, 3982–3999 (2018).

70. Liu, L. *et al.* From blood to the brain: can systemically transplanted mesenchymal stem cells cross the blood-brain barrier? *Stem Cells Int* **2013**, (2013).

71. Matsushita, T. *et al.* Mesenchymal stem cells transmigrate across brain microvascular endothelial cell monolayers through transiently formed inter-endothelial gaps. *Neurosci Lett* **502**, 41–45 (2011).

72. Ren, C. *et al.* A neuroproteomic and systems biology analysis of rat brain post intracerebral hemorrhagic stroke. *Brain Res Bull* **102**, 46–56 (2014).

73. Lee, R. H. *et al.* Intravenous hMSCs improve myocardial infarction in mice because cells embolized in lung are activated to secrete the anti-inflammatory protein TSG-6. *Cell Stem Cell* **5**, 54–63 (2009).

74. Ward, M. R., Abadeh, A. & Connelly, K. A. Concise Review: Rational Use of Mesenchymal Stem Cells in the Treatment of Ischemic Heart Disease. *Stem Cells Transl Med* **7**, 543–550 (2018).

75. Zhang, J., Wu, Y., Chen, A. & Zhao, Q. Mesenchymal stem cells promote cardiac muscle repair via enhanced neovascularization. *Cell Physiol Biochem* **35**, 1219–1229 (2015).

76. Diamanti-Kandarakis, E. *et al.* MECHANISMS IN ENDOCRINOLOGY: Aging and anti-aging: a Combo-Endocrinology overview. *Eur J Endocrinol* **176**, R283–R308 (2017).

77. Odeh, H. M., Kleinguetl, C., Ge, R., Zirkin, B. R. & Chen, H. Regulation of the proliferation and differentiation of Leydig stem cells in the adult testis. *Biol Reprod* **90**, (2014).

78. Zhang, Z. Y., Xing, X. Y., Ju, G. Q., Zhong, L. & Sun, J. Mesenchymal stem cells from human umbilical cord ameliorate testicular dysfunction in a male rat hypogonadism model. *Asian J Androl* **19**, (2017).

79. Golpanian, S. *et al.* Allogeneic Human Mesenchymal Stem Cell Infusions for Aging Frailty. *J Gerontol A Biol Sci Med Sci* **72**, 1505–1512 (2017).

80. Musiał-Wysocka, A., Kot, M. & Majka, M. The Pros and Cons of Mesenchymal Stem Cell-Based Therapies. *Cell Transplant* **28**, 801–812 (2019).

81. Hu, C., Zhao, L., Wu, D. & Li, L. Modulating autophagy in mesenchymal stem cells effectively protects against hypoxia- or ischemia-induced injury. *Stem Cell Res Ther* **10**, (2019).

82. Doron, G., Klontzas, M. E., Mantalaris, A., Guldberg, R. E. & Temenoff, J. S. Multiomics characterization of mesenchymal stromal cells cultured in monolayer and as aggregates. *Biotechnol Bioeng* **117**, 1761–1778 (2020).

83. Maraldi, T., Beretti, F., Guida, M., Zavatti, M. & Pol, A. de. Role of Hepatocyte Growth Factor in the Immunomodulation Potential of Amniotic Fluid Stem Cells. *Stem Cells Transl Med* **4**, 539 (2015).

84. Doyle, L. M. & Wang, M. Z. Overview of Extracellular Vesicles, Their Origin, Composition, Purpose, and Methods for Exosome Isolation and Analysis. *Cells* **8**, (2019).

85. Raposo, G. & Stoorvogel, W. Extracellular vesicles: Exosomes, microvesicles, and friends. *Journal of Cell Biology* **200**, 373–383 (2013).

86. Borges, F. T., Reis, L. A. & Schor, N. Extracellular vesicles: structure, function, and potential clinical uses in renal diseases. *Brazilian Journal of Medical and Biological Research* **46**, 824–830 (2013).

87. Yáñez-Mó, M. *et al.* Biological properties of extracellular vesicles and their physiological functions. *https://doi.org/10.3402/jev.v4.27066* **4**, 1–60 (2015).

88. Zaborowski, M. P., Balaj, L., Breakefield, X. O. & Lai, C. P. Extracellular Vesicles: Composition, Biological Relevance, and Methods of Study. *Bioscience* **65**, 783–797 (2015).

89. Booth, A. M. *et al.* Exosomes and HIV Gag bud from endosome-like domains of the T cell plasma membrane. *J Cell Biol* **172**, 923–935 (2006).

90. Bebelman, M. P., Smit, M. J., Pegtel, D. M. & Baglio, S. R. Biogenesis and function of extracellular vesicles in cancer. *Pharmacol Ther* **188**, 1–11 (2018).

91. Mathivanan, S. & Simpson, R. J. ExoCarta: A compendium of exosomal proteins and RNA. *Proteomics* **9**, 4997–5000 (2009).

92. Théry, C., Ostrowski, M. & Segura, E. Membrane vesicles as conveyors of immune responses. *Nature Reviews Immunology 2009 9:8* **9**, 581–593 (2009).

93. Simons, M. & Raposo, G. Exosomes – vesicular carriers for intercellular communication. *Curr Opin Cell Biol* **21**, 575–581 (2009).

94. Géminard, C., de Gassart, A., Blanc, L. & Vidal, M. Degradation of AP2 During Reticulocyte Maturation Enhances Binding of Hsc70 and Alix to a Common Site on TfR for Sorting into Exosomes. *Traffic* **5**, 181–193 (2004).

95. van Niel, G., Porto-Carreiro, I., Simoes, S. & Raposo, G. Exosomes: A Common Pathway for a Specialized Function. *The Journal of Biochemistry* **140**, 13–21 (2006).

96. Théry, C. *et al.* Proteomic Analysis of Dendritic Cell-Derived Exosomes: A Secreted Subcellular Compartment Distinct from Apoptotic Vesicles. *The Journal of Immunology* **166**, 7309–7318 (2001).

97. Morita, E. *et al.* Human ESCRT and ALIX proteins interact with proteins of the midbody and function in cytokinesis. *EMBO J* **26**, 4215–4227 (2007).

98. Tauro, B. J. *et al.* Comparison of ultracentrifugation, density gradient separation, and immunoaffinity capture methods for isolating human colon cancer cell line LIM1863-derived exosomes. *Methods* **56**, 293–304 (2012).

99. Witwer, K. W. *et al.* Standardization of sample collection, isolation and analysis methods in extracellular vesicle research. *https://doi.org/10.3402/jev.v2i0.20360* **2**, (2013).

100. Sinha, A., Ignatchenko, V., Ignatchenko, A., Mejia-Guerrero, S. & Kislinger, T. In-depth proteomic analyses of ovarian cancer cell line exosomes reveals differential enrichment of functional categories compared to the NCI 60 proteome. *Biochem Biophys Res Commun* **445**, 694–701 (2014).

101. Lötvall, J. *et al.* Minimal experimental requirements for definition of extracellular vesicles and their functions: a position statement from the International Society for Extracellular Vesicles. *https://doi.org/10.3402/jev.v3.26913* **3**, (2014).

102. Nolte'T Hoen, E. N. M. *et al.* Deep sequencing of RNA from immune cell-derived vesicles uncovers the selective incorporation of small non-coding RNA biotypes with potential regulatory functions. *Nucleic Acids Res* **40**, 9272–9285 (2012).

103. Skog, J. *et al.* Glioblastoma microvesicles transport RNA and proteins that promote tumour growth and provide diagnostic biomarkers. *Nature Cell Biology 2008 10:12* **10**, 1470–1476 (2008).

104. Ratajczak, J., Wysoczynski, M., Hayek, F., Janowska-Wieczorek, A. & Ratajczak, M. Z. Membrane-derived microvesicles: important and underappreciated mediators of cell-to-cell communication. *Leukemia 2006 20:9* **20**, 1487–1495 (2006).

105. Zöller, M. Tetraspanins: push and pull in suppressing and promoting metastasis. *Nature Reviews Cancer 2009 9:1* **9**, 40–55 (2008).

106. Escola, J. M. *et al.* Selective enrichment of tetraspan proteins on the internal vesicles of multivesicular endosomes and on exosomes secreted by human B-lymphocytes. *J Biol Chem* **273**, 20121–20127 (1998).

107. Morello, M. *et al.* Large oncosomes mediate intercellular transfer of functional microRNA. *http://dx.doi.org/10.4161/cc.26539* **12**, 3526–3536 (2013).

108. di Vizio, D. *et al.* Large oncosomes in human prostate cancer tissues and in the circulation of mice with metastatic disease. *Am J Pathol* **181**, 1573–1584 (2012).

109. Heijnen, H. F. G., Schiel, A. E., Fijnheer, R., Geuze, H. J. & Sixma, J. J. Activated Platelets Release Two Types of Membrane Vesicles: Microvesicles by Surface Shedding and Exosomes Derived From Exocytosis of Multivesicular Bodies and □-Granules. *Blood* **94**, 3791–3799 (1999).

110. Christianson, H. C., Svensson, K. J., van Kuppevelt, T. H., Li, J. P. & Belting, M. Cancer cell exosomes depend on cell-surface heparan sulfate proteoglycans for their internalization and functional activity. *Proc Natl Acad Sci U S A* **110**, 17380–17385 (2013).

111. Jeppesen, D. K. *et al.* Reassessment of Exosome Composition. *Cell* **177**, 428-445.e18 (2019).

112. Simpson, R. J., Lim, J. W. E., Moritz, R. L. & Mathivanan, S. Exosomes: proteomic insights and diagnostic potential. *Expert Rev Proteomics* **6**, 267–283 (2009).

113. Alvarez-Llamas, G. *et al.* Recent advances in atherosclerosis-based proteomics: new biomarkers and a future perspective. *Expert Rev Proteomics* **5**, 679–691 (2008).

114. Giusti, I., Francesco, M. & Dolo, V. Extracellular Vesicles in Glioblastoma: Role in Biological Processes and in Therapeutic Applications. *Curr Cancer Drug Targets* **17**, 221–235 (2017).

115. Zhou, H. *et al.* Exosomal Fetuin-A identified by proteomics: a novel urinary biomarker for detecting acute kidney injury. *Kidney Int* **70**, 1847–1857 (2006).

116. Alvarez-Erviti, L. *et al.* Delivery of siRNA to the mouse brain by systemic injection of targeted exosomes. *Nat Biotechnol* **29**, 341–345 (2011).

117. Lai, R. C., Yeo, R. W. Y., Tan, K. H. & Lim, S. K. Exosomes for drug delivery - a novel application for the mesenchymal stem cell. *Biotechnol Adv* **31**, 543–551 (2013).

118. Harrell, C. R., Jovicic, N., Djonov, V., Arsenijevic, N. & Volarevic, V. Mesenchymal Stem Cell-Derived Exosomes and Other Extracellular Vesicles as New Remedies in the Therapy of Inflammatory Diseases. *Cells* **8**, (2019).

119. Sandonà, M. *et al.* Mesenchymal Stromal Cells and Their Secretome: New Therapeutic Perspectives for Skeletal Muscle Regeneration. *Frontiers in Bioengineering and Biotechnology* vol. 9 Preprint at https://doi.org/10.3389/fbioe.2021.652970 (2021).

120. Smith, Z. J. *et al.* Single exosome study reveals subpopulations distributed among cell lines with variability related to membrane content. *J Extracell Vesicles* **4**, (2015).

121. Laulagnier, K. *et al.* Characterization of exosome subpopulations from RBL-2H3 cells using fluorescent lipids. *Blood Cells Mol Dis* **35**, 116–121 (2005).

122. Zhang, Z., Wang, C., Li, T., Liu, Z. & Li, L. Comparison of ultracentrifugation and density gradient separation methods for isolating Tca8113 human tongue cancer cell line-derived exosomes. *Oncol Lett* **8**, 1701–1706 (2014).

123. Schumaker, V. N. Zone centrifugation. *Adv Biol Med Phys* **11**, 245–339 (1967).

124. Li, P., Kaslan, M., Lee, S. H., Yao, J. & Gao, Z. Progress in Exosome Isolation Techniques. *Theranostics* **7**, 789–804 (2017).

125. Liu, F. *et al.* The Exosome Total Isolation Chip. *ACS Nano* **11**, 10712–10723 (2017).

126. Heinemann, M. L. *et al.* Benchtop isolation and characterization of functional exosomes by sequential filtration. *J Chromatogr A* **1371**, 125–135 (2014).

127. Gámez-Valero, A. *et al.* Size-Exclusion Chromatography-based isolation minimally alters Extracellular Vesicles' characteristics compared to precipitating agents. *Sci Rep* **6**, (2016).

128. Kang, D., Oh, S., Ahn, S. M., Lee, B. H. & Moon, M. H. Proteomic analysis of exosomes from human neural stem cells by flow field-flow fractionation and nanoflow liquid chromatography-tandem mass spectrometry. *J Proteome Res* **7**, 3475–3480 (2008).

129. Musante, L. *et al.* A simplified method to recover urinary vesicles for clinical applications, and sample banking. *Sci Rep* **4**, (2014).

130. Hosseini, S., Vázquez-Villegas, P., Rito-Palomares, M. & Martinez-Chapa, S. O. General overviews on applications of ELISA. *SpringerBriefs in Applied Sciences and Technology* 19–29 (2018) doi:10.1007/978-981-10-6766-2_2/COVER.

131. Amarnath, S. *et al.* Bone Marrow-Derived Mesenchymal Stromal Cells Harness Purinergenic Signaling to Tolerize Human Th1 Cells In Vivo. *Stem Cells* **33**, 1200–1212 (2015).

132. Samsonov, R. *et al.* Lectin-induced agglutination method of urinary exosomes isolation followed by mi-RNA analysis: Application for prostate cancer diagnostic. *Prostate* **76**, 68–79 (2016).

133. Lee, K., Shao, H., Weissleder, R. & Lee, H. Acoustic purification of extracellular microvesicles. *ACS Nano* **9**, 2321–2327 (2015).

134. Zhao, Z., Yang, Y., Zeng, Y. & He, M. A microfluidic ExoSearch chip for multiplexed exosome detection towards blood-based ovarian cancer diagnosis. *Lab Chip* **16**, 489–496 (2016).

135. Hiemstra, T. F. *et al.* Human urinary exosomes as innate immune effectors. *Journal of the American Society of Nephrology* **25**, 2017–2027 (2014).

136. Muller, L., Hong, C. S., Stolz, D. B., Watkins, S. C. & Whiteside, T. L. Isolation of biologically-active exosomes from human plasma. *J Immunol Methods* **411**, 55–65 (2014).

137. Zarovni, N. *et al.* Integrated isolation and quantitative analysis of exosome shuttled proteins and nucleic acids using immunocapture approaches. *Methods* **87**, 46–58 (2015).

138. Cvjetkovic, A., Lötvall, J. & Lässer, C. The influence of rotor type and centrifugation time on the yield and purity of extracellular vesicles. *J Extracell Vesicles* **3**, (2014).

139. Soo, C. Y. *et al.* Nanoparticle tracking analysis monitors microvesicle and exosome secretion from immune cells. *Immunology* **136**, 192–197 (2012).

140. Witwer, K. W. *et al.* Updating the MISEV minimal requirements for extracellular vesicle studies: building bridges to reproducibility. *J Extracell Vesicles* **6**, 1396823 (2017).

141. Théry, C. *et al.* Minimal information for studies of extracellular vesicles 2018 (MISEV2018): a position statement of the International Society for Extracellular Vesicles and update of the MISEV2014 guidelines. *J Extracell Vesicles* **7**, (2018).

142. Zavatti, M., Gatti, M., Beretti, F., Palumbo, C. & Maraldi, T. Exosomes Derived from Human Amniotic Fluid Mesenchymal Stem Cells Preserve Microglia and Neuron Cells from Aβ. *Int J Mol Sci* **23**, (2022).

143. Bruno, S. *et al.* Mesenchymal stem cell-derived microvesicles protect against acute tubular injury. *J Am Soc Nephrol* **20**, 1053–1067 (2009).

144. Bruno, S. *et al.* Microvesicles derived from mesenchymal stem cells enhance survival in a lethal model of acute kidney injury. *PLoS One* **7**, (2012).

145. Reis, L. A. *et al.* Bone Marrow-Derived Mesenchymal Stem Cells Repaired but Did Not Prevent Gentamicin-Induced Acute Kidney Injury through Paracrine Effects in Rats. *PLoS One* **7**, e44092 (2012).

146. Gatti, S. *et al.* Microvesicles derived from human adult mesenchymal stem cells protect against ischaemia–reperfusion-induced acute and chronic kidney injury. *Nephrology Dialysis Transplantation* **26**, 1474–1483 (2011).

147. Klibanski, A. *et al.* Osteoporosis prevention, diagnosis, and therapy. *JAMA* **285**, 785–795 (2001).

148. Raisz, L. G. Pathogenesis of osteoporosis: concepts, conflicts, and prospects. *J Clin Invest* **115**, 3318–3325 (2005).

149. Nicks, K. M. *et al.* Three-dimensional Structural Analysis of the Proximal Femur in an Age-Stratified Sample of Women. *Bone* **55**, 179 (2013).

150. Seeman, E. & Delmas, P. D. Mechanisms of Disease Bone Quality-The Material and Structural Basis of Bone Strength and Fragility. (2006).

151. Liang, M. *et al.* The therapeutic effect of secretome from human umbilical cord-derived mesenchymal stem cells in age-related osteoporosis. *Artif Cells Nanomed Biotechnol* **47**, 1357–1366 (2019).

152. Ren, L. *et al.* Adipose mesenchymal stem cell-derived exosomes ameliorate hypoxia/serum deprivation-induced osteocyte apoptosis and osteocyte-mediated osteoclastogenesis in vitro. *Biochem Biophys Res Commun* **508**, 138–144 (2019).

153. Palumbo, C. & Ferretti, M. The Osteocyte: From “Prisoner” to “Orchestrator”. *Journal of Functional Morphology and Kinesiology 2021, Vol. 6, Page 28* **6**, 28 (2021).

154. Nakashima, T. *et al.* Evidence for osteocyte regulation of bone homeostasis through RANKL expression. *Nat Med* **17**, 1231–1234 (2011).

155. Kobayashi, K. *et al.* Mitochondrial superoxide in osteocytes perturbs canalicular networks in the setting of age-related osteoporosis. *Scientific Reports 2015 5:1* **5**, 1–11 (2015).

156. Sinha, K., Das, J., Pal, P. B. & Sil, P. C. Oxidative stress: the mitochondria-dependent and mitochondria-independent pathways of apoptosis. *Arch Toxicol* **87**, 1157–1180 (2013).

157. Yang, X., Jiang, T., Wang, Y. & Guo, L. The Role and Mechanism of SIRT1 in Resveratrol-regulated Osteoblast Autophagy in Osteoporosis Rats. *Scientific Reports 2019 9:1* **9**, 1–15 (2019).

158. Labbadia, J. & Morimoto, R. I. The biology of proteostasis in aging and disease. *Annu Rev Biochem* **84**, 435–464 (2015).

159. Pierrefite-Carle, V., Santucci-Darmanin, S., Breuil, V., Camuzard, O. & Carle, G. F. Autophagy in bone: Self-eating to stay in balance. *Ageing Res Rev* **24**, 206–217 (2015).

160. Onal, M. *et al.* Suppression of autophagy in osteocytes mimics skeletal aging. *J Biol Chem* **288**, 17432–17440 (2013).

161. Pierrefite-Carle, V., Santucci-Darmanin, S., Breuil, V., Camuzard, O. & Carle, G. F. Autophagy in bone: Self-eating to stay in balance. *Ageing Res Rev* **24**, 206–217 (2015).

162. Zainabadi, K., Liu, C. J. & Guarente, L. SIRT1 is a positive regulator of the master osteoblast transcription factor, RUNX2. *PLoS One* **12**, (2017).

163. Simic, P. *et al.* SIRT1 regulates differentiation of mesenchymal stem cells by deacetylating β-catenin. *EMBO Mol Med* **5**, 430–440 (2013).

164. Iyer, S. *et al.* Deletion of FoxO1, 3, and 4 in Osteoblast Progenitors Attenuates the Loss of Cancellous Bone Mass in a Mouse Model of Type 1 Diabetes. *J Bone Miner Res* **32**, 60–69 (2017).

165. Ferron, M. *et al.* Insulin signaling in osteoblasts integrates bone remodeling and energy metabolism. *Cell* **142**, 296–308 (2010).

166. Rached, M. T. *et al.* FoxO1 is a positive regulator of bone formation by favoring protein synthesis and resistance to oxidative stress in osteoblasts. *Cell Metab* **11**, 147–160 (2010).

167. Iyer, S. *et al.* FOXOs attenuate bone formation by suppressing Wnt signaling. *J Clin Invest* **123**, 3409–3419 (2013).

168. Ambrogini, E. *et al.* FoxO-mediated defense against oxidative stress in osteoblasts is indispensable for skeletal homeostasis in mice. *Cell Metab* **11**, 136–146 (2010).

169. Li, D. Y. *et al.* Autophagy attenuates the oxidative stress-induced apoptosis of Mc3T3-E1 osteoblasts. *Eur Rev Med Pharmacol Sci* **21**, 5548–5556 (2017).

170. Deng, S. *et al.* Dexamethasone induces osteoblast apoptosis through ROS-PI3K/AKT/GSK3β signaling pathway. *Biomedicine & Pharmacotherapy* **110**, 602–608 (2019).

171. Zhang, S., Liu, Y. & Liang, Q. Low-dose dexamethasone affects osteoblast viability by inducing autophagy via intracellular ROS. *Mol Med Rep* **17**, 4307 (2018).

172. Pan, J. M., Wu, L. G., Cai, J. W., Wu, L. T. & Liang, M. Dexamethasone suppresses osteogenesis of osteoblast via the PI3K/Akt signaling pathway in vitro and in vivo. *https://doi.org/10.1080/10799893.2019.1625061* **39**, 80–86 (2019).

173. Bertacchini, J., Magarò, M. S., Potì, F. & Palumbo, C. Osteocytes Specific GSK3 Inhibition Affects In Vitro Osteogenic Differentiation. *Biomedicines 2018, Vol. 6, Page 61* **6**, 61 (2018).

174. Naumann, M. *et al.* Impaired DNA damage response signaling by FUS-NLS mutations leads to neurodegeneration and FUS aggregate formation. *Nat Commun* **9**, (2018).

175. Stitt, T. N. *et al.* The IGF-1/PI3K/Akt Pathway Prevents Expression of Muscle Atrophy-Induced Ubiquitin Ligases by Inhibiting FOXO Transcription Factors. *Mol Cell* **14**, 395–403 (2004).

176. Brown, J. P. *et al.* Bone turnover markers in the management of postmenopausal osteoporosis. *Clin Biochem* **42**, 929–942 (2009).

177. Zhang, X. *et al.* Ginsenosides Rg3 attenuates glucocorticoid-induced osteoporosis through regulating BMP-2/BMPR1A/Runx2 signaling pathway. *Chem Biol Interact* **256**, 188–197 (2016).

178. Jiang, Y., Zhang, P., Zhang, X., Lv, L. & Zhou, Y. Advances in mesenchymal stem cell transplantation for the treatment of osteoporosis. *Cell Prolif* **54**, e12956 (2021).

179. Tan, S. H. S. *et al.* Mesenchymal stem cell exosomes in bone regenerative strategies—a systematic review of preclinical studies. *Mater Today Bio* **7**, 100067 (2020).

180. Yang, Y. *et al.* Application and Molecular Mechanisms of Extracellular Vesicles Derived from Mesenchymal Stem Cells in Osteoporosis. *Current Issues in Molecular Biology 2022, Vol. 44, Pages 6346-6367* **44**, 6346–6367 (2022).

181. Sui, B. *et al.* Allogeneic Mesenchymal Stem Cell Therapy Promotes Osteoblastogenesis and Prevents Glucocorticoid-Induced Osteoporosis. *Stem Cells Transl Med* **5**, 1238–1246 (2016).

182. Aggarwal, R. *et al.* Human umbilical cord blood-derived CD34+ cells reverse osteoporosis in NOD/SCID mice by altering osteoblastic and osteoclastic activities. *PLoS One* **7**, (2012).

183. Fu, Y. S. *et al.* Xenograft of Human Umbilical Mesenchymal Stem Cells from Wharton's Jelly Differentiating into Osteocytes and Reducing Osteoclast Activity Reverses Osteoporosis in Ovariectomized Rats. *Cell Transplant* **27**, 194–208 (2018).

184. Qin, Y., Sun, R., Wu, C., Wang, L. & Zhang, C. Exosome: A Novel Approach to Stimulate Bone Regeneration through Regulation of Osteogenesis and Angiogenesis. *Int J Mol Sci* **17**, (2016).

185. Shevchenko, A., Tomas, H., Havliš, J., Olsen, J. v. & Mann, M. In-gel digestion for mass spectrometric characterization of proteins and proteomes. *Nat Protoc* **1**, 2856–2860 (2006).

186. Vousden, K. H. Outcomes of p53 activation--spoilt for choice. *J Cell Sci* **119**, 5015–5020 (2006).

187. Huang, R. *et al.* Deacetylation of Nuclear LC3 Drives Autophagy Initiation under Starvation. *Mol Cell* **57**, 456–466 (2015).

188. Chen, W. *et al.* Direct Interaction between Nrf2 and p21Cip1/WAF1 Upregulates the Nrf2-Mediated Antioxidant Response. *Mol Cell* **34**, 663–673 (2009).

189. Jensen, E. D., Gopalakrishnan, R. & Westendorf, J. J. Regulation of gene expression in osteoblasts. *BioFactors* **36**, 25–32 (2010).

190. Huang, W., Yang, S., Shao, J. & Li, Y. P. Signaling and transcriptional regulation in osteoblast commitment and differentiation. *Frontiers in Bioscience* **12**, 3068–3092 (2007).

191. Iacobini, C., Fantauzzi, C. B., Pugliese, G. & Menini, S. Role of Galectin-3 in Bone Cell Differentiation, Bone Pathophysiology and Vascular Osteogenesis. *International Journal of Molecular Sciences 2017, Vol. 18, Page 2481* **18**, 2481 (2017).

192. de Godoy, M. A. *et al.* Mesenchymal stem cells and cell-derived extracellular vesicles protect hippocampal neurons from oxidative stress and synapse damage induced by amyloid-β oligomers. *J Biol Chem* **293**, 1957–1975 (2018).

193. Wen, J. *et al.* Amyloid β-Derived Diffusible Ligands (ADDLs) Induce Abnormal Autophagy Associated with Aβ Aggregation Degree. *Journal of Molecular Neuroscience 2017 64:2* **64**, 162–174 (2017).

194. Huang, K. *et al.* Polydatin promotes Nrf2-ARE anti-oxidative pathway through activating Sirt1 to resist AGEs-induced upregulation of fibronetin and transforming growth factor-β1 in rat glomerular messangial cells. *Mol Cell Endocrinol* **399**, 178–189 (2015).

195. Hauck, L. *et al.* Critical role for FoxO3a-dependent regulation of p21CIP1/WAF1 in response to statin signaling in cardiac myocytes. *Circ Res* **100**, 50–60 (2007).

196. Brunet, A. *et al.* Stress-Dependent Regulation of FOXO Transcription Factors by the SIRT1 Deacetylase. *Science (1979)* **303**, 2011–2015 (2004).

197. Gorospe, M., Wang, X. & Holbrook, N. J. Functional Role of p21 During the Cellular Response to Stress. *Gene Expr* **7**, 377 (1999).

198. Ward, I. M., Minn, K., Jorda, K. G. & Chen, J. Accumulation of checkpoint protein 53BP1 at DNA breaks involves its binding to phosphorylated histone H2AX. *J Biol Chem* **278**, 19579–19582 (2003).

199. Flores, E. R. *et al.* p63 and p73 are required for p53-dependent apoptosis in response to DNA damage. *Nature* **416**, 560–564 (2002).

200. Napoli, M. & Flores, E. R. The family that eats together stays together: new p53 family transcriptional targets in autophagy. *Genes Dev* **27**, 971–974 (2013).

201. Cecchinelli, B. *et al.* Repression of the antiapoptotic molecule galectin-3 by homeodomain-interacting protein kinase 2-activated p53 is required for p53-induced apoptosis. *Mol Cell Biol* **26**, 4746–4757 (2006).

202. Fritsch, K. *et al.* Galectin-3 interacts with components of the nuclear ribonucleoprotein complex. *BMC Cancer* **16**, 1–10 (2016).

203. Mercer, N. *et al.* AGE-R3/galectin-3 expression in osteoblast-like cells: Regulation by AGEs. *Molecular and Cellular Biochemistry 2004 266:1* **266**, 17–24 (2004).

204. Kawamata, A. *et al.* JunD suppresses bone formation and contributes to low bone mass induced by estrogen depletion. *J Cell Biochem* **103**, 1037–1045 (2008).

205. Wu, J. *et al.* EFTUD2 gene deficiency disrupts osteoblast maturation and inhibits chondrocyte differentiation via activation of the p53 signaling pathway. *Hum Genomics* **13**, 1–14 (2019).

206. Bonaldo, P. & Sandri, M. Cellular and molecular mechanisms of muscle atrophy. *DMM Disease Models and Mechanisms* vol. 6 25–39 Preprint at https://doi.org/10.1242/dmm.010389 (2013).

207. Schiaffino, S., Dyar, K. A., Ciciliot, S., Blaauw, B. & Sandri, M. Mechanisms regulating skeletal muscle growth and atrophy. *FEBS J* **280**, 4294–4314 (2013).

208. Gomes, M. D., Lecker, S. H., Jagoe, R. T., Navon, A. & Goldberg, A. L. Atrogin-1, a muscle-specific F-box protein highly expressed during muscle atrophy. *Proc Natl Acad Sci U S A* **98**, 14440 (2001).

209. Bodine, S. C. *et al.* Identification of ubiquitin ligases required for skeletal muscle atrophy. *Science* **294**, 1704–1708 (2001).

210. Sandri, M. *et al.* Foxo Transcription Factors Induce the Atrophy-Related Ubiquitin Ligase Atrogin-1 and Cause Skeletal Muscle Atrophy. *Cell* **117**, 399–412 (2004).

211. Lee, S. J. REGULATION OF MUSCLE MASS BY MYOSTATIN. *https://doi.org/10.1146/annurev.cellbio.20.012103.135836* **20**, 61–86 (2004).

212. Huang, H. & Tindall, D. J. Dynamic FoxO transcription factors. *J Cell Sci* **120**, 2479–2487 (2007).

213. Jang, Y. C. *et al.* Superoxide-mediated oxidative stress accelerates skeletal muscle atrophy by synchronous activation of proteolytic systems. *Geroscience* **42**, 1579–1591 (2020).

214. Wiedmer, P. *et al.* Sarcopenia – Molecular mechanisms and open questions. *Ageing Research Reviews* vol. 65 Preprint at https://doi.org/10.1016/j.arr.2020.101200 (2021).

215. Ji, L. L. & Yeo, D. Mitochondrial dysregulation and muscle disuse atrophy [version 1; peer review: 2 approved]. *F1000Research* vol. 8 Preprint at https://doi.org/10.12688/f1000research.19139.1 (2019).

216. Ulla, A. *et al.* Morin attenuates dexamethasone-mediated oxidative stress and atrophy in mouse C2C12 skeletal myotubes. *Arch Biochem Biophys* **704**, (2021).

217. Liu, J. *et al.* Mitochondrial Dysfunction Launches Dexamethasone-Induced Skeletal Muscle Atrophy via AMPK/FOXO3 Signaling. *Mol Pharm* **13**, 73–84 (2016).

218. Oshima, Y., Kuroda, Y., Kunishige, M., Matsumoto, T. & Mitsui, T. Oxidative stress-associated mitochondrial dysfunction in corticosteroid-treated muscle cells. *Muscle Nerve* **30**, 49–54 (2004).

219. Shimizu, N. *et al.* Crosstalk between Glucocorticoid Receptor and Nutritional Sensor mTOR in Skeletal Muscle. *Cell Metab* **13**, 170–182 (2011).

220. Ohtsuka, A., Kojima, H., Ohtani, T. & Hayashi, K. Vitamin E Reduces Glucocorticoid-Induced Oxidative Stress in Rat Skeletal Muscle. *J Nutr Sci Vitaminol (Tokyo)* **44**, 779–786 (1998).

221. Gomes-Marcondes, M. C. C. & Tisdale, M. J. Induction of protein catabolism and the ubiquitin-proteasome pathway by mild oxidative stress. *Cancer Lett* **180**, 69–74 (2002).

222. Chen, C. *et al.* Effect of Quercetin on Dexamethasone-Induced C2C12 Skeletal Muscle Cell Injury. *Molecules 2020, Vol. 25, Page 3267* **25**, 3267 (2020).

223. Gonzalez-Freire, M., de Cabo, R., Studenski, S. A. & Ferrucci, L. The neuromuscular junction: Aging at the crossroad between nerves and muscle. *Frontiers in Aging Neuroscience* vol. 6 Preprint at https://doi.org/10.3389/fnagi.2014.00208 (2014).

224. Yedigaryan, L. & Sampaolesi, M. Therapeutic implications of mirnas for muscle-wasting conditions. *Cells* vol. 10 Preprint at https://doi.org/10.3390/cells10113035 (2021).

225. Lepore, E., Casola, I., Dobrowolny, G. & Musarò, A. Neuromuscular junction as an entity of nerve-muscle communication. *Cells* vol. 8 Preprint at https://doi.org/10.3390/cells8080906 (2019).

226. Rowan, S. L. *et al.* Denervation causes fiber atrophy and myosin heavy chain co-expression in senescent skeletal muscle. *PLoS One* **7**, (2012).

227. Valdez, G. *et al.* Attenuation of age-related changes in mouse neuromuscular synapses by caloric restriction and exercise. *Proc Natl Acad Sci U S A* **107**, 14863–14868 (2010).

228. Liu, W., Wei-Lapierre, L., Klose, A., Dirksen, R. T. & Chakkalakal, J. v. Inducible depletion of adult skeletal muscle stem cells impairs the regeneration of neuromuscular junctions. doi:10.7554/eLife.09221.001.

229. Iyer, S. R., Shah, S. B. & Lovering, R. M. The neuromuscular junction: Roles in aging and neuromuscular disease. *International Journal of Molecular Sciences* vol. 22 Preprint at https://doi.org/10.3390/ijms22158058 (2021).

230. Rocha, M. C., Pousinha, P. A., Correia, A. M., Sebastião, A. M. & Ribeiro, J. A. Early Changes of Neuromuscular Transmission in the SOD1(G93A) Mice Model of ALS Start Long before Motor Symptoms Onset. *PLoS One* **8**, (2013).

231. Jackson, M. J. & Mcardle, A. Age-related changes in skeletal muscle reactive oxygen species generation and adaptive responses to reactive oxygen species. *J Physiol* **589**, 2139–2145 (2011).

232. Zhou, C. *et al.* SIRT3 alleviates neuropathic pain by deacetylating FoxO3a in the spinal dorsal horn of diabetic model rats. *Reg Anesth Pain Med* **46**, 49–56 (2021).

233. Kim, M. J., Kim, Y. M., Kim, Z. H., Heo, S. H. & Kim, S. M. Mesenchymal Stem Cells Suppress Muscle Atrophy Induced by Hindlimb Suspension. *J Stem Cell Res Ther* **5**, 266 (2015).

234. Choi, A. *et al.* Anti-Fibrotic Effect of Human Wharton's Jelly-Derived Mesenchymal Stem Cells on Skeletal Muscle Cells, Mediated by Secretion of MMP-1. *International Journal of Molecular Sciences 2020, Vol. 21, Page 6269* **21**, 6269 (2020).

235. Moussa, M. H. *et al.* Comparative Study on Bone Marrow-Versus Adipose-Derived Stem Cells on Regeneration and Re-Innervation of Skeletal Muscle Injury in Wistar Rats. *Tissue Eng Regen Med* **17**, 887–900 (2020).

236. Zhao, C. P. *et al.* Human mesenchymal stromal cells ameliorate the phenotype of SOD1-G93A ALS mice. *Cytotherapy* **9**, 414–426 (2007).

237. Zhou, F. *et al.* miRNA-9 expression is upregulated in the spinal cord of G93A-SOD1 transgenic mice. *Int J Clin Exp Pathol* **6**, 1826 (2013).

238. Nakamura, Y. *et al.* Mesenchymal-stem-cell-derived exosomes accelerate skeletal muscle regeneration. *FEBS Lett* **589**, 1257–1265 (2015).

239. Wang, X. *et al.* MicroRNA-494 Targeting Both Proapoptotic and Antiapoptotic Proteins Protects Against Ischemia/Reperfusion-Induced Cardiac Injury. *Circulation* **122**, 1308–1318 (2010).

240. Mitchell, R. *et al.* Secretome of adipose-derived mesenchymal stem cells promotes skeletal muscle regeneration through synergistic action of extracellular vesicle cargo and soluble proteins. *Stem Cell Res Ther* **10**, 1–19 (2019).

241. Mellows, B. *et al.* Protein and Molecular Characterization of a Clinically Compliant Amniotic Fluid Stem Cell-Derived Extracellular Vesicle Fraction Capable of Accelerating Muscle Regeneration Through Enhancement of Angiogenesis. *https://home.liebertpub.com/scd* **26**, 1316–1333 (2017).

242. Zhou, W. *et al.* Cancer-Secreted miR-105 Destroys Vascular Endothelial Barriers to Promote Metastasis. *Cancer Cell* **25**, 501–515 (2014).

243. Bonafede, R. *et al.* The Anti-Apoptotic Effect of ASC-Exosomes in an In Vitro ALS Model and Their Proteomic Analysis. *Cells 2019, Vol. 8, Page 1087* **8**, 1087 (2019).

244. Dellavalle, A. *et al. Pericytes of human skeletal muscle are myogenic precursors distinct from satellite cells*. *NATURE CELL BIOLOGY* vol. 9 (2007).

245. Tonlorenzi, R., Dellavalle, A., Schnapp, E., Cossu, G. & Sampaolesi, M. Isolation and characterization of mesoangioblasts from mouse, dog, and human tissues. *Curr Protoc Stem Cell Biol* **Chapter 2**, (2007).

246. Dittlau, K. S. *et al.* Generation of Human Motor Units with Functional Neuromuscular Junctions in Microfluidic Devices. *J Vis Exp* **2021**, (2021).

247. Guo, W. *et al.* HDAC6 inhibition reverses axonal transport defects in motor neurons derived from FUS-ALS patients. *Nat Commun* **8**, (2017).

248. Stoklund Dittlau, K. *et al.* Human motor units in microfluidic devices are impaired by FUS mutations and improved by HDAC6 inhibition. *Stem Cell Reports* **16**, 2213–2227 (2021).

249. Marini, V. *et al.* Long-term culture of patient-derived cardiac organoids recapitulated Duchenne muscular dystrophy cardiomyopathy and disease progression. *Front Cell Dev Biol* **10**, (2022).

250. Nascimento, C. M. *et al.* Sarcopenia, frailty and their prevention by exercise. *Free Radical Biology and Medicine* vol. 132 42–49 Preprint at https://doi.org/10.1016/j.freeradbiomed.2018.08.035 (2019).

251. Jang, Y. C. & van Remmen, H. Age-associated alterations of the neuromuscular junction. *Experimental Gerontology* vol. 46 193–198 Preprint at https://doi.org/10.1016/j.exger.2010.08.029 (2011).

252. Wang, P., Kang, S. Y., Kim, S. J., Park, Y. K. & Jung, H. W. Monotropein Improves Dexamethasone-Induced Muscle Atrophy via the AKT/mTOR/FOXO3a Signaling Pathways. *Nutrients* **14**, (2022).

253. Agnetti, G., Herrmann, H. & Cohen, S. New roles for desmin in the maintenance of muscle homeostasis. *FEBS Journal* vol. 289 2755–2770 Preprint at https://doi.org/10.1111/febs.15864 (2022).

254. Wang, X., Hu, Z., Hu, J., Du, J. & Mitch, W. E. Insulin resistance accelerates muscle protein degradation: Activation of the ubiquitin-proteasome pathway by defects in muscle cell signaling. *Endocrinology* **147**, 4160–4168 (2006).

255. Agnetti, G. *et al.* Proteomic profiling of endothelin-1-stimulated hypertrophic cardiomyocytes reveals the increase of four different desmin species and alpha-B-crystallin. *Biochim Biophys Acta* **1784**, 1068–1076 (2008).

256. Chen, C. Y. *et al.* Suppression of detyrosinated microtubules improves cardiomyocyte function in human heart failure. *Nat Med* **24**, 1225–1233 (2018).

257. Rainer, P. P. *et al.* Desmin Phosphorylation Triggers Preamyloid Oligomers Formation and Myocyte Dysfunction in Acquired Heart Failure. *Circ Res* **122**, e75–e83 (2018).

258. Tseng, A. H. H., Wu, L. H., Shieh, S. S. & Wang, D. L. SIRT3 interactions with FOXO3 acetylation, phosphorylation and ubiquitinylation mediate endothelial cell responses to hypoxia. *Biochem J* **464**, 157–168 (2014).

259. Nijssen, J., Aguila, J., Hoogstraaten, R., Kee, N. & Hedlund, E. Axon-Seq Decodes the Motor Axon Transcriptome and Its Modulation in Response to ALS. *Stem Cell Reports* **11**, 1565–1578 (2018).

260. Pollari, E., Goldsteins, G., Bart, G., Koistinaho, J. & Giniatullin, R. The role of oxidative stress in degeneration of the neuromuscular junction in amyotrophic lateral sclerosis. *Frontiers in Cellular Neuroscience* vol. 8 Preprint at https://doi.org/10.3389/fncel.2014.00131 (2014).

261. Giniatullin, A. R. & Giniatullin, R. A. Dual Action of Hydrogen Peroxide on Synaptic Transmission at the Frog Neuromuscular Junction. *J Physiol* **552**, 283–293 (2003).

262. Dupuis, L. & Loeffler, J. P. Neuromuscular junction destruction during amyotrophic lateral sclerosis: insights from transgenic models. *Curr Opin Pharmacol* **9**, 341–346 (2009).

263. Fischer, L. R. *et al.* Amyotrophic lateral sclerosis is a distal axonopathy: evidence in mice and man. *Exp Neurol* **185**, 232–240 (2004).

264. Naumenko, N. *et al.* Gender-specific mechanism of synaptic impairment and its prevention by GCSF in a mouse model of ALS. *Front Cell Neurosci* **0**, 1–8 (2011).

265. Giniatullin, A. R. *et al.* Reactive oxygen species contribute to the presynaptic action of extracellular ATP at the frog neuromuscular junction. *J Physiol* **565**, 229–242 (2005).

266. Shakirzyanova, A. *et al.* Age-dependent action of reactive oxygen species on transmitter release in mammalian neuromuscular junctions. *Neurobiol Aging* **38**, 73–81 (2016).

267. Liu, Z., Zhou, T., Ziegler, A. C., Dimitrion, P. & Zuo, L. Oxidative Stress in Neurodegenerative Diseases: From Molecular Mechanisms to Clinical Applications. *Oxid Med Cell Longev* **2017**, (2017).

268. Lane, C. A., Hardy, J. & Schott, J. M. Alzheimer's disease. *Eur J Neurol* **25**, 59–70 (2018).

269. Querfurth, H. W. & LaFerla, F. M. Alzheimer's disease. *N Engl J Med* **362**, 329–344 (2010).

270. Ferreiro, E., Oliveira, C. R. & Pereira, C. M. F. The release of calcium from the endoplasmic reticulum induced by amyloid-beta and prion peptides activates the mitochondrial apoptotic pathway. *Neurobiol Dis* **30**, 331–342 (2008).

271. Shelat, P. B. *et al.* Amyloid beta peptide and NMDA induce ROS from NADPH oxidase and AA release from cytosolic phospholipase A2 in cortical neurons. *J Neurochem* **106**, 45–55 (2008).

272. Reybier, K. *et al.* Free Superoxide is an Intermediate in the Production of H2O2 by Copper(I)-Aβ Peptide and O2. *Angewandte Chemie* **128**, 1097–1101 (2016).

273. Cheignon, C. *et al.* Oxidative stress and the amyloid beta peptide in Alzheimer's disease. *Redox Biol* **14**, 450–464 (2018).

274. Johri, A. Disentangling Mitochondria in Alzheimer's Disease. *Int J Mol Sci* **22**, (2021).

275. Gonzalez-Garcia, M., Fusco, G. & de Simone, A. Membrane Interactions and Toxicity by Misfolded Protein Oligomers. *Front Cell Dev Biol* **9**, (2021).

276. Ionescu-Tucker, A. & Cotman, C. W. Emerging roles of oxidative stress in brain aging and Alzheimer's disease. *Neurobiol Aging* **107**, 86–95 (2021).

277. Ferrer, I. *et al.* Current advances on different kinases involved in tau phosphorylation, and implications in Alzheimer's disease and tauopathies. *Curr Alzheimer Res* **2**, 3–18 (2005).

278. Bisht, K., Sharma, K. & Tremblay, M. È. Chronic stress as a risk factor for Alzheimer's disease: Roles of microglia-mediated synaptic remodeling, inflammation, and oxidative stress. *Neurobiol Stress* **9**, 9–21 (2018).

279. Zuo, L., Zhou, T., Pannell, B. K., Ziegler, A. C. & Best, T. M. Biological and physiological role of reactive oxygen species--the good, the bad and the ugly. *Acta Physiol (Oxf)* **214**, 329–348 (2015).

280. Giuliani, D. *et al.* Melanocortins protect against progression of Alzheimer's disease in triple-transgenic mice by targeting multiple pathophysiological pathways. *Neurobiol Aging* **35**, 537–547 (2014).

281. Giuliani, D. *et al.* Hydrogen sulfide slows down progression of experimental Alzheimer's disease by targeting multiple pathophysiological mechanisms. *Neurobiol Learn Mem* **104**, 82–91 (2013).

282. Angeloni, C., Gatti, M., Prata, C., Hrelia, S. & Maraldi, T. Role of Mesenchymal Stem Cells in Counteracting Oxidative Stress-Related Neurodegeneration. *Int J Mol Sci* **21**, (2020).

283. Tay, T. L., Savage, J. C., Hui, C. W., Bisht, K. & Tremblay, M. È. Microglia across the lifespan: from origin to function in brain development, plasticity and cognition. *J Physiol* **595**, 1929–1945 (2017).

284. Heneka, M. T. *et al.* NLRP3 is activated in Alzheimer's disease and contributes to pathology in APP/PS1 mice. *Nature* **493**, 674–678 (2013).

285. Singh, A., Kukreti, R., Saso, L. & Kukreti, S. Oxidative Stress: A Key Modulator in Neurodegenerative Diseases. *Molecules* **24**, (2019).

286. Venegas, C. *et al.* Microglia-derived ASC specks cross-seed amyloid-β in Alzheimer's disease. *Nature 2017 552:7685* **552**, 355–361 (2017).

287. Hansen, D. v., Hanson, J. E. & Sheng, M. Microglia in Alzheimer's disease. *J Cell Biol* **217**, 459 (2018).

288. Tang, Y. & Le, W. Differential Roles of M1 and M2 Microglia in Neurodegenerative Diseases. *Mol Neurobiol* **53**, 1181–1194 (2016).

289. Elia, C. A., Losurdo, M., Malosio, M. L. & Coco, S. Extracellular Vesicles from Mesenchymal Stem Cells Exert Pleiotropic Effects on Amyloid-β, Inflammation, and Regeneration: A Spark of Hope for Alzheimer's Disease from Tiny Structures? *Bioessays* **41**, (2019).

290. Katsuda, T. *et al.* Human adipose tissue-derived mesenchymal stem cells secrete functional neprilysin-bound exosomes. *Sci Rep* **3**, (2013).

291. Yang, H. *et al.* Intravenous administration of human umbilical cord mesenchymal stem cells improves cognitive impairments and reduces amyloid-beta deposition in an AβPP/PS1 transgenic mouse model. *Neurochem Res* **38**, 2474–2482 (2013).

292. Yokokawa, K. *et al.* Transplantation of Mesenchymal Stem Cells Improves Amyloid-β Pathology by Modifying Microglial Function and Suppressing Oxidative Stress. *Journal of Alzheimer's Disease* **72**, 867–884 (2019).

293. Ursini, F., Maiorino, M. & Forman, H. J. Redox homeostasis: The Golden Mean of healthy living. *Redox Biol* **8**, 205–215 (2016).

294. Bodart-Santos, V. *et al.* Extracellular vesicles derived from human Wharton's jelly mesenchymal stem cells protect hippocampal neurons from oxidative stress and synapse damage induced by amyloid-β oligomers. *Stem Cell Res Ther* **10**, 1–13 (2019).

295. Gatti, M. *et al.* Oxidative Stress in Alzheimer's Disease: In Vitro Therapeutic Effect of Amniotic Fluid Stem Cells Extracellular Vesicles. *Oxid Med Cell Longev* **2020**, (2020).

296. Baldassarro, V. A., Marchesini, A., Giardino, L. & Calza, L. Vulnerability of primary neurons derived from Tg2576 Alzheimer mice to oxygen and glucose deprivation: role of intraneuronal amyloid-β accumulation and astrocytes. *Dis Model Mech* **10**, 671 (2017).

297. Sun, B. *et al.* Concentrated Hypoxia-Preconditioned Adipose Mesenchymal Stem Cell-Conditioned Medium Improves Wounds Healing in Full-Thickness Skin Defect Model. *Int Sch Res Notices* **2014**, 1–6 (2014).

298. Rastogi, R., Geng, X., Li, F. & Ding, Y. NOX activation by subunit interaction and underlying mechanisms in disease. *Front Cell Neurosci* **10**, 301 (2017).

299. Singh, S., Singh, A. K., Garg, G. & Rizvi, S. I. Fisetin as a caloric restriction mimetic protects rat brain against aging induced oxidative stress, apoptosis and neurodegeneration. *Life Sci* **193**, 171–179 (2018).

300. Imbimbo, B. P. & Watling, M. Investigational BACE inhibitors for the treatment of Alzheimer's disease. *Expert Opin Investig Drugs* **28**, 967–975 (2019).

301. Zhu, Y. *et al.* CD45 Deficiency Drives Amyloid-β Peptide Oligomers and Neuronal Loss in Alzheimer's Disease Mice. *The Journal of Neuroscience* **31**, 1355 (2011).

302. Götz, J., Chen, F., van Dorpe, J. & Nitsch, R. M. Formation of neurofibrillary tangles in P301l tau transgenic mice induced by Abeta 42 fibrils. *Science* **293**, 1491–1495 (2001).

303. Xu, Y., Wei, H. & Gao, J. Natural Terpenoids as Neuroinflammatory Inhibitors in LPS-stimulated BV-2 Microglia. *Mini Rev Med Chem* **21**, 520–534 (2021).

304. Lévy, E. *et al.* Causative Links between Protein Aggregation and Oxidative Stress: A Review. *Int J Mol Sci* **20**, (2019).

305. Bitto, A. *et al.* Stress-induced senescence in human and rodent astrocytes. *Exp Cell Res* **316**, 2961–2968 (2010).

306. Madore, C., Yin, Z., Leibowitz, J. & Butovsky, O. Microglia, Lifestyle Stress, and Neurodegeneration. *Immunity* **52**, 222–240 (2020).

307. Ribarič, S. Peptides as Potential Therapeutics for Alzheimer's Disease. *Molecules : A Journal of Synthetic Chemistry and Natural Product Chemistry* **23**, (2018).

308. Lattanzi, G., Marmiroli, S., Facchini, A. & Maraldi, N. M. Nuclear damages and oxidative stress: new perspectives for laminopathies. *Eur J Histochem* **56**, 45 (2012).

309. Frost, B. Alzheimer's disease: An acquired neurodegenerative laminopathy. *Nucleus* **7**, 275 (2016).

310. Liu, Z. *et al.* The Ambiguous Relationship of Oxidative Stress, Tau Hyperphosphorylation, and Autophagy Dysfunction in Alzheimer's Disease. *Oxid Med Cell Longev* **2015**, (2015).

311. Çelik, H., Karahan, H. & Kelicen-Uğur, P. Effect of atorvastatin on Aβ1-42 -induced alteration of SESN2, SIRT1, LC3II and TPP1 protein expressions in neuronal cell cultures. *J Pharm Pharmacol* **72**, 424–436 (2020).

312. Matsuda, S. *et al.* Implications of PI3K/AKT/PTEN Signaling on Superoxide Dismutases Expression and in the Pathogenesis of Alzheimer's Disease. *Diseases* **6**, 28 (2018).

313. Birnbaum, J. H. *et al.* Oxidative stress and altered mitochondrial protein expression in the absence of amyloid-β and tau pathology in iPSC-derived neurons from sporadic Alzheimer's disease patients. *Stem Cell Res* **27**, 121–130 (2018).

314. Cenini, G., Lloret, A. & Cascella, R. Oxidative Stress in Neurodegenerative Diseases: From a Mitochondrial Point of View. *Oxid Med Cell Longev* **2019**, (2019).

315. Resende, R. *et al.* Brain oxidative stress in a triple-transgenic mouse model of Alzheimer disease. *Free Radic Biol Med* **44**, 2051–2057 (2008).

316. Bagyinszky, E. *et al.* Role of inflammatory molecules in the Alzheimer's disease progression and diagnosis. *J Neurol Sci* **376**, 242–254 (2017).

317. Yun, H. M. *et al.* Placenta-derived mesenchymal stem cells improve memory dysfunction in an Aβ1-42-infused mouse model of Alzheimer's disease. *Cell Death Dis* **4**, (2013).

318. Yang, H. *et al.* Human umbilical cord mesenchymal stem cell-derived neuron-like cells rescue memory deficits and reduce amyloid-beta deposition in an AβPP/PS1 transgenic mouse model. *Stem Cell Res Ther* **4**, (2013).

319. Kim, D. H. *et al.* Thrombospondin-1 secreted by human umbilical cord blood-derived mesenchymal stem cells rescues neurons from synaptic dysfunction in Alzheimer's disease model. *Scientific Reports 2018 8:1* **8**, 1–13 (2018).

320. Kim, H. J. *et al.* Intracerebroventricular injection of human umbilical cord blood mesenchymal stem cells in patients with Alzheimer's disease dementia: a phase I clinical trial. *Alzheimers Res Ther* **13**, 1–11 (2021).

321. Spittau, B., Dokalis, N. & Prinz, M. The Role of TGFβ Signaling in Microglia Maturation and Activation. *Trends Immunol* **41**, 836–848 (2020).

322. Gatti, M. *et al.* Amniotic Fluid Stem Cell-Derived Extracellular Vesicles Counteract Steroid-Induced Osteoporosis In Vitro. *Int J Mol Sci* **22**, 1–18 (2020).